LASER ANNEALING AND DOPANT ACTIVATION IN III-V MATERIALS

A Dissertation

Presented to the Faculty of the Graduate School

of Cornell University

in Partial Fulfillment of the Requirements for the Degree of

Doctor of Philosophy

by

Victoria Carrie Sorg

May 2017

LASER ANNEALING AND DOPANT ACTIVATION IN III-V MATERIALS

Victoria Carrie Sorg, Ph.D.

Cornell University 2017

For the past 50 years, the electronics industry has profited from their ability to follow Moores Law, doubling the performance of the computer chip approximately every two years. Traditionally, these improvements came from reducing the size of the logic switches, or transistors, so that more could fit in a given sized computer chip. However, the electronics industry has hit a roadblock where merely shrinking components no longer improves the performance. To overcome this hurdle, manufacturers are beginning to implement non-traditional device structures and materials into computer chips.

Compound semiconductors are strong candidates for materials to replace silicon based on their improved speed and efficiency with, importantly, lower power requirements. III-V materials, like InGaAs and InAs, are promising candidates to replace silicon in areas in the transistor that require high conductivity semiconductors. Low-power device architectures can be realized with GaN and other III-N materials. Although charge-carrying electrons can move much faster in these materials, a fundamental issue is getting enough free electrons into the materials through a process called doping, hence limiting the conductivity that can be achieved. This is the problem that my work addresses– studying how fast thermal processing could improve the electrical properties of doped III-V and III-N materials.

Using sub-millisecond to millisecond laser spike annealing (LSA), we can transiently reach high annealing temperatures, and, in this way, improve con-

ductivity by achieving high active concentrations of dopants in these materials. We have broadly characterized LSA for III-V and III-N materials with a high-throughput, combinatorial processing method. With this method, we explored kinetically limited states that are inaccessible using typical heating approaches like furnace and rapid thermal annealing (RTA). We found that LSA increased the activation of high-dose implanted dopants in InGaAs to a peak concentration beyond a previously established thermodynamic limit, improving dopant activation by a highly significant 29%. In contrast to longer timescale anneals (like those from furnace anneals or RTA), no deactivation is observed during LSA processing for InGaAs samples with dopants grown in to active positions. Our latest LSA studies of implanted GaN resulted in achieving nearly 100% activation of dopants. In these millisecond time frames, LSA is effective for ion-implantation dopant activation and for retention of metastable as-grown dopant concentrations. Our work shows that this kind of metastable processing will be critical to future device applications that use III-V and III-N materials.

BIOGRAPHICAL SKETCH

Victoria grew up in Eugene, Oregon, where she was raised up by two unbelievably supportive parents and was fortunate to find her soul mate while in high school.

She decided to study Chemical Engineering at Oregon State University because she liked the idea of making the world a better place with science and was drawn to the types of problems that chemical engineers get to solve. At OSU, she met phenomenal friends and mentors that helped guide projects related to her interest in sustainable energy. As part of her undergraduate honors thesis work, she explored ways to decrease energy use during hydrogen production by using ionic liquids in electrochemical step of the hybrid sulfur cycle. Additionally, she conducted undergraduate research in biodiesel and thermoelectrics. She graduated with an honors B.S. (2011) *summa cum laude*. Before coming to Cornell, she interned at NOHMs Technologies (a start-up battery company), Frito-Lay, and Carestream Health. She moved to Ithaca and joined the Clancy group, where Professor Clancy has given her the encouragement and freedom to explore her academic interests. Next, she is moving back to Oregon to work at Intel, where she will help develop next-generation electronics.

She enjoys being outside, traveling, reading, making things, learning, running, backpacking, camping, cooking, eating, and spending time with her family and friends.

This thesis is dedicated to my family and friends. Your love and support mean the world to me.

ACKNOWLEDGEMENTS

First off, I want to thank the love of my life, Tim. You are always there for me and will forever be my best friend. You are my perfect complement in every way and I am so lucky to have you. You know me better than anyone else and there is no one I would rather spend my life with... as long as that life does not include 10 more cats.

For my parents, who have always been supportive of whatever decisions I make and what I decide to put my mind to. You have taught me the values which I hold to this day. I am so fortunate to have you and I am so happy to be moving back closer to you.

I am so lucky to have an incredible committee. Professor Paulette Clancy, you instantly made me feel like Cornell was where I belonged and welcomed me into your lab. You have been a phenomenal advisor and opened up so many opportunities for me. You listened to what my goals were and your guidance has allowed me to make the most of my time at Cornell and to prepare for whatever my future may hold. Professor Mike Thompson, thank you for opening up your lab to me. I have learned so much from you and I truly appreciate all the time you have spent teaching me and challenging me to gain a deeper understanding of my research. Professor Tobias Hanrath, for being so generous with your time and for offering a fresh perspective to my project. Thank you all.

To my labmates in the Clancy group and Thompson group, thank you. Some of my best memories from Cornell are from spending time with you and problem solving on the white board with all my incoherent drawings. I am so thankful to have all the members of Thompson group train me. First off, I have also had the opportunity to work with wonderful undergraduate and masters students on my project: Megan, Suki, Emily, and Steve. Thank you for all your

contributions to this project. I truly could not have done this without each and every one of you. You have made my time here so much more memorable. I feel so fortunate to work with and learn from such hard-working, curious, and kind teammates. David, thank you so much for everything- most importantly for being a phenomenal friend. You have been so generous with your time, between brainstorming experiment ideas, co-fabricating with me in the CNF, and making the best informative limericks. Alan and Bob, thank you both for your patience and helping me learn not only laser annealing techniques that our lab uses, but also expanding the temperature calibrations our lab uses to my samples. Bob, thank you for bringing energy and excitement to the lab, I could always count on you for a smile and an entertaining story. Alan, thank you for all your help on experiments, maintaining the laser system, and always being willing to help. To the computational III-V group, Cheng Wei, Mardochee, Jingyang, and Binit, our discussions added so much insight to my project. I owe a large thanks to the many other Clancy group members for making a welcoming environment for the sole experimentalist in the Clancy group.

Thank you to the collaborators to my project: the Xing group at Cornell, IBM, and Aaron Lind of the Jones Group at University of Florida. The staff at CCMR and CNF, especially Kit Umbach who helped me with the Raman and CNF Staff who trained me on the cleanroom equipment.

And of course, to all my friends I have made at Cornell.

I am very thankful for the financial support I have received from the National Science Foundation Graduate Research Fellowship (2013) and Intel Foundation/SRCEA Graduate Fellowship (2014).

TABLE OF CONTENTS

LIST OF TABLES

LIST OF FIGURES

CHAPTER 1

INTRODUCTION

1.1 Motivation: Laser Annealing of III-V Materials

The functionality of electronics and optoelectronics are fundamentally defined by the properties of the materials they are made from. As the demand for faster, energy efficient electronics increases, the need for incorporation of new materials is becoming more pressing. Performance improvements in current devices as well as entirely new applications can be realized by choosing materials that have properties that are well-suited for a particular use. Semiconductor materials from group III and V of the periodic table are especially well-suited for this transition, covering a large parameter space of electrical and optical properties. By moving away from the limitations that come from modifications of a single material like silicon, a whole range of new possibilities emerge for engineering semiconductor band gaps, lattice constants, and mobilities. Optimizing these materials and understanding their limits for a particular application are critically reliant on processing, which will define how a material functions.

1.2 Thesis Overview

This thesis focuses on how high-temperature, short time-scale heating and quenching with a laser affects III-V materials. A powerful, high-throughput method was developed to rapidly characterize a continuous distribution of annealing temperatures to determine how laser annealing changes properties of

interest in III-V materials, in this case crystalline quality and electrical characteristics. Additionally, metrics like annealing temperature and time were characterized on these samples so that they could be directly compared to the established results of longer timescale heating methods. This analysis allows us to probe kinetically limited annealing states that are inaccessible to longer timescale methods. We found that the high temperatures and short timescales in laser annealing leads to improved electrical behavior compared to traditional, longer timescale annealing methods.

CHAPTER 2

BACKGROUND ON COMPOUND SEMICONDUCTORS

2.1 Compound Semiconductors

2.1.1 Material Properties

Compound semiconductors, a crystalline blend of two or more elements from the periodic table like SiGe, GaN or InGaAs, represent a promising class of materials that could enable improved performance and increased efficiency in the operation of electronics. These materials overcome some of the challenges inherent in designing devices around an elemental semiconductors like Si or Ge, and can have niche applications unavailable to elemental semiconductors [25, 26]. Compound semiconductors are unique because you can tune their material and electrical properties by changing their composition, which is ideal for engineering the next generation of electronic devices. Alloys of compound semiconductors are especially powerful for their ability to form completely miscible ternary and quaternary materials. This thermodynamic property allows such alloys to explore a continuous change in a material or electrical property based on composition [2]. For example, by blending two binary compound semiconductors together into a ternary, e.g. blending InAs and GaAs to form InGaAs, you can change both the band gap of the material as well as the lattice constant. Figure 2.1 displays the γ-valley energy gap as a function of lattice constant. The binary materials are displayed as points, whereas the band gap of ternary or quaternary materials are shown along the solid curves that join the binaries that they are composed of. This powerful property makes a rich material

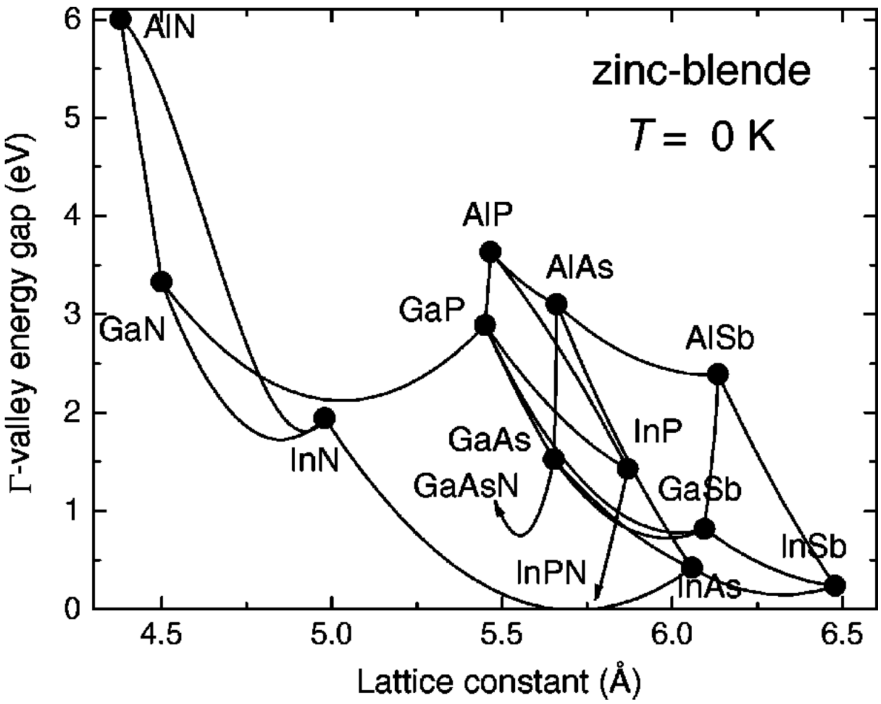

Figure 2.1: The Γ-valley energy gap as a function of lattice constant for III-V materials. Both the lattice constant and Γ-valley energy gap can be modified by changing the composition of the alloy, as represented by the solid lines connecting the III-V compounds. Reproduced with permission from Vurgaftman *et al.* [2], copyright Journal of Applied Physics 2001.

phase space, so that an ideal material can be designed based on its properties, rather than limiting device design based on the properties of a single material.

Within the class of compound semiconductor materials, compounds with direct band gaps, or optoelectronics, are particularly important for applications like photovoltaics, energy conversion, and transistors. A well-known class of optoelectronic materials is III-V compound semiconductors, which consist of atoms from group III and V of the periodic table. These materials could allow continued scaling of next generation transistors because of their fast electron transport properties and low supply voltage requirements [27, 28, 29, 3, 30].

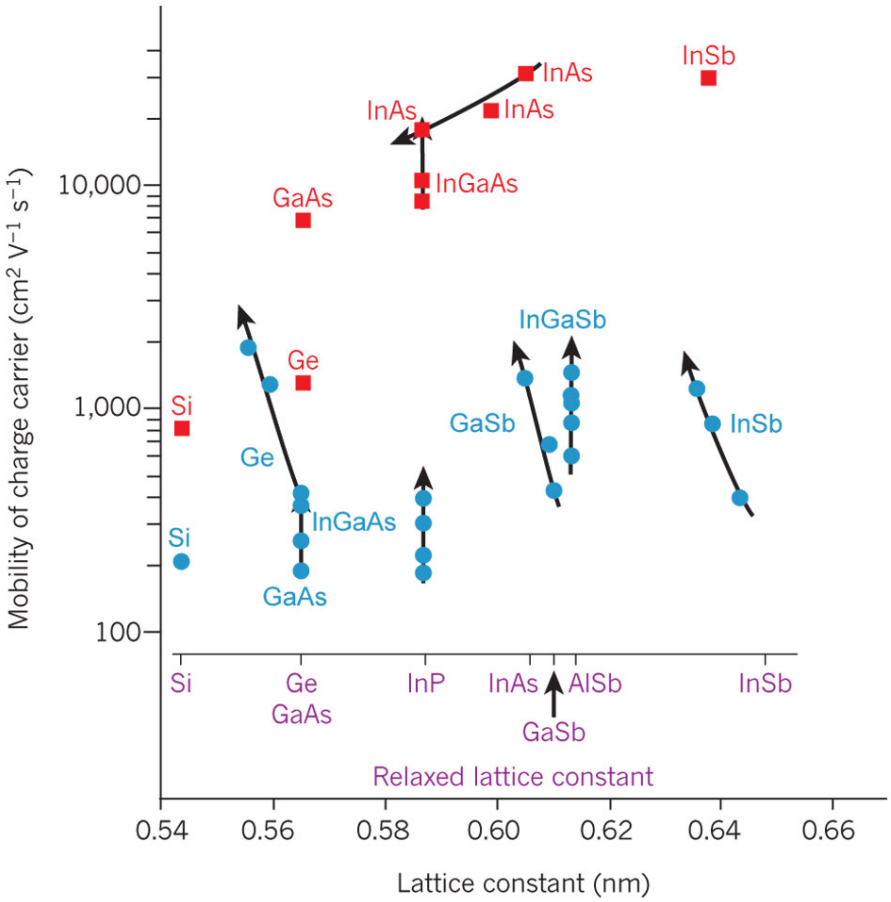

Figure 2.2: The electron mobility (red squares) and hole mobility (blue circles) versus lattice constant for some III-V materials of interest compared to elemental semiconductors like Si and Ge. III-V materials have higher electron mobilities than Si and Ge. Reproduced with permission from del Alamo [3], copyright Nature 2011.

Optoelectronics are defined by the property of having a direct band gap, which contributes the advantage of a low supply voltage. Additionally, these materials can have high charge carrier mobility. By replacing silicon with a material with higher mobility, the transistor channel can become more conductive. An excellent review that addresses electronic scaling limits using III-V electronics is provided by del Alamo [3].

Figure 2.2 displays the mobility of charge carriers versus lattice constant for some III-V materials compared to group IV materials traditionally used in electronics (Si and Ge). The electron (red squares) and hole (blue circles) mobilities represent the speed at which charge carriers can move in response to an electrical field. The higher the mobility, the faster the charge carrier can move. The direction of the arrows represents compressive biaxial strain, which can be used to modify the mobility.

2.1.2 Electronic and Optoelectronic Applications

The electrical properties of some III-V materials, namely the band gap and mobility of these materials, make them applicable for use in a wide variety of applications [3]. Direct band gap III-V materials are extremely useful in a broad range of optoelectronic devices that detect or emit light, like photovoltaics, LEDs, lasers, and photo detectors. Their outstanding electron transport characteristics are particularly well-suited to improvements in transistor performance.

In the interest of moving beyond the material limitation of silicon in transistor technology [31, 32], there is a growing interest in III-V MOSFETs [33]. As one example of this, InGaAs is considered to be a promising candidate for *n*-type channels and source/drain contacts in transistors [34, 30]. As a III-V material, it has approximately 10 times the electron mobility of silicon [3]. InGaAs is a ternary, zinc blende semiconductor made up of InAs and GaAs sublattices. This combination creates a balance in its material properties: the high electron mobility in InGaAs is a result of the high mobility electrons in InAs, while the low current leakage from thermally excited carriers comes from the

larger band gap of GaAs. This blend of material characteristics makes it ideal for use in channels. Using InGaAs for *n*-type channels, devices could have low power dissipation while still achieving high speeds. III-V materials have the additional advantage that they are amenable to typical micro and nanofabrication techniques. Unlike other emerging high-mobility materials like carbon nanotubes and nanowires [35], III-V materials allow conventional lithography and etch techniques to be used [27]. Overall, InGaAs has the potential to allow devices to continue transistor scaling according to Moore's Law.

One subset of III-V materials that is widely studied involves using nitrogen as the group V element, or III-N materials. These materials are particularly exciting because the direct band gaps of alloys of these materials span the entire visible spectrum of light (Figure 2.1). Theoretically, this makes light emission possible at any visible wavelength by changing the composition of the alloy. Practically accessing this behavior can be extremely challenging, due, in no small part, to the complication arising from defects introduced during material growth processes. This challenge is illustrated by three decades of work that went into making an efficient blue light-emitting diode before the 2014 Nobel Prize winning work of Isamu Akasaki, Hiroshi Amano, and Shuji Nakamura, who overcame these growth-related defect issues [36, 37]. Beyond light emission, gallium nitride (GaN) and other related III-N materials combine the advantages of fast carrier transport, a high breakdown voltage and low "on" resistance essential for power switching devices and high voltage applications. In power switching devices that convert AC to DC power, large inefficiencies and power loss occur in silicon-based devices. These inefficiencies are based on the material properties of silicon and can be overcome by switching to wide band gap material systems that are better suited for power conversion, like GaN. [38].

Combining these materials with a vertical device structure can allow low-cost efficient power devices to be realized [38].

2.1.3 Heterogeneous Integration and Growth Methods

Considerable effort is underway to integrate III-V films into device fabrication on silicon substrates. There are a variety of reasons why III-V materials must be integrated onto a silicon substrate. Primarily, an efficient processing infrastructure for silicon-based devices is already established. The presence of this infrastructure leads to low substrate costs and well-developed processing techniques. In addition, silicon has a number of highly desirable mechanical and chemical properties. Silicon wafers are more robust and can dissipate heat more easily than GaAs wafers, say. The availability of large silicon wafer sizes also means that the combined photonic-electronic functionality and higher speed signal processing is distributed over larger substrate areas. Since the properties of silicon substrates is well-characterized, the integration of III-V materials can bridge the transition between silicon and fundamentally different functionality offered by III-V materials.

There are a number of difficult material challenges that must be overcome before this desirable integration can happen [30]. These challenges stem from crystallographic and chemical compatibility differences between silicon and III-V materials. In general, heteroepitaxial films are more difficult to grow than bulk crystals [39]. Since the substrate and the thin film have inherently different compositions and structures, defects can form, such as dislocations, twins, and stacking faults. Electronic and optoelectronic applications requiring epitaxial

films are extremely intolerant of defects because they lead to decreases in carrier concentration and mobility in devices [39]. These differences in materials characteristics can lead to grain boundaries, stress/strain, and interfacial defects. Intel's Component Research group has identified the main challenges for integration of III-V materials with silicon as anti-phase boundary defects, thermal mismatch, and lattice mismatch [29]. Of these challenges, lattice-matching and thermal expansion were identified as being the most important [25].

Thermal mismatch is the result of the different coefficients of thermal expansion (CTE), α_{th}, between the two materials. For the materials of interest to this thesis, Table 2.1 shows the linear CTE at 300 K [40, 25, 1]. Heating and cooling materials with dissimilar CTE values can lead to significant stress and strain [25]. The thermal strain (ϵ_{th}) can be found from Equation 2.1 as a function of the thermal expansion coefficient(α_{th}) and the temperature, T. The temperature used for the deposition, as well as any subsequent processing steps, must be limited to reduce the likelihood of introducing defects resulting from the differing CTE values. This is extremely difficult because annealing is instrumental in a number of steps in traditional semiconductor processing.

$$\epsilon_{th} = \int_{Ti}^{Tf} \Delta\alpha_{th} dT \tag{2.1}$$

Dislocations and stress/strain can also be a result of differences in lattice parameters. A lattice mismatch of less than 0.1% is required in optoelectronic devices [39]. InGaAs has a lattice parameter that is 8% larger than silicon, as shown in the horizontal axis of Figure 2.2. This large difference could lead to the creation of significant defects at the interface between the two materials.

Table 2.1: The coefficient of thermal expansion for III-V binaries, silicon, and other materials of interest for this thesis. Differences in thermal expansion coefficients can cause stress in layered, heterogeneous films during heating and cooling.

Material	α_{th} $[10^{-6}\mathbf{K}^{-1}]$
Si	2.62
GaAs	6.03
$In_{0.53}Ga_{0.47}As$	5.69
InAs	5.50
InP	4.56
GaN	5.0
Al_2O_3	5.2
SiO_2	0.5

There are two methods of integrating InGaAs into the silicon substrate: monolithic and pseudomonolithic [25]. In monolithic integration, all devices in the circuit are formed on a single substrate in a manner that is compatible with simultaneously processing large batches of full wafers, each containing numerous individual circuit chips [25]. Both crystal structure and coefficient of thermal expansion are important for monolithic integration [25]. This type of integration could be achieved through a process such as epitaxy. The second type of integration is pseudomonolithic [25]. This method is based on bonding of processed or partially processed optoelectronic devices onto selected sites on the silicon wafer. In this technique, the coefficient of thermal expansion is important, while crystal structure is not. Structures having a large lattice mismatch *can* be fabricated with misfit locations but without threading dislocations [39].

Although monolithic integration may not be essential, it will be the focus of the remainder of the section.

InGaAs and silicon are structurally, chemically, and electronically different from each other which makes heteroepitaxy difficult. There are a variety of considerations when choosing a deposition technique. For electronic devices, it is essential to have highly ordered, defect-free films with near atomic resolution film/substrate abruptness, high levels of doping uniformity, and the ability to grow multilayered structures with different compositions and doping levels. Additionally, due to differences in CTE, a relatively low processing temperature must be used. There are two main options that Ohring identified that are appropriate for deposition for high performance applications [39]. The first deposition option is metalorganic chemical vapor deposition (MOCVD), alternatively known as organometallic vapor-phase epitaxy (OMVPE) or metalorganic vapor-phase epitaxy (MOVPE). The second option is molecular beam epitaxy (MBE) [39]. Both methods use low temperature growth, far from equilibrium and will be discussed in more detail in the section on growth and doping.

There has been experimental success with monolithic integration using layers that are compositionally graded. This eases the difference in lattice parameter between silicon and InGaAs. One example is the "silicon on lattice-engineered substrate" (SOLES) developed at MIT [41]. This technique allows III/V materials to be sandwiched between layers of silicon. Using MOCVD, this group used Ge-on-insulator, then compositionally graded III-V until a relaxed, large lattice on silicon was accomplished. Intel has developed another technique that made transistors comparable in performance to devices made on III-V substrates [42]. They use a silicon substrate that is cut off-axis to increase the lattice

parameter. Then they use MBE to grow buffer layers of GaAs and $In_xAl_{1-x}As$ with suitably graded composition. These buffer layers ease the change in lattice parameter and electronically insulate the InGaAs channel. They found that this procedure confined the dislocations to the buffer layers.

Other heterogeneous integration methods focus growing III-V materials directly on silicon without compositionally graded materials. One such method is aspect ratio trapping where the III-V material is grown on Si in SiO_2 trenches [30]. The III-V growth is confined to high aspect area patterned SiO_2 trenches on Si and the misfit and threading dislocations are diverted towards the sidewalls during growth [30]. Another method for integration is growing nanowires using vapor-liquid-solid growth or selective area epitaxy, with just the base of the wire contacting the silicon substrate [30]. Since the contacting surface area is minimized between the III-V and silicon substrate, it avoids forming dislocations. A final method is using MOCVD and patterned oxide masks to selectively grow III-V materials [30, 43].

In summary, monolithic integration is challenging due to differences in structure, chemistry, and electronic characteristics between silicon on III-V materials. In terms of growth and processing, lattice mismatch and thermal expansion differences cause the largest problems. In order to make defect-free devices, a relatively low temperature process is needed that makes highly ordered and uniform films. The most likely candidates according to Ohring are MBE and OMVPE. Monolithic integration has been successful in lab-scale devices through using low temperature processes that grow buffer layer films with a gradually increasing lattice parameter between the silicon and InGaAs layers. III-V materials have also been successfully grown directly on silicon by mini-

mizing the interfacial area between silicon and III-V and confining its growth, misfit dislocations can be controlled or even eliminated. Although it is a promising start, monolithic integration still faces many challenges that may impede large-scale implementation in transistors.

2.1.4 Doping

Point defects in a semiconductor can have an enormous impact on the chemical and electrical properties of a material [44]. Point defects can occupy substitutional, interstitial, or vacancy sites in the lattice. Defects can be native (intrinsic) to the semiconductor or they can be introduced when adding impurities through doping or contamination (extrinsic). The movements of atoms through diffusion mechanisms are critically reliant on the nature of the point defects, which can be charged or electrically neutral. In order to affect the electrical properties of the semiconductor, the dopants need to occupy places in the lattice where they are charged, or electrically active. In other words, the dopants need to occupy positions in the crystalline lattice where the electrons in the outer shell of the dopant delocalize. The emphasis in this thesis is on n-type materials, namely, materials that donate electrons to improve conduction. For a semiconductor, the conductivity (σ) relies on the number of conducting electrons (n) and holes (p), the elementary charge (e), and the mobility (μ), as shown in Equation 2.2. The conductivity (σ) is inversely related to the resistivity (ρ) through the equation:

$$\sigma = ne\mu_n + pe\mu_p = \frac{1}{\rho} \tag{2.2}$$

Understanding and controlling the complex doping and defect structures that will arise as a result of processing is one of the primary challenges associated with III-V, or indeed any, semiconductor material. There are many possible defect structures for both intrinsic and extrinsic defects, as well as many possible dopants [45, 4]. The defect populations and thus the properties of a material is dependent on its growth, doping, and thermal processing. Samples can be grown into metastable states that are kinetically, but not thermodynamically, stable [46]. The formation energies of charged point defects determines thermodynamic stability at 0 K. Wang *et al.* determined the formation energy of possible point defects in silicon-doped ordered $In_{0.5}Ga_{0.5}As$, as shown in Figure 2.3 [4]. Each defect is labeled with the atom and its location as a superscript. The slope of the line gives the charged state of the dopant. The lower the formation energy, the more energetically favorable is the formation of the point defect. Figure 2.3a shows that Fermi Level pinning for As-poor growth conditions is unfavorable for *n*-type doping. Figure 2.3b shows that, in Ga-poor growth conditions, it is energetically favorable for Si to sit on a Ga site, with the slope of the line showing that Si on a Ga site will act as a donor. Figure 2.3c shows that Si located on an In site as a donor is favorable for In-poor growth conditions. Comparable work has been completed for GaN systems [47, 48].

The effectiveness of electronic devices are critically reliant on the controlled doping of semiconductors. Bulk electrical properties arise as a direct result of the arrangement of atoms on the crystal lattice. Doping occurs by the addition of impurities to crystalline semiconductor materials, which modifies its electronic properties. Dopants can be added using a variety of methods. They can be incorporated during the growth of the semiconductor using techniques such as Molecular Beam Epitaxy (MBE) or Metal Organic Chemical Vapor Deposi-

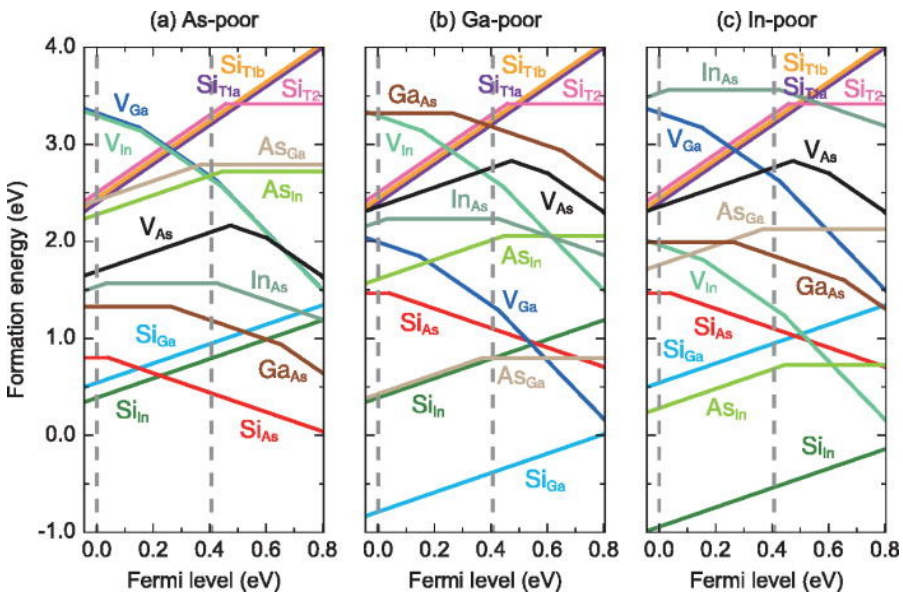

Figure 2.3: Formation energy of point defects in $In_{0.5}Ga_{0.5}As$. The defects with the lowest formation energy at a given Fermi level are the most thermodynamically favorable to form. The slope of the line indicated the charge state of the defect. Reproduced with permissions from Wang *et al.* [4], copyright Journal of Applied Physics 2017.

tion (MOCVD). They can be added through diffusion or they can be implanted into the crystal through ion-implantation. Each of these methods has distinct trade-offs in terms of expense, time, additional processing steps, introduction of defects, and spatial selectivity. The growth and processing steps that a material goes through will determine its electrical performance. Thus, it is important to review dopant incorporation techniques.

Doping during Growth

The techniques for III-V growth for monolithic integration semiconductors can also be used to incorporate dopants. These growth techniques, namely MOCVD

and MBE, both happen at relatively low temperatures compared to equilibrium growth methods. This is ideal to reduce dislocations and defects from differing CTE during growth. MOCVD uses the vapor phase chemical precursors to deliver metalorganic reactants to the substrate, where the the precursors react to form a solid and the gaseous byproducts are carried away. An example of this reaction to form GaAs is using TMGa and arsine to form GaAs and methane as a byproduct [39, 49]. MBE growth occurs in an ultra high vacuum environment, where effusion ovens evaporate source materials to provide beams of molecules or atoms delivered to the substrate [39, 49]. The substrate is heated to promote surface reactions and migration [49]. Ohring compared and contrasted the two growth methods, MOCVD and MBE for epitaxy [39]. According to Ohring, both techniques can be used to grow high quality films and layered structures with differing compositions with near-atomic interface abruptness and high doping uniformity. MOCVD has a relatively fast growth rate, 2-3 times faster than MBE. MOCVD also has the advantage of less maintenance downtime than MBE. The MBE growth process occurs at lower temperature and is farther from equilibrium. Additionally, the vacuum environment in MBE makes *in situ* measurements possible. MBE also is generally safer, the precursors used in MOCVD are often toxic and/or pyrophoric. The device characteristics of MBE-grown materials are generally superior to MOCVD-grown material, but it is not always the case [39, 50].

Doping after Growth

There are a few options for adding dopants to a material after growth. These including diffusion, transmutation, and ion-implantation [49]. Ion-implantation

will be the focus of this discussion because, in general, it is inexpensive and well-controlled [51, 52]. During ion-implantation, a sample is biased and a high energy beam of ionized dopants is accelerated towards it. Using masking, dopants can be selectively implanted into certain areas of the sample, which is especially useful for self-aligned device structures. The implant depth, the crystalline damage, the number of dopants introduced, and the defects formed depend on: the substrate, the dopant species, implant energy, implant dose, angle of implant relative to the crystal orientation, and substrate temperature. Some of the drawbacks of this technique are material damage up to amorphization, ion-channeling, and the need for additional thermal processing to activate the dopants. Because of the abundance of defects that are possible, the role of implant conditions on defects and electrical properties in III-V semiconductors has been widely studied [53, 54, 55, 56, 57]. For III-V materials, the main challenge is the fact that the high temperature needed to activate carriers and repair implant damage is beyond the temperature at which the materials thermally decompose by evaporation. Additionally, implantation can form damaged regions, including dislocation loops, which are difficult, if not impossible, to remove through annealing. Previous work has identified that crystalline damage is repaired at a lower temperature, whereas a higher temperature is needed to move dopants into electrically active positions [53, 58].

2.1.5 Annealing

In III-V materials, the low vapor pressure of the group V atom in the compound semiconductor lattice leads to an additional complication during thermal processing. The low vapor pressure is a result of the polar-covalent bonding. With

annealing, the semiconductor will start to thermally decompose before reaching the melt, as the group V atom evaporates and causes surface degradation [59].

To address this issue of evaporation of the group V atom, a few techniques have been developed [60, 61, 33, 45]. One such technique involves annealing the sample in an ambient environment of the species that evaporates, or the capless anneal. One version of this capless anneal is the so-called "proximity cap" method, which relies on the thermal decomposition of a sacrificial material to provide the ambient environment rich in the evaporating species [62, 63]. The final technique is to add a thin dielectric layer to prevent surface arsenic loss upon heating, commonly known as a capping layer. The dielectrics most often used are Al_2O_3 [64, 65], SiN_x[66, 67, 68, 65], SiO_xN_y[69], and SiO_2[68]. Another way to limit evaporation is to decrease the time that a sample is annealed for, putting kinetic limitations on the thermodynamically driven process.

For logic applications like shallow junctions, or other devices with shrinking dimensions, the location of dopants is extremely important. Thus, one of the current driving forces in semiconductor processing is to move towards limiting the amount of time over which a sample is heated, or annealed, in an attempt to limit dopant redistribution through diffusion [70]. These so-called "low thermal budget" processes heat a sample quickly, on a timescale that is not long enough for the sample to reach equilibrium. Thermal budget is commonly defined as the area under a time/temperature curve [71]. In industrial applications, these short timescales can also reduce wafer throughput time. Conventional, long timescale heating in semiconductor processing uses furnace annealing, which happens on the order of minutes to hours. This type of annealing results in the sample reaching an equilibrium state. Rapid Thermal Annealing (RTA) occurs

on timescales on the order of seconds. This work is focused on Laser Spike Annealing (LSA), which occurs in the sub-millisecond to millisecond regime. The shorter timescale anneals push the sample into states that are kinetically-limited, rather than thermodynamically limited. Additionally, these anneals often occur at higher temperatures, which can provide enough energy for formation of point defects or dopant activation with high activation energies that are inaccessible to lower temperature/lower energy anneals. Laser annealing is a short timescale annealing technique. It has distinct advantages over other annealing methods because heating can be localized in space and in time [72]. Additionally, temperatures reached during laser annealing can be extremely high, beyond which commercial annealing processing equipment can typically withstand. For example, commercial RTA equipment can reach up to 1200 °C [73]. Considering the general rule that 2/3 of the material's melting temperature is needed to repair crystalline damage, annealing temperatures may be needed beyond those accessible with traditional equipment [73].

Laser Annealing of III-V

Laser annealing of III-V materials has been explored by other groups using a range of different timescales and laser wavelengths. Most of this work has been conducted using pulsed lasers, though some work has been conducted with continuous wave lasers. Some of the laser-annealed samples reached the melt, whereas others were annealed at lower temperatures. The work that was conducted with GaAs is particularly relevant for the closely related InGaAs system studied here. A brief summary of the most relevant studies will be covered here.

Golovchenko *et al.* used a Q-switched ruby laser (λ = 694.3 nm) with a single

12 ns pulse to anneal uncapped Te-implanted GaAs [74]. They found that annealing recrystallized the amorphorization that occurred during implantation and that the Te was incorporated into the GaAs lattice sites beyond the solubility limit of Te in GaAs, with little long-scale diffusion. Electrical tests, however, showed that the measured resistivity was comparable to conventionally doped samples, indicating low mobility or large amounts of electrically inactive dopants.

Sealy, Kular, Badawi *et al.* used a Q-switched ruby laser (λ = 694.3 nm) with a single 15-25 ns pulse to study the electrical properties of laser-annealed GaAs ion-implanted with Se and Te both with and without capping layers [75, 66, 67]. They found that they could achieve carrier concentrations in the range of 1-2 10^{19} cm^{-3} and the high temperature capping process repaired some of the crystalline damage from ion-implantation. Even on the capped samples, Ga precipitates formed on the surface as As evaporated. Semi-insulating samples that were not implanted with dopants but capped with Si_3N_4 were conductive after laser annealing. The capping layer was assumed to act as a source of dopants, leading to *n*-type doping the sample after melting [67]. Other groups subsequently confirmed this behavior [76, 77].

Using a Q-switched Nd: YAG laser (λ = 1.06 µm), Barnes *et al.* annealed uncapped Te-implanted GaAs with overlapping 125 ns pulses [78]. They determined that they could incorporate Te to concentrations above the solubility limit, but found evidence of large length scale diffusion that suggested melt and recrystallization of their films. After removing the excess Ga from the surface that formed from As evaporation with a HCl etch and removing the 5 nm of the surface, the authors found that they could make ohmic contacts, but that only

1% of the Te located on lattice sites were electrically active.

Using a pulsed CO_2 laser, James *et al.* annealed Zn-doped and Si-doped GaAs to melt and observed As loss. For the doped samples, they noted that an increase in temperature led to a rapid increase in free carrier absorption, creating areas with localized heating [79].

Most recently, Kong *et al.* explored forming shallow junctions by coating an InGaAs film with silicon monolayers, capping the sample, and using a laser to anneal the sample and drive in silicon dopants [80]. They laser-annealed InGaAs films with a single 23 ns pulse of an excimer laser $\lambda = 248$ nm [80]. By combining delta doping of silicon (using either silane or disilane treatments) and laser annealing, they were able to avoid damage from implantation while incorporating silicon concentrations nearing 10^{21} Si/cm^3. By changing the laser fluence, they were able to change the melt depth, forming junctions on the order of tens of nanometers. They also found that RTA at 800 °C was insufficient to activate dopants but was high enough to lead to unwanted substrate degradation, necessitating the need for laser annealing.

2.1.6 Electrical Activation

Understanding the complexities of III-V doping and how thermal processing affects the electrical properties of III-V semiconductors has been the focus of many studies. Since this thesis focuses on *n*-type $In_{0.53}Ga_{0.47}As$ and GaN, what follows will emphasize results for these material systems. Doping methods explored to date can be split into two categories, namely, samples with dopants added during growth or after growth through processing like ion-implantation. The

grown-in samples have dopants that are already incorporated into positions where they are electrically active. The goal of these samples is to determine whether the active concentrations are thermally stable with annealing or if they deactivate or form charge-compensating defects following thermal processing. Samples that are ion-implanted require a thermal annealing step to repair the resultant crystalline damage to the lattice and to move dopants to active positions in the lattice.

InGaAs

Elements from groups IV or VI from the periodic table have successfully been used for *n*-type doping of InGaAs [45, 12, 81]. For group IV, the dopant must sit on a III site to donate an electron for conduction. If it sits on a group V site, the dopant is an acceptor. If a dopant can exhibit both *n*- and *p*-type behavior it is said to be amphoteric. Carbon tends to act as a *p*-type dopant, whereas Si, Ge, and Sn act as *n*-type dopants [81]. Si is commonly used because of its relatively high activation and low diffusivity. From group IV, S, Se, and Te are possible dopants. Orzali *et al.* compiled carrier concentrations for various as grown dopants, Figure 2.4 [10]. The $In_{0.53}Ga_{0.47}As$ samples are plotted in the center of the graph, with *n*-type carrier concentrations up to $\approx 10^{20}$ cm^{-3} using MBE or MOCVD to dope with Sn, Te, or Si.

An example taken from Fedoryshyn *et al.*, shown in Figure 2.5, shows that metastable MBE-grown $In_{0.53}Ga_{0.47}As$ samples that are either volume- or delta-doped with silicon. The carrier concentration and mobility were measured using Hall Effect measurements. These samples show an $\approx 2.9 \times 10^{19}$ cm^{-3} carrier concentration limit, presumably as a result of the amphoteric nature of the sili-

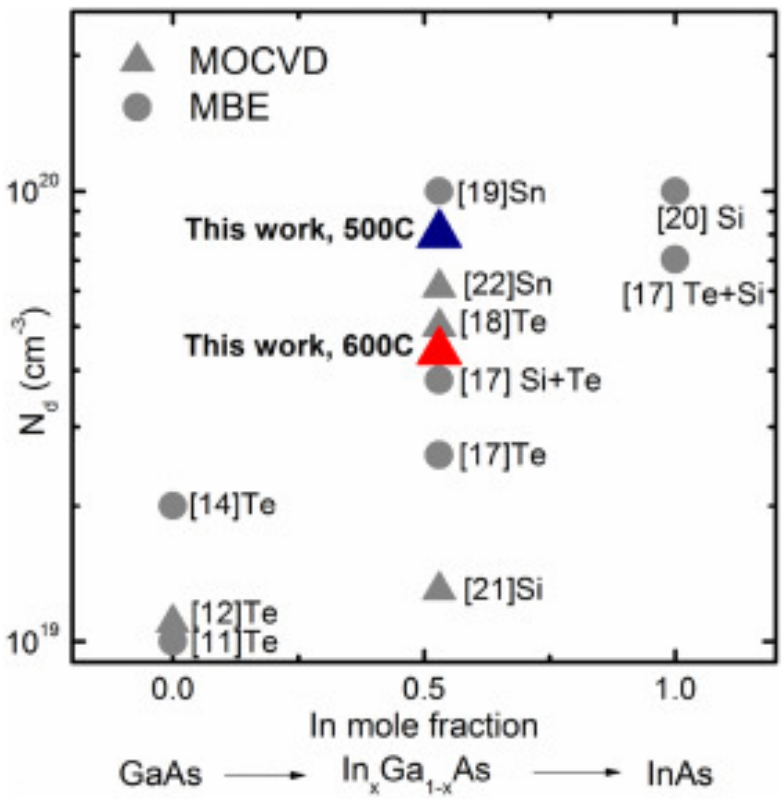

Figure 2.4: Net donor concentration for grown-in samples with various dopants as a function of indium composition. Te was used as the dopant for the points labeled "this work." Other InGaAs points are taken from [5, 6, 7, 8, 9]. High carrier concentrations are possible to achieve using grown in dopants. Reproduced with permission from Orzali *et al.* [10], copyright Journal of Crystal Growth 2015.

con dopants [11]. It is also interesting to note that, as the carrier concentrations increases, the mobility drops, presumably from scattering from ionized dopants. The Burstein-Moss shift was measured using photoluminescence, which shows the shift in the absorption edge relative to the band gap due to the Fermi level being pushed into the conduction band at high doping levels.

Even though samples can be grown with high carrier concentrations, an issue arises with further thermal processing. The high grown-in carrier concentra-

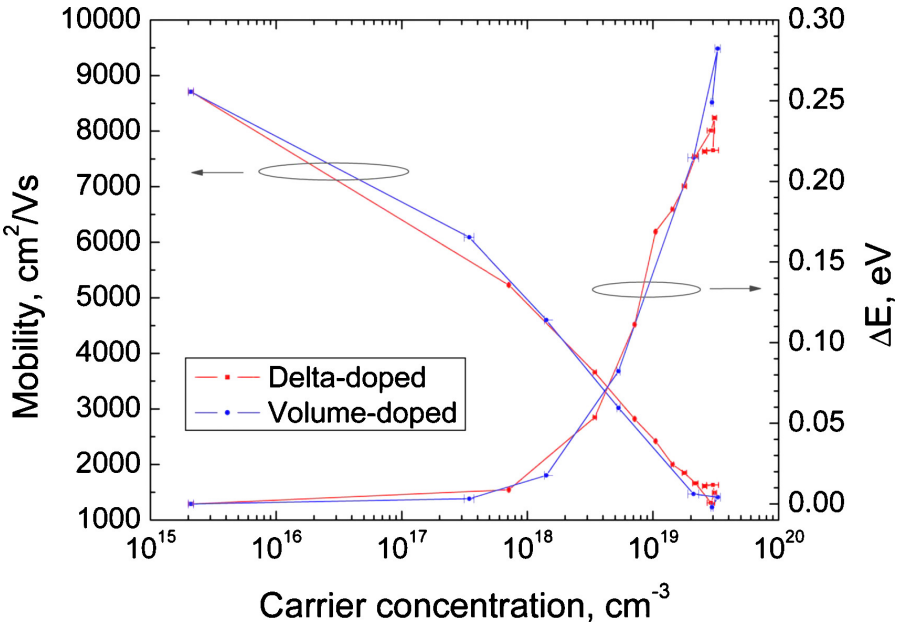

Figure 2.5: The electron mobility (left axis) and Burstein-Moss shift ΔE (right axis) as a function of the net donor concentration (x-axis) both delta and volume, silicon-doped $In_{0.53}Ga_{0.47}As$ grown by MBE. The circles and arrows are drawn to guide the eye to the correct axis. Reproduced with permission from Fedoryshyn *et al.* [11], copyright Journal of Applied Physics 2010.

tions are metastable and deactivate under 10-minute furnace anneals. Watanabe *et al.* initially reported this finding [82], and Lind *et al.* repeated this experiment and compared it to ion-implanted samples [83, 12], Figure 2.6 [83]. Both groups found that with furnace annealing for 10 minutes in an inert ambient (N_2 [82] or Ar [83]), the carrier concentrations in the capped, grown-in samples deactivated to a level of $\approx 1.4 \times 10^{19}$ cm^{-3}. Lind *et al.* found that ion-implanted samples activated with thermal annealing to the same level as that by which the grown-in samples deactivated. They hypothesized that compensating point defects form at equilibrium.

Another annealing study was performed in which the time scale of the an-

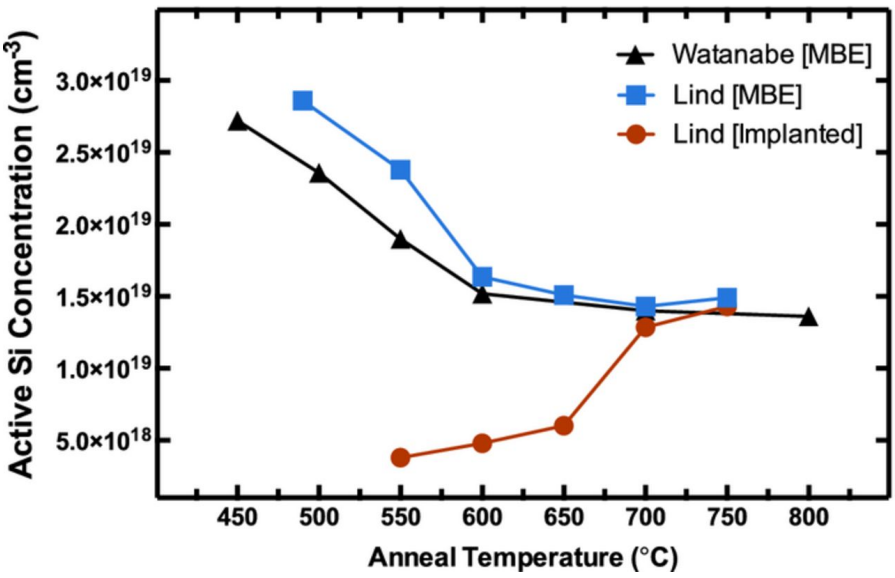

Figure 2.6: Net donor concentration in silicon-doped $In_{0.53}Ga_{0.47}As$ as a function of annealing temperature for 10-minute furnace anneals from Lind *et al.* The implanted samples activate to the same level that samples with grown-in dopants deactivate to, $\approx 1.4 \times 10^{19}$ cm^{-3}. Reproduced with permission from Lind *et al.* [12].

nealing was shortened for the high temperature anneals and lengthened for the long temperature anneals [12]. The results show roughly the same carrier concentration limit Figure 2.7, suggesting that longer times are needed for the lower temperatures to reach a equilibrium state. Since ion-implantation is a high-energy process that creates crystalline damage and dislocation loops that are difficult to anneal in III-V materials [84], it would be expected that the point defect populations in as-grown samples would be drastically different from the ion-implanted samples. It is thus rather surprising that both sets of samples are observed to reach the same state, even with a low temperature thermal anneal.

Traditional thermal processing methods, like RTA and furnace annealing, has been explored for InGaAs. It was found that ion-implanted samples could

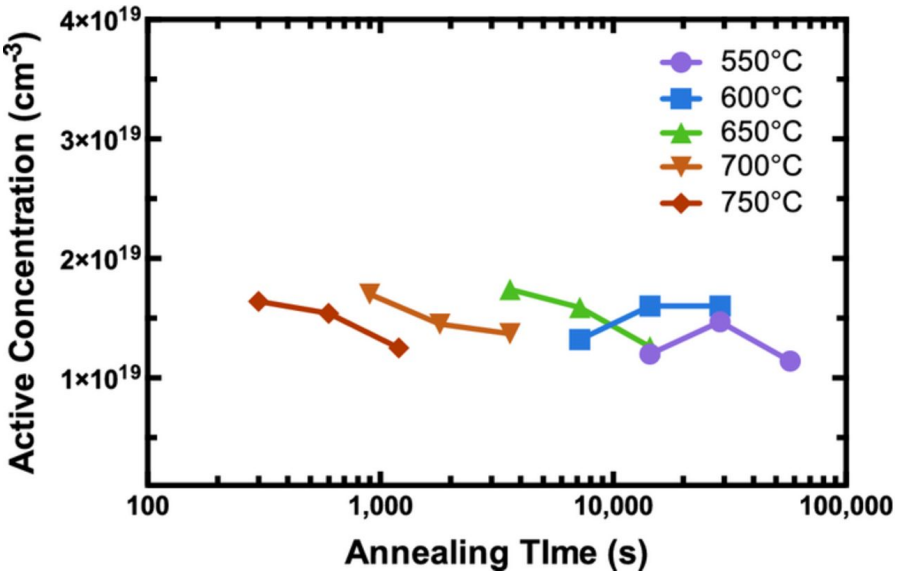

Figure 2.7: Net donor concentration in silicon doped $In_{0.53}Ga_{0.47}As$ as a function of annealing temperature and time for furnace annealed samples from Lind *et al.* [12]. The activation concentration for short annealing times at high temperature is the same as long annealing times at low temperatures.

be activated. The high annealing temperatures that are needed to repair crystalline damage and for dopant activation was problematic. The temperatures the samples could reach was limited by material decomposition, as the vapor pressure of As increases with an increase in temperature. The active concentration reached a limit of $\approx 1.4 \times 10^{19}$ cm^{-3}. Additionally, the longer annealing times used traditional thermal processing equipment leads to deactivation metastable dopants to the same $\approx 1.4 \times 10^{19}$ cm^{-3} level. This work is focused on understanding how the short time scales and high annealing temperatures fit within this picture, assessing the ability of LSA to repair the full range of defects and electrically activate ion-implanted dopants and its ability to maintain metastable dopant concentrations.

GaN

Since the majority of the work was carried out on InGaAs samples, only a few relevant articles for GaN will be cited here, with a focus on laser annealing results. One important point is that annealing temperatures above 1500 °C are needed to completely remove implantation damage in GaN; lower temperatures, ≈1200 °C, can only reduce damage in low dose implants [73]. This high temperature is not accessible using traditional annealing equipment but is accessible using laser annealing.

Using pulsed laser annealing, the crystalline damage in samples can be repaired. Vitali *et al.* found that using 10-30 low-power pulses of 25 ns with a Q-switched ruby laser could repair crystalline damage induced from implantation in GaN and InP, but higher power densities result in group V evaporation even before the occurrence of the melt [85].

In polycrystalline GaN, laser annealing with 20 ns pulses from a KrF excimer laser (λ = 248 nm) improved the structural and optical properties of the film [86].

Wang *et al.* used pulsed laser annealing to activate Be-implanted GaN [87]. They found that RTA alone could not efficiently repair the implantation damage and activate the implanted dopants. Using just laser annealing, the sample had good dopant activation, but crystal defects and strain remained. After pulsed laser annealing followed by RTA, the sample exhibited an acceptable degree of dopant activation, suitable surface morphology, and the defects caused by implantation were repaired.

In a related study, Feigelson *et al.* activated *p*-type implants in GaN using an initial 1 hr furnace anneal at 1050 °C to repair crystalline damage, followed

by cycling through high temperature processing for timescales less than 23 s between 1300 and 1400 °C to activate the dopants. The high temperature anneals activated *p*-type dopants while the limited annealing time prevented nitrogen evaporation [58].

In GaN, laser annealing has been explored as a method to activate ion-implanted samples and to repair crystalline damage that occurs from implantation. It was found that laser annealing using pulsed lasers can improve crystalline quality and activate dopants, but for the best results, a lower temperature, longer time scale anneal step should be combined with the laser anneal to repair crystalline damage and defects formed during implantation.

2.2 Summary

III-V compound semiconductors have a wide-range of tunable structural, electrical, and optical properties, making them useful for a wide variety of electronic and optoelectronic applications, like photovoltaics, LEDs, lasers, and photo detectors. However, challenges still remain if the industry is to incorporate these materials into high performance, next-generation transistor fabrication. The major among them, from the point of view of this thesis, is to resolve the complications that arise from intentional and unintentional defects, which can have an enormous impact on semiconductor properties. Processing plays a large role in determining what defects will be created and destroyed. Of particular importance is the thermal annealing, which is necessary for activation of ion-implanted dopants and for the repair of implantation related crystalline damage. However, annealing temperatures for long timescale anneals are lim-

ited by thermal decomposition of the material from the evaporation of the group V atom. Longer timescale also deactivate films with high active carrier concentrations. Thus, it is of utmost importance to understand the role of processing and its relationship to material properties. In this work, we are interested in how short timescale, high temperature laser spike annealing affects the structural and electrical properties of III-V materials, specifically intrinsic and doped InGaAs and GaN.

CHAPTER 3

METHODS

3.1 Laser Annealing

3.1.1 Laser Annealing Set-up

Laser annealing in the Thompson research group uses a high power, continuous wave laser focused onto a moving stage to rapidly heat and quench samples at a rate on the order of 10^4 – 10^7 K/s. By tightly focusing the laser in the scan direction and quickly moving the sample under the laser, we can explore short annealing times (on the order of sub-millisecond to millisecond timescales) and probe states that are kinetically limited, rather than thermodynamically limited. The variables that we control in our set up are the choice of laser we use (determining the wavelength of light used to anneal), the speed at which we scan the laser over the stage (captured in the dwell or annealing time), and the power of the laser. In laser annealing processes, it is common to anneal to a roughly uniform temperature by rastering overlapping laser scans across the sample. Our set-up can easily do this; however, the Thompson group has found that a *single* laser scan can be used as a powerful combinatorial technique that quickly screens the effect of laser annealing temperature for a given dwell on a material [13]. By intentionally defocusing our laser perpendicular to the scan direction, we can probe the effect of annealing temperature over a range from the substrate temperature of an unannealed control location (far away from the center of the laser scan) to the highest annealing temperature (occurring in the middle of the scan). This produces temperatures that vary as a function of posi-

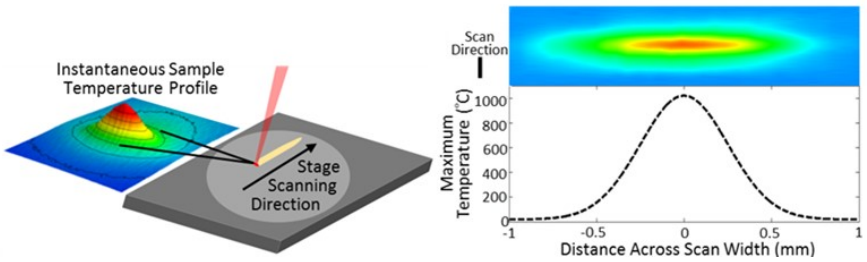

Figure 3.1: Schematic of the single scan laser annealing set-up (left) and profiles of the CO_2 laser power density (top-right) and perpendicular temperatures (bottom-right). The laser is scanned over the sample, creating an annealing temperature gradient based on the sample position. Reprinted with permission from Bell *et al.* [13]. Copyright 2016 American Chemical Society.

tion on the sample, as illustrated in Figure 3.1.

There are two continuous wave infrared lasers used for annealing samples in our lab. One is a CO_2 laser (P_{max} = 130 W, λ = 10.6 µm) and the other is a diode laser (P_{max} = 250 W, λ = 980 nm). The coupling between a material and the laser is dependent on the wavelength of the laser light.

The beam of the CO_2 laser is focused to maintain a broad Gaussian shape in the x-direction and a narrow Gaussian shape in the y-direction, as shown in Figure 3.2(a). The x-axis of the diode beam is focused to achieve a profile with a roughly flat top with the y-axis focused to a Gaussian shape, see Figure 3.2(b). The lasers are scanned in the direction of the short axis, in this case, the y-axis.

We define annealing times by dwell, which is the full width half max (FWHM) of the laser focus in the scan direction divided by the velocity of the moving stage (*e.g.*, a 88.4 µm FWHM value observed at a speed of 88.4 mm/ s would correspond to a 1 ms dwell). Typically, we use dwells ranging from 150 µs to 10 ms. We define the peak laser line power density, I_0 (W/cm), in Equa-

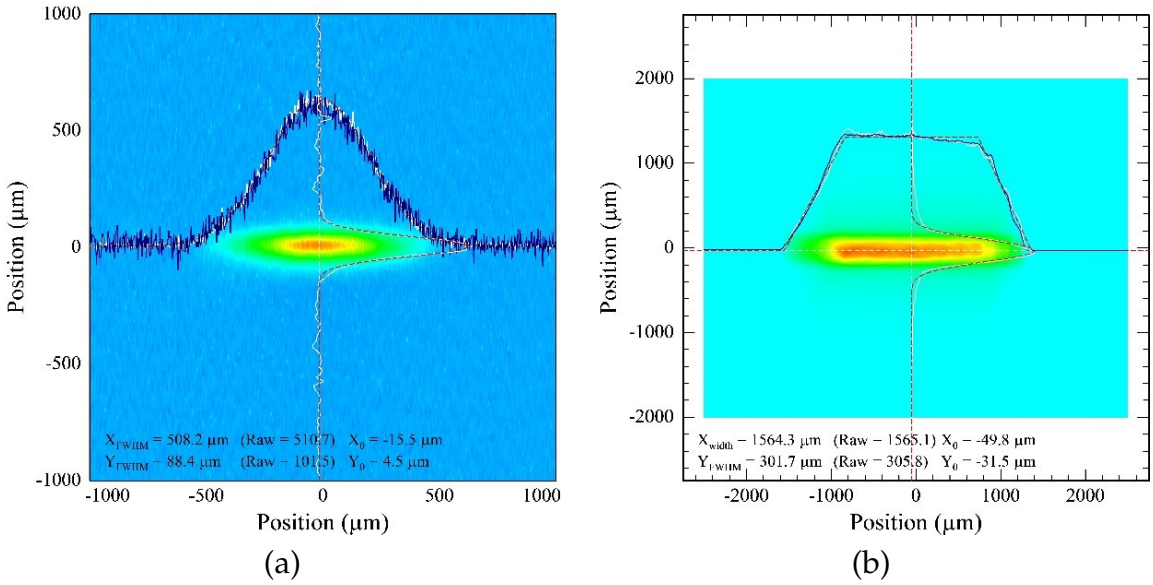

Figure 3.2: Representative laser power density profile for the (a) CO_2 laser and the (b) diode laser. In both cases, the laser is scanned in narrow axis, in the *y*-direction to quickly heat and quench the samples. The *x*-axis is broadly focused, to allow for spatially resolved temperature measurements.

tion 3.1. The line power density can be calculated using the laser power, P (W), and the FWHM (cm) perpendicular to the scan direction [88].

$$I_0 = \frac{2P_0}{FWHM}\sqrt{\frac{ln(2)}{\pi}} \tag{3.1}$$

In order for the laser to heat a material, the laser must interact with it in some way, directly or indirectly. The critical material properties for laser coupling are the absorption and reflectivity of the material at the laser's wavelength. The laser can couple with a thin film, substrate, or an absorber on the top of, or within, the stack. The heating of the film is determined by its thermal and optical properties. The optical properties (reflectivity and absorption) will determine how much and how strongly the light is absorbed and the thermal prop-

erties (thermal conductivity and heat capacity) determine heat transfer through the materials. Many of these properties have a strong temperature dependence, making it non-trivial to predict the thermal annealing profiles [89].

3.1.2 Challenges

One of the challenges associated with laser annealing experiments involves understanding how the laser interacts with the sample that we want to heat. The frequency of the CO_2 laser is such that it couples with heavily doped samples by oscillating free carriers, thereby heating the sample. This method is widely used in our lab to heat heavily doped silicon, but can be used for other materials as well. Direct bad gap absorption can be used to heat the sample if the energy of the laser is larger than the energy of the direct band gap of the sample.

Table 3.1 provides a comparison of the band gaps of the materials used in this thesis to the lasers used in our lab. The conversion between wavelength and energy is shown in Equation 3.2; where E is energy, h is Planck's constant, c is the speed of light, and λ is the wavelength [90] (hc is 1239 in units of eV nm). If the direct band gap of a material is less than the energy of the laser, the sample can absorb the laser light. From the information provided in Table 3.1, it is evident that the energy of the light from the CO_2 laser will not heat any of the samples by direct band gap absorption, but the shorter wavelength diode laser should couple with either $In_{0.53}Ga_{0.47}As$ or InAs through this mechanism.

$$E = \frac{hc}{\lambda} \tag{3.2}$$

Table 3.1: Summary of the direct band gap of III-V materials used in this study and the energies of the lasers used to anneal them. For direct band gap light absorption, the material must have a band gap energy that is smaller than the energy of the light.

		Energy [eV]	**Wavelength [nm]**
Material	$In_{0.53}Ga_{0.47}As$	0.75	1653
	InP	1.35	918
	InAs	0.36	3443
	GaN	3.4	365
Laser	CO_2	0.117	10600
	Diode	1.26	980

Beyond direct band gap absorption, a material's optical properties give a more complete description of the light/matter interaction. Relevant optical properties for materials of interest for this thesis are displayed in Table 3.2. This table displays the index of refraction (n), the extinction coefficient (k), the absorption coefficient (α), and the reflectivity (R). The optical properties for each material are dependent on many factors, including wavelength, temperature, and the extent of its doping. The data compiled in the table are taken at 300 K and are summarized for the closest conditions to the laser energies (0.12 eV for the CO_2 and 1.3 eV for the diode) that are available from Adachi [90], with linear interpolation used if there are sufficient data. The critical parameters for laser annealing are the absorption length ($1/\alpha$) and the reflectivity, which are related to n and k. The absorption lengths describes how strongly the light is absorbed and converted to heat, where a short length indicates strong absorption. The

reflectivity indicates the amount of light that bounces off the sample rather than being transmitted into the sample. For a sample to be heated, a portion of the light must be transmitted to the sample and then absorbed. It is important to note that capping layers added to the sample may modify this interaction.

Table 3.2: Summary of optical properties for materials of interest in this thesis. The optical properties are dependent on the wavelength of light used. The most practical parameters are absorption length ($1/\alpha$) and reflectivity (R). A small absorption length means that the sample strongly absorbs the light. Additionally, the lower the reflectivity, the more light is transmitted to the sample.

Material	**Laser Energy [eV]**	n	k	α [cm^{-1}]	**Absorption Length** [μm]	R
InGaAs	0.12	NA	NA	NA	NA	NA
	1.3	3.66	0.288	3.71×10^4	0.269	33%
InAs	0.1	3.40	0.00021	2.11	4740	30%
	1.5	3.71	0.432	6.57×10^4	0.152	34%
InP	0.13	3.05	0.00011	1.15	8710	26%
	1.3	3.36	0.00029	38.0	263	29%
GaN	0.12	1.81	0.018	216	46.3	8%
	1.3	2.34	NA	NA	NA	16%

An additional challenge comes from characterizing the sample after annealing. Each position on the sample relative to the annealing scan corresponds to a different annealing temperature. Characterization techniques that probe large volumes will average many different annealing temperatures together. In order

to resolve small temperature differences, characterization techniques must have good spatial resolution, as described in more detail below.

3.2 Characterization

There are numerous techniques that our group uses to characterize samples, chosen based on the properties we want to probe. Patterned resistors, thermal decomposition behavior, phase changes, and thermal damage are used to characterize annealing temperature [13, 89, 91]. To characterize electrical properties, we can use traditional electrical measurements adapted to small areas, or use other methods that probe properties of interest in a more indirect manner, as described below.

3.2.1 Annealing Temperature

Temperature calibrations were performed on the surface of the III-V films. Platinum thin film resistors, with a linearly varying resistivity with temperature, were used to establish relative temperatures both as a function of laser power and across the laser scans for each dwell. These resistors were fabricated on a 50 nm PECVD SiO_2 layer deposited on the III-V films to electrically insulate the sample from the thin film resistor. The samples were then packaged and wire-bonded, as shown on the left in Figure 3.3. The platinum resistor was passed underneath the laser and the resulting resistance, which is directly proportional to temperature, was measured *in situ* [89, 91, 13]. The resistor was measured using a 4-wire technique, with the current controlled through the two leads in

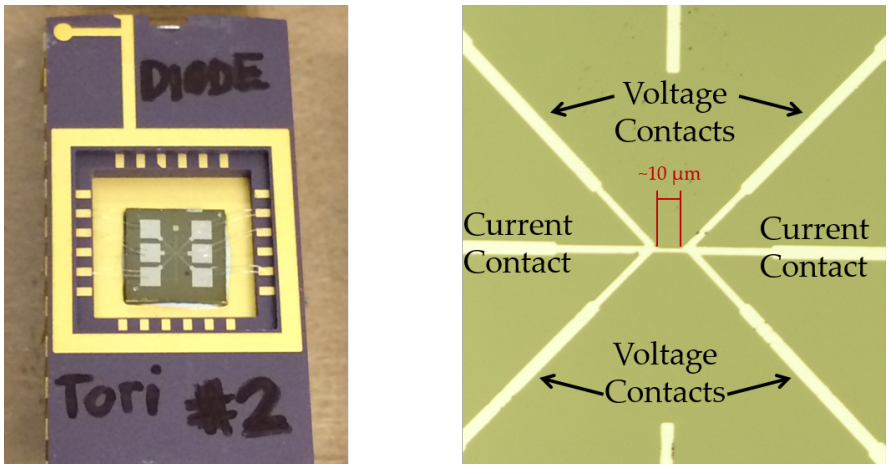

Figure 3.3: Platinum thin-film resistor fabricated on a InGaAs sample. Left: The packaged Pt resistor. Right: A bright field micrograph of the resistor. The resistors are used to provide relative temperature measurements as a function of time and position relative to the laser.

the center and the voltage measured through two other leads, as shown on the right in Figure 3.3.

For each dwell, we calibrated peak temperatures as a function of laser power against the maximum observed resistance. In addition, the resistors were used to profile the lateral temperature across the laser scans by systematically translating the 20 µm wide resistor probe. These calibrations are critical to interpretation of the spatially resolved properties. Due to damage limitations on the platinum films, measurements were taken up to a peak temperature of ≈600 °C.

Absolute temperatures were established using gold dots that melt when the temperature exceeds 1064 °C and the thermal decomposition behavior of the block copolymer poly(styrene-*block*-methyl methacrylate), 70 wt.% polystyrene [89, 91]. Between 650 and 1050 °C, the dwell-dependent thermal decomposition behavior of a 60 nm block copolymer thin film was compared to

well-calibrated behavior on heavily doped Si substrates. A schematic of how the polymer decomposition temperature calibration is conducted is shown in Figure 3.4.

Figure 3.5a shows an image of a silicon wafer with the spun polymer under both a diode laser anneal (top of the image, shown as thick stripes) and a CO_2 laser anneal (middle and bottom of the wafer, shown as thin stripes). This image emphasizes the drastic difference in the beam size between the two lasers. The visible white stripes are where the laser has scanned over the sample and the polymer has subsequently thermally decomposed.

For the CO_2 scans, the temperatures marked on the image in Figure 3.5a show the peak annealing temperature of the scan, ranging from 700 °C to 1100 °C. The dwells ranged from 150 µs to 10 ms, increasing in annealing time from left to right within each temperature group (150 µs, 250 µs, 500 µs, 1 ms, 2 ms, 5 ms, and 10 ms).

For the diode laser scans, we used dwells from 5 ms to 30 ms. The first three scans in Figure 3.5a were 5 ms scans at peak temperatures of 700 °C, 800 °C, and 900 °C. The other sets of scans in Figure 3.5a were carried out with a maximum annealing temperature of 900 °C, 1000 °C, and 1100 °C, respectively. Within these groups, the dwells were increased from left to right (10 ms, 20 ms, and 30 ms).

An increase in annealing temperature from the laser causes the polymer to thermally decompose, resulting in a decrease in thickness of the polymer. The change of thickness of the polymer was initially explored using profilometry. The change in thickness as a function of position was converted to a function of laser annealing temperature using relationships that are well-established for sil-

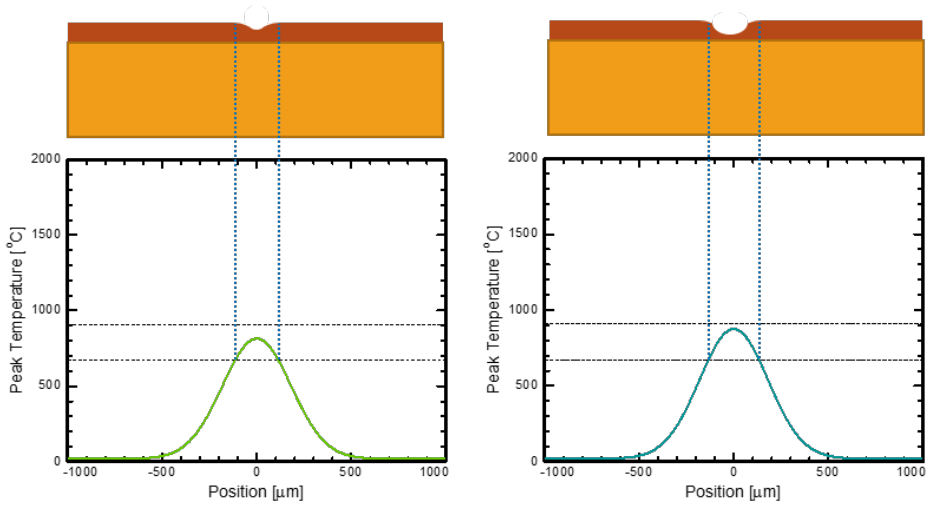

(a) Partial Decomposition (b) Partial Decomposition

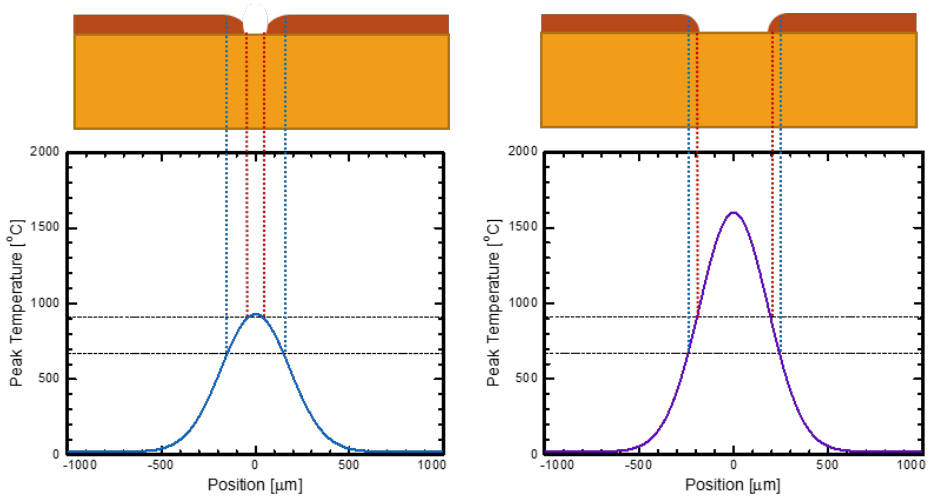

(a) Full Decomposition (b) Full Decomposition

Figure 3.4: A schematic of the absolute temperature calibration for laser annealing using polymer decomposition. The top of the image shows a sketch of the substrate with a thin polymer layer on top after laser annealing. Beneath the sketch shows the spatial temperature distribution of the laser annealing scan. As the laser power is increased, the temperature of the substrate increases. Above a dwell-dependent threshold temperature, the polymer begins to decompose, as evident in (a) and (b), with the blue dotted lines marking the position and temperature that partial decomposition occurs on the sample. As the laser power is increased further, the polymer reaches high enough temperatures to also completely decompose as shown with red dotted lines in (c) and (d).

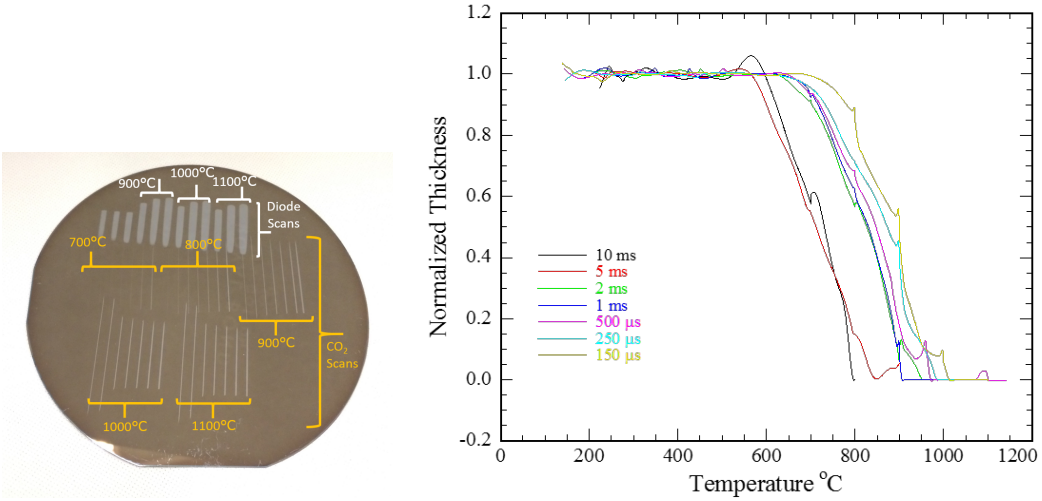

Figure 3.5: Absolute temperature calibration for laser annealing using polymer decomposition on a well-calibrated, heavily doped silicon wafer: (a) shows a image of the silicon wafer and the annealing scans used for the calibration; (b) shows the change in thickness of the polymer measured by profilometry as a function of annealing temperature. As the annealing time is increased, the polymer decomposes at lower temperature. The decomposition behavior of the polymer on the silicon control sample was then used to determine the laser annealing temperatures on the III-V samples.

icon in our lab, as shown in Figure 3.5(b). In this figure, multiple scans with differing peak temperatures are averaged together within each dwell for the CO_2 laser. The profilometry data were analyzed in greater detail for each scan, the width was found for 20% decomposition and full decomposition and converted to temperature for each scan. The 20% decomposition was easier to identify from the data compared to the start of decomposition. The annealing time and temperature for these decompositions were used to find the activation energy for decomposition using an Arrhenius plot. The results from the Arrhenius plot was used to find the 20% and 100% decomposition temperatures for each dwell.

Additionally, it was found that micrographs from optical microscopy could be used to access polymer decomposition, which became our preferred method due to its relative ease and speed for data collection and analysis. Images from either dark field and bright field images can be used, as will be explained next. For samples with high numbers of defects, the dark field images are more difficult to analyze, so bright field images are preferred in that case. In the dark field images, the start and end of the polymer decomposition appears as bright light scattering lines. Figure 3.6 shows an example of this for the CO_2-annealed silicon for a 5 ms dwell with a peak temperature of (a) 800 °C and (b) 900 °C. The two lines in Figure 3.6(a) mark the position where polymer decomposition starts to occur. Figure 3.6(b) has two sets of lines, the outer lines marking the start of polymer decomposition and the inner lines marking complete polymer decomposition. Between these two figures, it is clear that the the polymer completely decomposes between 800 °C and 900 °C. The widths between the decomposition lines were analyzed for each scan and the line widths were converted to temperature for each scan. As with the profilometry data, the annealing time and temperature for these decompositions were used to find the activation energy for decomposition. This is achieved using an Arrhenius plot which is then used to find the decomposition temperature which these inner and outer lines appear.

The polymer decomposition results for both methods, profilometry versus image analysis, are summarized in Table 3.3. In general, relationship between the polymer decomposition temperature and annealing time is as expected for both methods. As the dwell time increases, both the start of polymer decomposition and complete decomposition occurs at lower temperature. Thus, the longer the heating time for the sample, the lower the decomposition tempera-

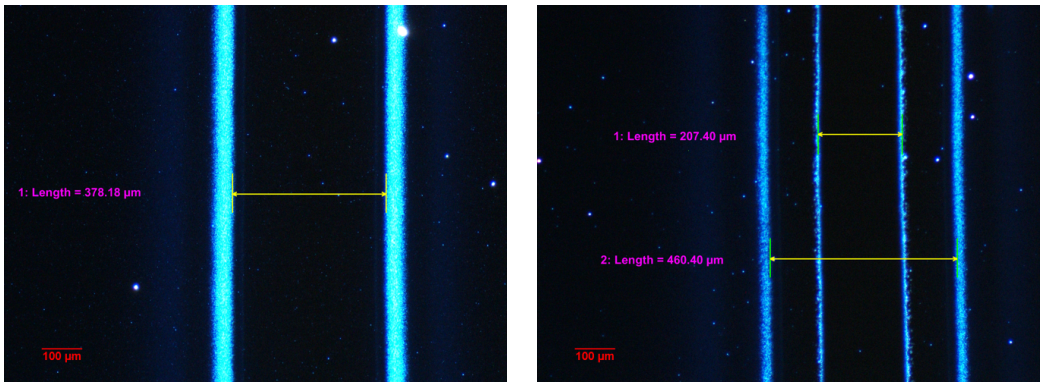

(a) (b)

Figure 3.6: Dark field micrograph of the polymer decomposition on silicon for a 5 ms CO_2 anneal with a peak temperature of (a) 800 °C and (b) 900 °C. The single set of lines in (a) show the position on the sample where the polymer has begun to decompose. The double set of lines in (b) show the polymer has completely decomposed (outer lines are the beginning of decomposition, inner lines are complete decomposition).

ture of the polymer. The difference between the two methods is summarized in the last two columns of the table. Comparing the two methods, the start of decomposition using profilometry (20% film loss) to the dark field images (the outer lines), it is evident that the outer lines of the dark field images have a lower temperature by roughly 90 °C. This is because the outer lines in the dark field images mark the beginning of film loss, rather than 20% film loss, which takes place at a higher temperature. The difference between the complete decomposition behavior is less consistent. This is most likely a result of the difficulty of clearly identifying complete decomposition of the polymer with profilometry. Additionally, the finite tip size may induce some error into the profilometry measurement.

In order to be a good temperature calibration, the polymer should be optically transparent to the lasers, with decomposition only occurring if the sub-

Table 3.3: Summary of polymer decomposition temperatures found from profilometry and dark field images. The dark field micrograph data was easier to collect and analyze. Compared to the profilometry data, the dark field images had larger initial and full polymer decomposition widths, that led to consistently lower predicted temperatures.

Dwell	**Decomposition Temperature** [°C]					
[ms]	**Profilometry**		**Dark Field**		**Difference**	
	20%	**100%**	**Start**	**End**	ΔT_{Low}	ΔT_{High}
0.150	898	1151	814	1028	84	123
0.250	856	1093	769	991	86	102
0.500	803	1021	714	943	89	78
1	755	956	664	899	91	57
2	712	898	620	858	92	40
5	660	829	567	809	93	21
10	624	782	531	774	93	8

strate reaches a high enough temperature to thermally decompose the polymer. To ensure that the polymer was transparent to the CO_2 laser, it was spun on a semi-insulating silicon wafer that does not couple with the laser and annealed at the highest accessible power (130 W). After annealing, the polymer showed no evidence of decomposition. This test was repeated with a sample that did not couple with the diode laser (InGaAs:Te on Si substrate) and it was confirmed that the polymer also did not decompose under the strongest illumination of the diode laser (250 W).

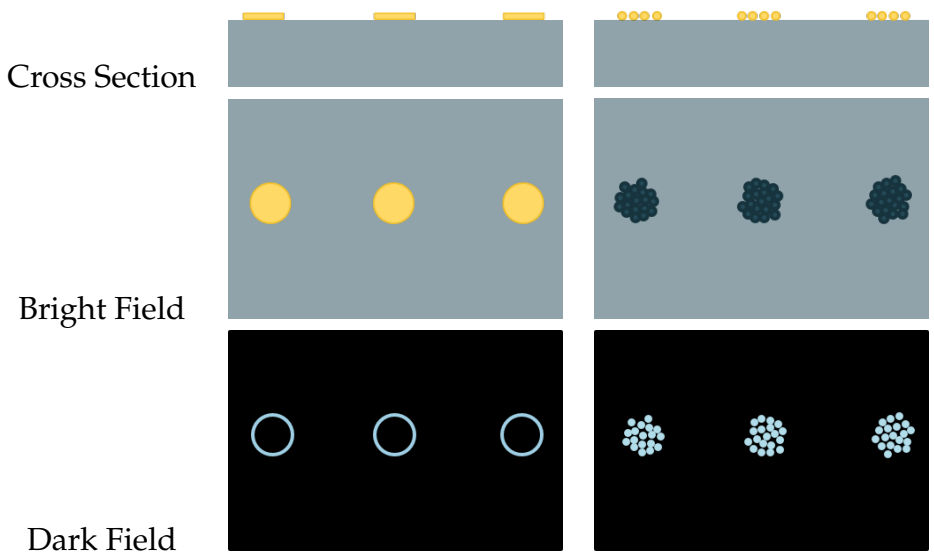

Figure 3.7: Schematic description of the gold dot melting experiments showing the appearance of gold dots: (a) before melting; and (b) after melting. The cross sectional view (top) shows what the individual dots look like before and after melting. The bright and dark field images show what dots look like in the microscope before and after melting.

For higher temperature calibrations, 1.5 nm of Cr (to promote adhesion) and 25 nm of Au were thermally evaporated onto 50 nm PECVD SiO_2-coated samples, which were then photolithographically patterned to define lines of 5 µm gold dots, laterally spaced on 10 µm centers. When the dots are heated above the melting temperature of gold (1064 °C), the surface tension causes the gold to dewet and separate into smaller beads. The gold that melted was clearly visible in both bright and dark field micrographs. A schematic is the gold dot calibration is shown in Figure 3.7. A laser-annealed sample used for temperature calibrations is shown in Figure 3.8, with the sample temperature exceeding gold melt as shown by the 3-5 melted dots in the center of images when the laser has passed.

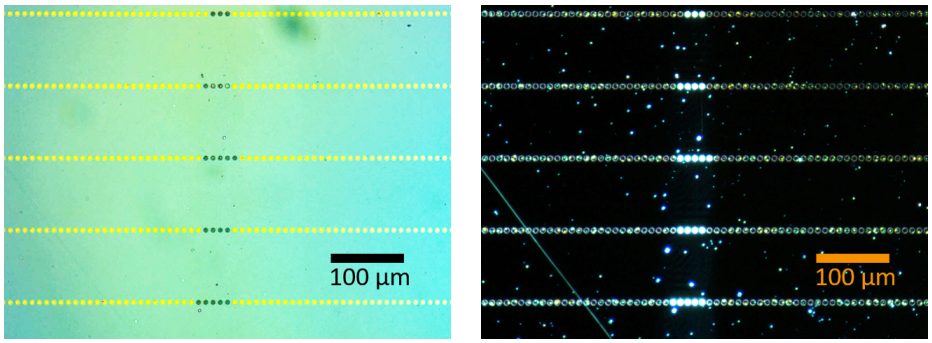

(a) Bright Field (b) Dark Field

Figure 3.8: Absolute temperature calibration for the laser annealing of InGaAs films using the melting temperature of gold as the reference. The melted gold dots are clearly visible in the center on the sample and appear dark in the bright field micrograph (a), and bright in the dark field micrograph (b). The melted dots show the position on the sample that has exceeded 1064 °C.

Material Damage

Laser annealing can reach high temperatures in short periods of time and, above a critical temperature threshold, laser annealing can cause irreversible damage to a material. This damage is what limits the temperatures that laser annealing can reach. In order to explore the complete range of accessible temperatures during non-melt laser annealing, our lab often anneals the samples up to the point at which they damage. This can be manifested in the form of slip, cracking, evaporation, or melt. Depending on the type of damage, it may be possible to extend the range of annealing temperatures that can be reached by limiting or preventing the extent damage. For example, if arsenic evaporation is the cause of the damage, capping layers can be used to extend the damage threshold. Of the types of damage that occur, the temperature at which melt occurs is easiest to quantify. Many groups have reported laser-induced periodic surface structures (LIPSS) on laser-annealed compound semiconductors [92, 93, 94, 95]. This

damage, also known as "ripples" occurs from the interference of the incident laser light with the scattered light, causing surface instabilities and inducing localized melt [95]. The melting temperatures for relevant materials for this work are summarized in Table 3.4 [1].

Table 3.4: The melting temperature for III-V binaries and silicon from [1]. Temperatures during laser annealing are often difficult to characterize and can be high enough to melt films. These temperatures can be used as a rough guide for the temperature at which laser annealing will damage the films through melt.

Material	T_m [°C]
Si	1414
GaAs	1240
InAs	937
InP	1062
GaN	2518

The values in this table show that InP (T_m= 1062 °C) and gold (T_m= 1064 °C) melt at approximately the same temperature. This makes using gold dots as a temperature calibration especially valuable because gold melt and sample damage occur at the same position, than the sample damage is most likely related to InP melt. Slip or cracking damage during laser annealing is also common at high temperatures. Because of large thermal gradients, localized stress can occur from thermal expansion, causing damage. In layered materials, an additional complication arises as a result of differences in thermal expansion between the layered materials, as discussed in the Background section.

3.2.2 Electrical Properties

There are a wide variety of techniques to probe the electrical properties of semiconductors, which have been tested and used extensively [96]. Many of the traditional methods for measuring electrical properties are so-called "contact" methods, where the semiconductor is physically contacted and, hence, is often destructive to some degree. A large emphasis is typically placed on measuring intrinsic electrical properties of the material that are important in determining how a semiconductor device will function (carrier density and mobility) and so that results can be compared across different samples. One common method often used for electrical measurements involves four-point probes, which measure sheet resistivity by passing a current through two contacts and measuring the voltage through two other contacts. Sheet resistivity is related to the bulk resistivity (ρ) in Equation 2.2 through the thickness of the conductive layer thickness (t), as shown in Equation 3.3. The sheet resistivity cannot directly measure carrier concentrations, mobility, or layer thickness. The sheet carrier density (or sheet number) and mobility can be found from Hall measurements, which use electrical measurements in a magnetic field.

$$\rho = \frac{1}{ne\mu_n + pe\mu_p} = \rho_{\square} t \tag{3.3}$$

On laser-annealed samples, the annealing conditions vary with position. In order to probe electrical properties that change with position, we use modified versions of traditional electrical measurement techniques adjusted to smaller sizes. This technique has been used successfully by other groups to differentiate changes in electrical properties of samples that were annealed with overlapping laser scans [97]. By using spatially resolved probes, variations in electrical prop-

erties could be seen as a function of where the scan was made which would not be apparent for probes with poorer spatial resolution.

3.2.3 Optical Properties

Another powerful method used for characterization is Raman spectroscopy which collects the signal from inelastic light scattering events. Since its discovery in 1928 [98], it has been used extensively across many fields as a non-destructive characterization technique [99, 100]. Raman spectroscopy has been used to investigate a variety of III-V materials beginning in 1966 [101] and shortly after was used to probe free electron concentrations in *n*-type GaAs, showing the first example of scattering by conduction-electron plasmons [102, 103]. Raman spectroscopy is still widely used today to study III-V materials [104, 105].

An excellent review by Ibáñez and Cuscó *et al.* describes the characterization of compound semiconductors using Raman spectroscopy, which forms the basis of much of the following description [104]. For III-V materials, Raman is commonly used to assess properties like composition, crystalline quality, stress, impurities, and free carriers. In Raman spectroscopy, a single wavelength of light illuminates the sample. The majority of that light is elastically scattered, or Rayleigh-scattered, where the light changes direction but does not gain or lose any energy. A very small portion of the photons, around 1 out of every million, is inelastically scattered and either loses or gains energy. The former is called Stokes-Rayleigh scattering and the latter is called anti-Stokes Rayleigh scattering. These are the scattering events that are collected and analyzed in Raman

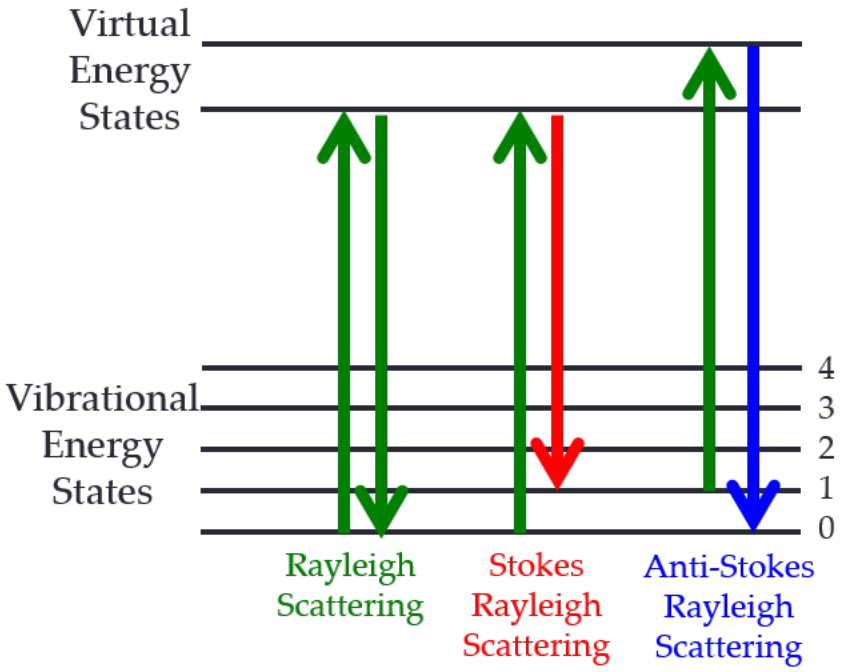

Figure 3.9: Schematic describing Raman scattering in terms of the inelastic Stokes and anti-Stokes scattering. Raman probes vibrational energy states by illuminating the sample with a single wavelength of light and collecting the inelastically scattered light that excited vibrational states in the crystal.

spectroscopy. The different types of scattering are summarized in Figure 3.9.

During these inelastic scattering events, the energy lost (or gained) by the light is transferred to (or from) the sample and excites vibrations within the crystal like phonons (lattice vibrations) and local vibrational modes from defects. The vibrational energy states in a crystal are quantized, so energy changes happen at well-defined frequencies. Thus, Raman has proven to be a powerful tool to probe the vibrational states of the crystal. Depending on the orientation of the crystal structure with respect to the polarization of the incident and scattered light, different phonon modes are excited, or allowed. For a deeper understanding, Hayes and Loudon wrote an outstanding reference for the the-

ory of light scattering in crystals [106].

This work used a 488 nm wavelength laser source in a Renishaw InVia microRaman system, used in the backscattering configuration with a 1 μm probe diameter. Raman spectra were collected perpendicularly across each laser scan. Primary phonon modes were fitted to Lorentzian peaks [107, 108]. In InGaAs, the area of the primary GaAs-like longitudinal optical (LO) phonon peak was used to qualitatively assess crystalline quality in undoped samples and, prior to substantial carrier activation, in doped samples. At high carrier concentrations, the macroscopic electric fields of the LO phonon mode couples with the longitudinal plasmon mode. This coupling results in a longitudinal optical phonon-plasmon coupled mode (LOPCM). This behavior takes place in polar semiconductors with high carrier mobility and low effective masses. Figure 3.10 shows a typical Raman spectrum for a laser- annealed InGaAs sample with the high frequency LOPCM peak near 850 cm^{-1} shown magnified.

In contrast to sheet conductivity measurements that determine only the total sheet carrier density, the LOPCM position directly probes the concentration of the active carriers within the probe volume (depth for InGaAs $\approx 2.3/2\alpha$ = 46 nm) [109, 105]. The relationship between phonon-plasmon coupled modes and *n*-type carrier concentrations have been widely modeled for a variety of compound semiconductors [103, 110, 111, 14, 18, 16, 17, 112, 113, 114]. The peak position of high frequency LOPC mode is highly sensitive to changes in the number of free carriers, and was thus was used to quantify carrier density [14, 15, 19, 16, 17, 115, 116, 117].

The frequency of the LOPCM corresponds to the zeros of the wavevector and wavenumber dependent (q, ω) dielectric function of the material, $\varepsilon(\omega)$, as

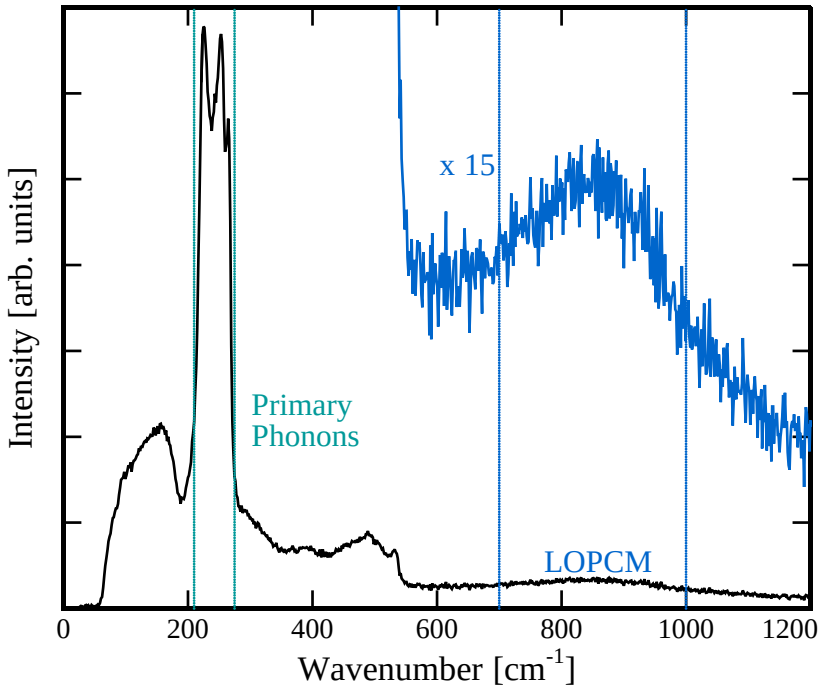

Figure 3.10: Typical Raman spectra from an LSA-activated sample. The primary InAs and GaAs-like phonon modes dominate the spectra between 210 and 275 cm^{-1}. The inset highlights the LOPCM peak near 850 cm^{-1}. The primary phonons can be used to probe composition, stress, and crystalline quality. The LOPCM peak can be used to probe the properties of the free electrons.

shown in Equation 3.4 [104, 105]. By neglecting Laudau damping and dispersion effects ($q = 0$), we can easily solve the equation using the quadratic formula to find the frequency of the LOPCM peaks. The first term, ε_∞, is the high frequency dielectric constant of the material and represents the contribution from the valence electrons. The second term, χ_I is the electric susceptibility of the ionic lattice, Equation 3.5, which relies on the phonon frequencies, ω_{LO} and ω_{TO} The third term, χ_e is the contribution from the dielectric susceptibility of the free-carrier plasma, which depends on carrier concentration; see Equation 3.6.

$$\varepsilon(q,\omega) = \varepsilon_\infty + 4\pi(\chi_I(w) + \chi_e(q,\omega)) = 0 \tag{3.4}$$

$$\chi_I(w) = \frac{\varepsilon_\infty}{4\pi}\frac{\omega_{LO}^2 - \omega_{TO}^2}{\omega_{TO}^2 - \omega^2} \tag{3.5}$$

$$\chi_e(q,\omega) = \frac{\varepsilon_\infty}{4\pi}\frac{\omega_p^2}{\omega^2} \tag{3.6}$$

$$\varepsilon(0,\omega) = 0 = (\omega^2)^2 + (-\omega_p^2 - \omega_{LO}^2)(\omega^2) + \omega_p^2\omega_{TO}^2 \tag{3.7}$$

$$\omega_\pm^2 = \frac{1}{2}\left[\omega_{LO}^2 + \omega_p^2 \pm \sqrt{(\omega_{LO}^2 + \omega_p^2)^2 - 4\omega_p^2\omega_{TO}^2}\right] \tag{3.8}$$

By taking the Drude form of the plasma (Equation 3.9, where e is the elementary charge and m^* is the effective mass of an electron), the frequency can be determined as a function of carrier density; see Equation 3.8 (To convert the angular frequency to wavenumber, divide by $2\pi c$, where c is the speed of light).

$$\omega_p^2 = \frac{4\pi n_e e^2}{\varepsilon_\infty m^*} \tag{3.9}$$

The two solutions emerge in Equation 3.8 as the high frequency coupled mode (ω_+ or L^+) and the low frequency coupled mode (ω_- or L^-). The only variable is n_e, so an increase in carrier concentrations will increase the plasmon-like peak. For low carrier concentrations, the L^- peak is plasmon-like and the L^+ is phonon-like, around the LO frequency. At high carrier concentrations,

the L^+ peak is plasmon-like and the L^- is phonon-like, around the TO phonon frequency.

This is the most simplistic Drude model and, as such, can yield significant errors. There are other, more accurate models used to fit experimental results; they differ based on the dielectric functions used for the electron and phonon contributions. They can be used for improved accuracy of the peak position as well as the line shape of the peak. The hydrodynamic model is a improvement over Drude and takes into account wavevector- dependent plasma frequency [118]. Hon and Faust developed a line shape model based on fluctuation-dissipation theory [119]. The Lindhard-Mermin model is a quantum mechanical approach, which is accurate but computationally expensive [14, 120]. This model can also reproduce the change in LOPCM peak position and shape based on the wavelength of the scattered light used in Raman [120].

Figure 3.11 and Figure 3.12 shows the relationship for plasmon-phonon coupled modes for InGaAs and GaN, respectively. The position of the LOPCM peak has been previously calibrated to the active carrier concentration in InGaAs in a number of experiments as well as theoretically modeled [14, 15, 16, 17], summarized in Figure 3.11. A power law fit was used as a calibration to convert the observed high frequency LOPCM peak position to active carrier concentration.

These coupled modes can be effectively used to quantify carrier concentrations above 10^{17} cm^{-3}. Figure 3.11 shows for InGaAs, the high frequency coupled mode is most sensitive to changes in the carrier concentration. For GaN, Figure 3.12 shows that the the low frequency-coupled mode is more sensitive to lower carrier densities, whereas the high frequency-coupled mode is more sensitive to changes at high carrier densities. Using micro-Raman spectroscopy,

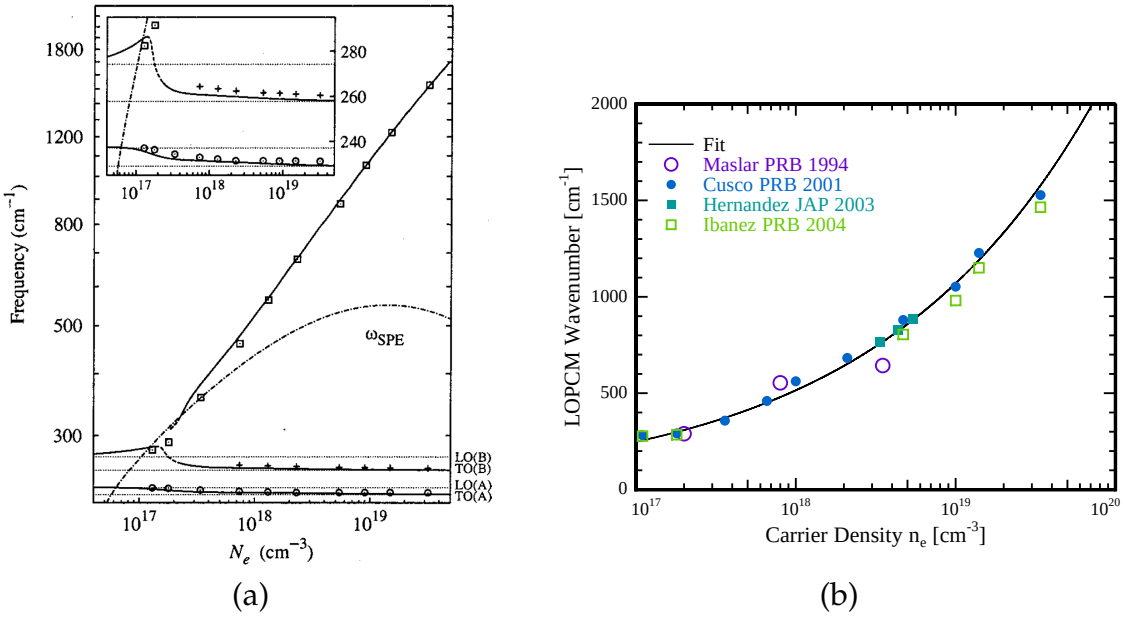

Figure 3.11: The relationship between coupled mode wavenumber and *n*-type carrier concentration for InGaAs. In (a), solid lines show the computationally derived solutions for carrier-coupled modes from Cuscó *et al.* [14] and the points are experimentally measured. Three coupled modes arise, the low (∘), intermediate (+), and high frequency (□) modes. On the right side of the plot, horizontal dotted lines mark the frequency of the primary LO and TO phonon modes: marked with an *A* for InAs-like and *B* for the GaAs-like modes. The dashed dotted line shows the frequency of single particle excitations. Reproduced with permission from Cuscó *et al.* [14], copyright Physical Review B 2001. In (b), the power law fit that was used to convert the high frequency peak position to carrier concentration in this thesis is shown as a line, based on modeling from [14]. The points are taken from the literature (∘ [15], • [14], ■ [16], and □ [17]). Note that the wavenumber on the *y*-axis is no longer plotted on a log scale.

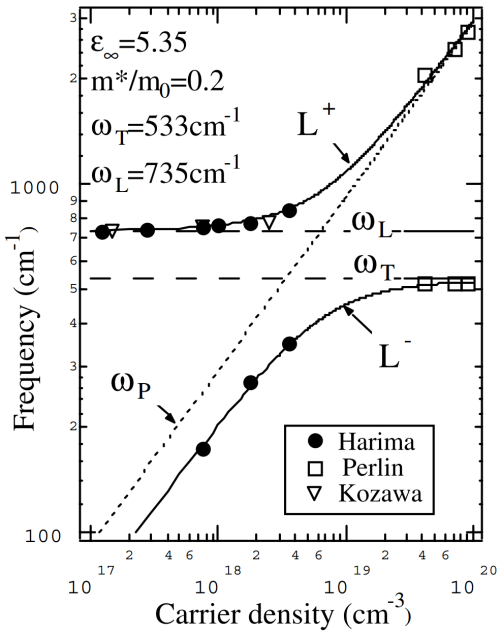

Figure 3.12: The relationship between LOPCM wavenumber and carrier concentration for *n*-type GaN [18], summarized from various previous studies (• [19], □ [20], and ▽ [21]). The dotted line marks the plasma frequency (ω_p); the frequency of the LO mode (ω_L) and TO mode (ω_T) are marked with dashed lines. The low frequency-coupled mode (L^-) and high frequency-coupled mode (L^+) are shown as solid curves. Reproduced with permissions from Harima [18], copyright Journal of Physics: Condensed Matter 2002.

we can non-destructively probe the *n*-type carrier concentration in compound semiconductors with good spatial resolution.

3.3 Summary

Laser annealing is an effective way to quickly heat and quench samples to study kinetically limited states. By combining lateral gradient laser annealing with characterization techniques with good spatial resolution, we can determine how

annealing time and temperature changes properties of compound semiconductors. Non-destructive optical techniques like Raman that probe electrical and structural characteristics are especially powerful.

CHAPTER 4

INTRINSIC InGaAs

4.1 Motivation

The undoped (denoted as "intrinsic") InGaAs samples were used to understand the baseline CO_2 and diode laser annealing behavior with laser annealing temperature profiles, the damage behavior, and the Raman spectra. This work provides the critical foundation to compare to the later studies on doped samples.

4.2 Sample Details

Samples of 300 nm of intrinsic $In_{0.53}Ga_{0.47}As$ were epitaxially grown on an InAlAs buffer layer on lattice-matched, 2-inch diameter InP substrates (with samples provided by IBM, and substrates from AXT, Inc). The samples were grown on two different types of substrates, either semi-insulating or heavily doped InP, as seen in Figure 4.1.

The heavily doped InP was *p*-type doped with Zn, grown with carrier concentrations within the range of 0.8 to 8×10^{18} cm^{-3} and mobility in the range of 50 to 100 cm^2/Vs. The samples were then cleaved into small pieces, 6 mm by 6 mm.

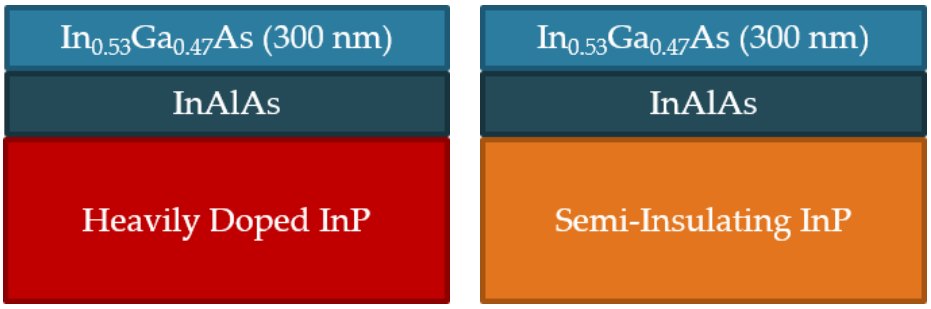

Figure 4.1: Cross-sectional schematic diagram representing the heterostructure of the intrinsic InGaAs samples: (a) InGaAs film on heavily-doped InP; (b) InGaAs film on semi-insulating InP substrate.

4.3 Laser Annealing of Intrinsic InGaAs Samples

The intrinsic samples were annealed using either the CO_2 or the diode laser. To establish upper values of the dwell that produced damage following laser annealing damage, we studied a set of single scans with steadily increasing power for each value of the dwell. This allowed us to narrow down appropriate annealing conditions (in terms of power) for each dwell and determine when laser-induced damage occurred. These served as upper limits for a given dwell/power combination.

4.3.1 CO_2 Laser Annealing

Samples of 300 nm $In_{0.53}Ga_{0.47}As$ on heavily doped InP substrates, as shown on the left hand side of Figure 4.1, were annealed with the CO_2 laser. The InGaAs is essentially transparent to the 10.6 µm laser wavelength, but the carriers in the heavily doped InP substrate couple with the laser in order to heat the In-

GaAs film indirectly. On the time scales and dimensions of these experiments, thermal conduction results in uniform heating of the InGaAs surface film. This uniformity is a result of the fact that the thermal diffusion length ($\sqrt{D\tau}$), calculated using room temperature properties of InP [121], is >100 μm even for the shortest anneals (250 μs). Dwells between 250 μs to 2 ms were explored.

4.3.2 Diode Laser Annealing

Samples on semi-insulating InP were annealed using the diode laser. The direct band gap of InGaAs (≈0.75 eV), lies above the energy of the CO_2 laser but below the energy of the diode laser, allowing us to heat the samples by direct band gap absorption. We explored dwells of 5 ms and 10 ms.

4.4 Characterization of Intrinsic InGaAs samples

4.4.1 Laser-Induced Damage

The damage behavior for the samples differed dramatically depending on the laser annealing wavelength, as described below.

CO_2 Laser-Induced Damage

Samples annealed with the CO_2 laser visibly damaged the film with evidence of a slight color change, with the sample becoming lighter where damage occurred. As the power of the laser increases, the width of the damaged region

increases, as shown in Figure 4.2, with the green box marking the center of the annealing scan, and the white text marking the power at which the laser was set (using images modified from [22] in which multiple microscope images were merged together). The line power densities ranges at which damage occurs is summarized for each dwell time in Table 4.1.

Table 4.1: Summary of visible damage of InGaAs samples annealed with the CO_2 laser. In general, the longer the annealing time, the lower the power the sample damages at.

Dwell (ms)	**Line Power Density (W/cm)**	
	No Damage	**Damage**
0.25	639	671
0.5	479	511
1	383	415
2	256	287

Crystalline slip was also evident in the damage area for some anneals. Previous work in the Thompson group had characterized this visible damage with surface damage and a decrease in arsenic composition in the sample by energy dispersive X-ray spectroscopy [22]. This result is not surprising considering the substantial evidence from other groups that high temperatures reached during the annealing can cause out-diffusion and evaporation of arsenic atoms in the InGaAs films.

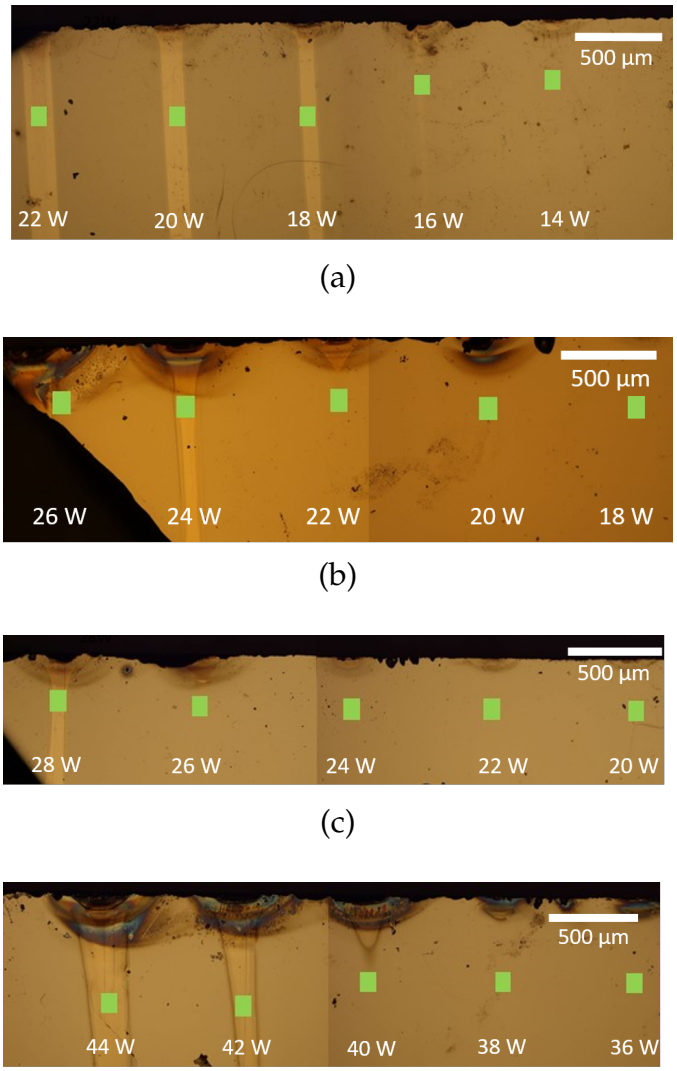

Figure 4.2: Bright field micrographs of the intrinsic InGaAs sample after annealing with the CO_2 laser with various dwell times: (a) 2 ms, (b) 1 ms, (c) 500 µs, and (d) 250 µs. Increasing the laser power increases the light colored visible damage width that occurs on the sample. This type of study, using single laser scans with increasing power, are used to identify the damage threshold of the samples. All images from [22].

Diode Laser-Induced Damage

The samples annealed with the diode laser tended to damage by slip and cracking, though the laser settings at which such damage occurred was inconsistent. About half the samples annealed tended to break at the threshold of 75 A for the 5 ms anneals and at 55 A for the 10 ms anneals. The samples also showed other visible signs of annealing, with the sample darkening in the areas that reached the highest temperatures.

Figure 4.3 shows a bright field micrograph of a sample after diode annealing at 75 A for 5 ms. The sample was coated with polymer before annealing. The laser was scanned from the top to the bottom of the sample. The darker outer edge of the sample was covered in polymer, the lighter region was where the sample reached temperatures high enough to thermally decompose the polymer, and the darker inner region is where the sample visibly damaged. The widening of the damage area as the scan progressed indicated that the temperature on the sample did not reach steady-state, with the sample increasing in temperature as the laser was scanned. The sharp color change near the bottom sixth of the figure is due to the presence of copper tape, which was used to reflect the laser light and thereby prevent thermal stress building up on the edge of the sample which could lead to cracking. The exact origin of the cracking that occurred on these samples is currently unknown. It most likely is a result of the thermal build-up of the much larger heating area of the diode laser combined with the small samples and lower thermal conductivity of the semi-insulating InP substrates, the longer dwell time, or localized thermal stress from InGaAs absorption.

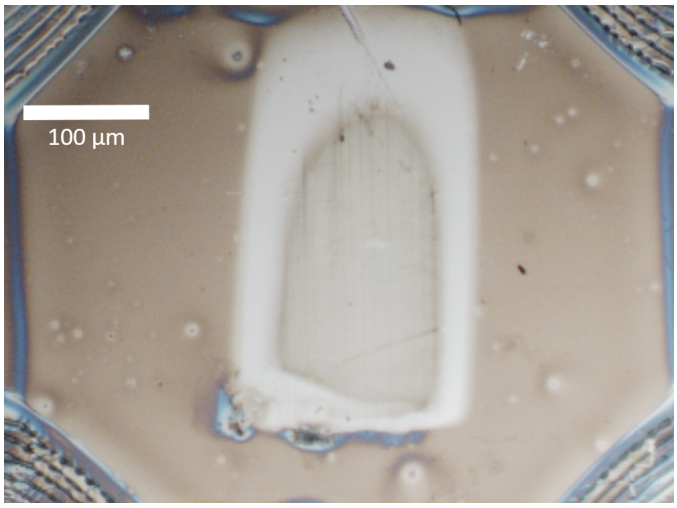

Figure 4.3: Micrograph of the intrinsic InGaAs sample coated with polymer after annealing with the diode laser for 5 ms at 75 A. The laser was scanned from top to bottom. The inner dark area is where the sample had a visible color change after annealing, slip lines are evident in this area. The surrounding white area is where the sample reached high enough temperatures to thermally decompose the polymer.

4.4.2 Temperature Calibrations

Temperature calibrations were conducted *in situ* using the thin film platinum resistors, as discussed in the Methods Section. Resistors were fabricated on both the heavily doped and semi-insulating InP samples. The resistivity of the resistor was measured as the laser passed over the sample. For each dwell, a maximum resistance was measured in the center of the laser beam, in the area corresponding to the highest power density. This measurement was used to generate the peak resistance versus power density for each dwell. The resistor was also translated laterally to develop a profile of the resistance versus position.

Gold dots were fabricated on the sample as a means to provide an absolute

temperature measurement. In addition, polymer decomposition was used as a secondary temperature calibration. These two methods were used to verify a temperature at a given position on the sample, which allowed a conversion from the resistor-measured resistance to a corresponding temperature.

CO_2 Temperature Calibrations

Gold dots were fabricated on the InGaAs samples as described in the Methods section. The laser was then scanned over the sample. The effect on the sample following laser annealing is shown as a bright field micrograph in Figure 4.4. The thin horizontal lines consist of gold dots; the lines are spaced 100 µm apart and the gold dots are spaced 10 µm apart. The sample was annealed top to bottom, with laser scans running perpendicular to the gold dots. From left to right, the scans correspond to dwell/power combinations of: 250 µs, 721 W/cm; 250 µs, 702 W/cm; 500 µs, 462 W/cm; 1 ms, 388 W/cm; and 2 ms, 296 W/cm. The image shows that, on the leading edge of the laser scan, the sample is not at steady-state; thus the width of the gold melt was taken at the bottom of the sample by which point the temperature could be relied upon to have reached steady-state. All the scans show a slight color change indicating where the laser had passed over the sample. The first two scans show clear visible damage on the sample.

Figure 4.5 shows a magnified view of the top left section of the second laser scan in a dark field micrograph. Laser-induced damage is clearly evident on the right side of the image. The gold dots are shown running horizontally across the image. The laser annealing temperature increases as it moves from the left side of the sample to the right side of the sample. On the far left of the image, the

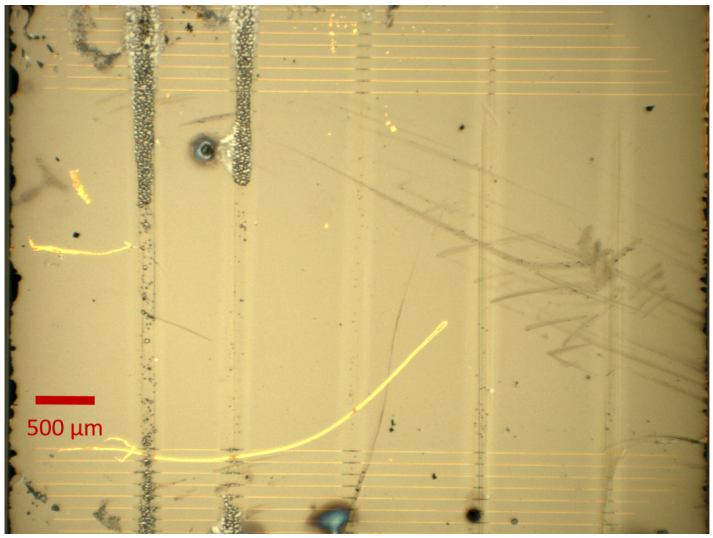

Figure 4.4: Bright field image of the InGaAs sample with gold dots used for absolute temperature calibration, shown after annealing with the CO_2 laser. The laser settings for each scan from left to right are: 250 µs, 721 W/cm; 250 µs, 702 W/cm; 500 µs, 462 W/cm; 1 ms, 388 W/cm; and 2 ms, 296 W/cm. The top and bottom of the sample show horizontal lines of gold dots. The laser was scanned perpendicular to the lines of gold dots. The melted dots appear dark, marking the areas on the sample where the sample has exceeded the melting temperature of gold. Significant laser damage is also apparent for the two left-most scans.

gold dot is unmelted, as evidenced by the faint, circular outline of the dot on the sample. At higher temperatures, the gold dot melts and beads up into smaller, glowing pieces (see Figure 3.7 for a descriptive schematic and Figure 3.8 for an image of the 1 ms, 388 W/cm scan). The "gold melt" threshold was identified as occurring in the fifth dot from the left. It appears that damage to the sample takes place slightly before the gold dots melt, visible in the changes occur on the sample in the area where the gold dots are located while the clear outline of dots shows that the gold has not melted. This additional change also seems to indicate that the gold dots are inducing visible damage in the sample farther

from the laser scan than it appears in the area without gold dots, with visible sample damage appearing to nucleate from the area where the dots are located. Since these InGaAs samples sit on InP substrates, the visible damage that occurs at a lower temperature than that corresponding to the gold melt (1064 °C) is most likely an InP melt, which occurs at 1062 °C. Since the source of this visible damage was not confirmed, and the width that this damage occurred at was inconsistent, the width of the visible damage on the sample was not used as an absolute temperature calibration.

Table 4.2 summarizes the gold melt widths found from for the different laser annealing conditions. The entries each correspond to an individual scan at a given dwell time and line power density, moving from left to right across the sample. The result for the scan corresponding to a 2 ms dwell was inconclusive; gold melt did appear, but it is possible that it was induced by the laser scattering from a scratch on the sample.

Table 4.2: Summary of steady-state, laser annealing temperature calibrations on InGaAs using gold melt. The width of the gold melt was found as a function of the laser line power density and dwell time.

Dwell [ms]	**Line Power Density [W/cm]**	**Au Melt Width [μm]**
0.25	721	150
0.25	702	140
0.5	462	60
1	388	90
2	296	< 10

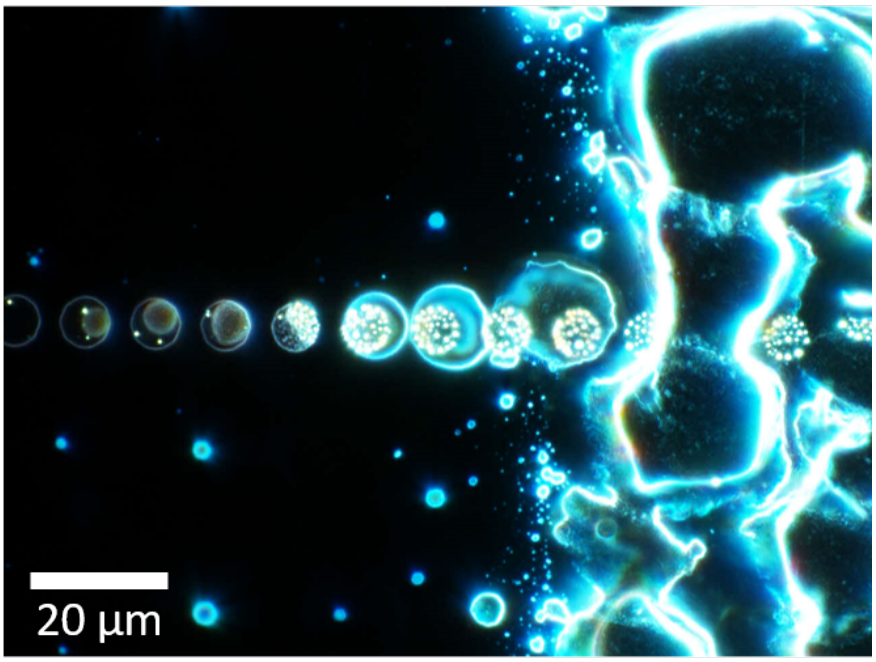

Figure 4.5: Dark field micrograph of the InGaAs sample after gold dot deposition and following annealing with the CO_2 laser used for an absolute temperature calibration. The image is of the top portion of the 250 µs scan at 702 W/cm. The laser annealing temperature increases from left to right on the image, with laser induced sample damage shown on the right. The temperature transition from gold melt is shown by the horizontal dots which melt into smaller glowing dots when the surface temperature on the sample exceeds 1064 °C.

An analogous polymer decomposition study was also carried out on the InGaAs samples. The polymer characterized in the Methods section was spun onto the sample and laser-annealed for three different conditions: 250 µs at 739 W/cm, 1 ms at 425 W/cm, and 2 ms at 314 W/cm. The samples were characterized using bright field microscope images analyzed using ImageJ intensity plots (the same analysis was also performed on the silicon calibration samples). The damage that occurred on the sample made it difficult to characterize with both profilometry and dark field images. Figure 4.6 shows the microscope images of the sample after annealing, taken in the same spot with both bright and dark field. The 250 µs and 1 ms scans show both visible damage and complete polymer decomposition. The 2 ms scan shows partial polymer decomposition and no visible sample damage. Table 4.3 summarizes the polymer decomposition widths found from the laser-annealed samples as a function of power density and dwell times.

Table 4.3: Summary of the inner and outer widths of the polymer decomposition temperature calibration found using a combination of bright field microscope analysis using ImageJ and profilometry on InGaAs samples annealed with the CO_2 laser at different combinations of power density and dwell time.

Dwell [ms]	**Line Power Density [W/cm]**	**Outer Width [µm]**	**Inner Width [µm]**
0.25	739	440	330
1	425	480	320
2	314	370	NA

The spatial profile generated from the InGaAs resistor, combined with the occurrence of the gold melt (Table 4.2) and polymer decomposition (Table 4.3),

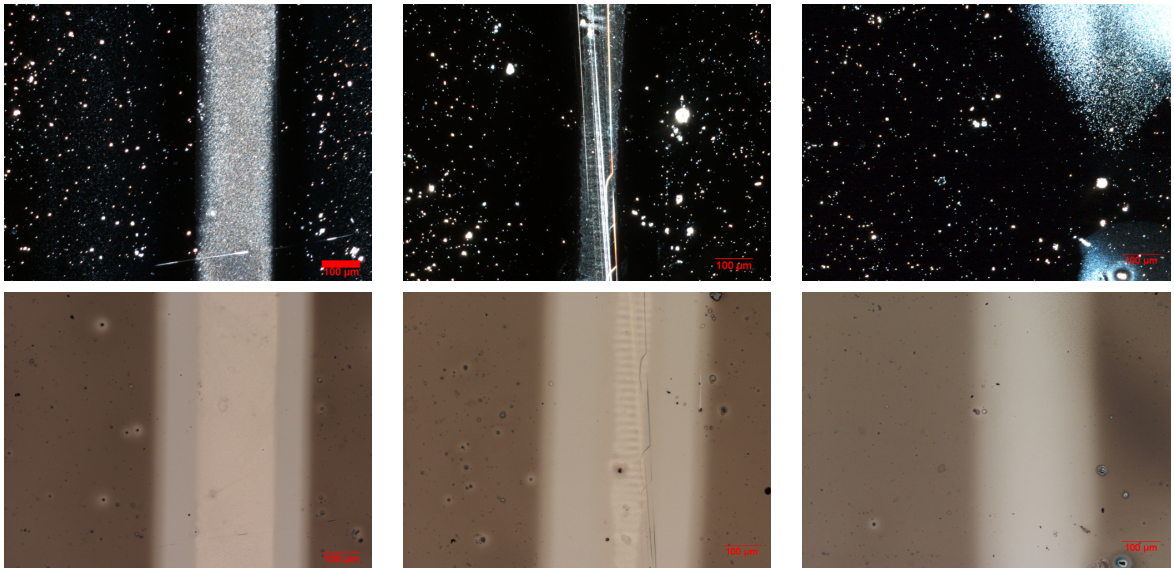

(a) (b) (c)

Figure 4.6: Microscope images showing polymer decomposition following the laser annealing of InGaAs at three different combinations of power density and dwell time: (a) 250 µs at 739 W/cm, (b) 1 ms at 425 W/cm, and (c) 2 ms at 314 W/cm. The upper image shows the dark field micrograph, the lower images shows the bright field micrograph. All samples show polymer decomposition, most easily identified in the bright field images as the transition from dark (polymer coated) to light (no polymer). The parameters used for laser annealing (a) and (b) also reached a high enough temperature to visibly damage the sample, evident as the middle stripe in both the dark and bright field images.

is shown in Figure 4.7. The peak temperature as a function of position is shown in Figure 4.8. The size of the error bars on the gold melt and polymer decomposition were based on the distance from the center of the sample at which the temperature calibration was taken. The larger the error bar, the larger the uncertainty in the temperature at the peak power. Values for the laser power were converted to line power densities using Equation 3.1. To confirm the coupling of the CO_2 laser with the heavily doped InP substrate, a patterned

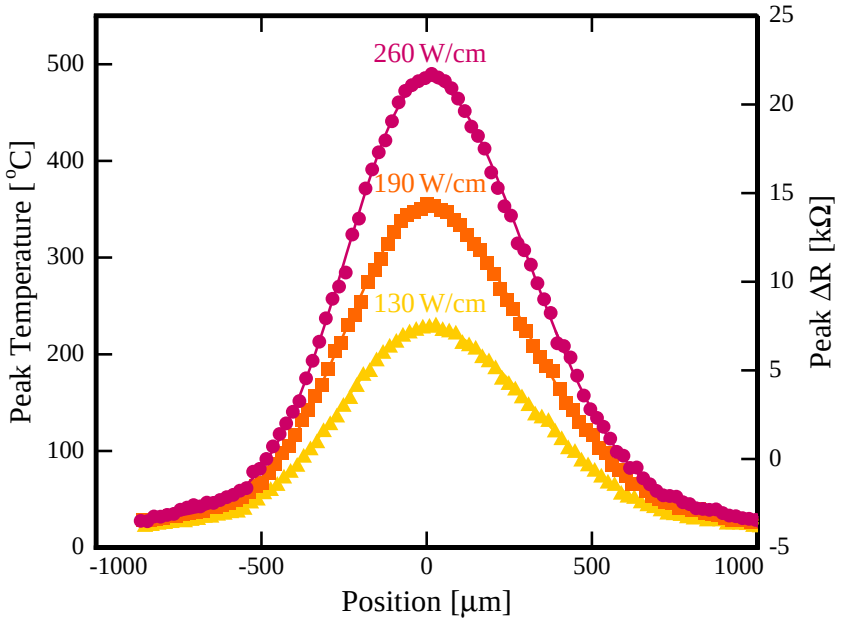

Figure 4.7: Spatial temperature profile perpendicular to the laser scan generated from resistor data for a representative InGaAs sample using the CO_2 laser, with results shown for three different power densities. The resistances were converted to temperature using the absolute temperature calibrations.

resistor used for the diode temperature calibration (undoped InGaAs/buffer layer/semi-insulating InP) was scanned with the CO_2 laser. It exhibited no change in resistance, indicating no temperature change or coupling with the CO_2 laser without the heavily doped carriers in the substrate to couple with the laser.

InGaAs films were annealed to establish the damage limits for LSA as a function of the dwell. The threshold power for visible damage in the center of each scan was determined for dwells of 250 μs, 500 μs, 1 ms, and 2 ms, and was found to be nearly independent of dwell at ≈1070 °C. The damage is most likely InP melt, which occurs at 1062 °C.

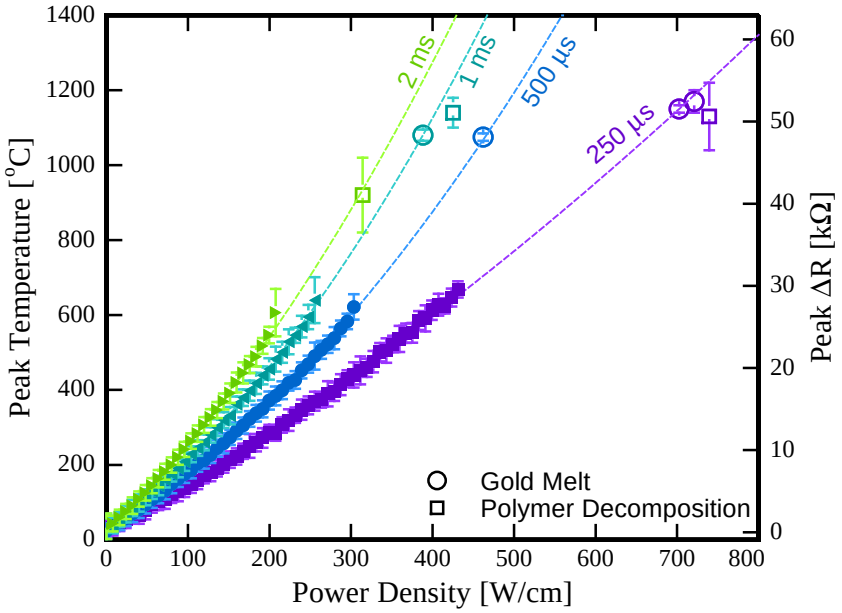

Figure 4.8: Peak temperature profile for a representative InGaAs sample using the CO_2 laser, with results shown for four different dwell times. The resistor measurements are shown as solid symbols, the absolute temperature calibration using gold melt is shown as open circles and polymer as open squares. The dotted line is based on extrapolation of the resistor data.

Diode Temperature Calibrations

Gold dots were deposited on the samples before annealing with the diode laser. A summary of the results is shown in Table 4.4. For a 5 ms dwell, the sample annealed at 75 A cracked before reaching a temperature high enough to melt the gold dots. There may have been melting along the crack, but it was difficult to ascertain with certainty. In contrast, the sample annealed at 77 A reached a temperature above the gold melt, also cracking upon annealing.

Figure 4.9 shows the 5 ms spatial temperature profile obtained from diode resistor measurements on InGaAs. The spatial profile of the 5 ms dwell was taken

Table 4.4: Summary of Au dot InGaAs samples annealed for a 5 ms dwell with the diode laser. Between the laser settings of 75 A and 77 A, the sample exceeds the gold melt temperature.

Dwell (ms)	**Laser Current (A)**	**Au Melt Width (μm)**
5	75	0
5	77	> 310

at 20 A and temperature was scaled using the polymer decomposition width. Using this technique, the peak temperature for the 75 A anneal was extrapolated to be 1060 °C, just below the gold melt. We then used Au dots to confirm this temperature calibration. The sample annealed at 75 A appeared to reach a peak temperature below the gold melt (it cracked during annealing with what appeared to be one Au dot melted along the crack). A sample annealed at 77 A was above the gold melt, with at least 31 of the Au dots melting. Half the sample annealed at 77 A shattered, making it impossible to retrieve an accurate Au melt width. This confirms that, for the two samples measured, the temperature was below 1064°C for an anneal at 75 A and above for 77 A.

The resistors did give some unexpected results. In Figure 4.10(a), we found that the resistance of the resistor changed as the HeNe pilot diode was scanned across the surface. Additionally, in Figure 4.10(b), we found that we could turn the room lights on and the resistance of the resistor would drop, perhaps indicating a poor electrical insulation from the InGaAs. Finally, the peak resistance versus laser current had an unexpected trend. Because of these anomalies, the absolute temperature calibrations were performed at the laser settings used for annealing, and extrapolations to other power densities should be undertaken

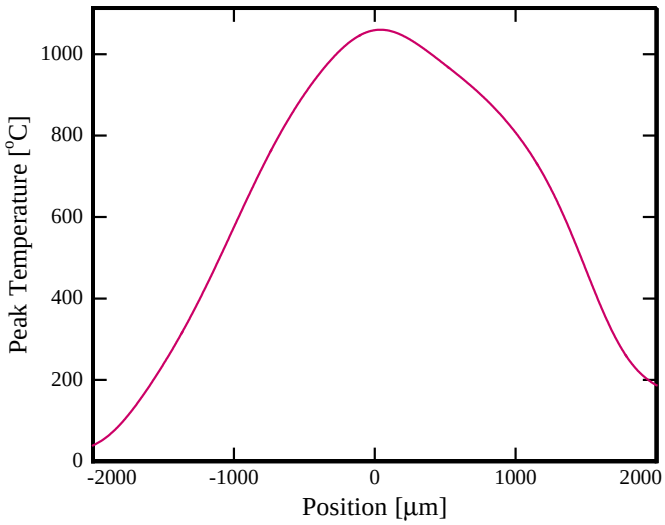

Figure 4.9: Spatial temperature profile for InGaAs using the diode laser with a 5 ms dwell. The spatial profile was collected using resistors at lower temperature and scaled to a higher temperature using the results from the absolute temperature calibrations (gold melt and polymer decomposition). Because of the broad focus of the diode laser in the *x*-axis, the spatial profile is significantly wider than the spatial temperature profile of the CO_2 laser.

with caution.

Figure 4.11 summarizes the peak resistance found from scanning the diode laser over the resistors for each dwell time. These data are shown in more detail than for the CO_2 resistors because the trends were unexpected and remain not well understood at this point. The peak resistance for each scan was found for a given value of the diode laser current and normalized to the initial resistance of the resistor before the diode laser passed over it. For scans labeled "up," the current was increased in 0.5 A increments. For data labeled "down," the current to the laser was decreased in 0.5 A increments. This was done in order to determine if the sample had cooled sufficiently between measurements. Each

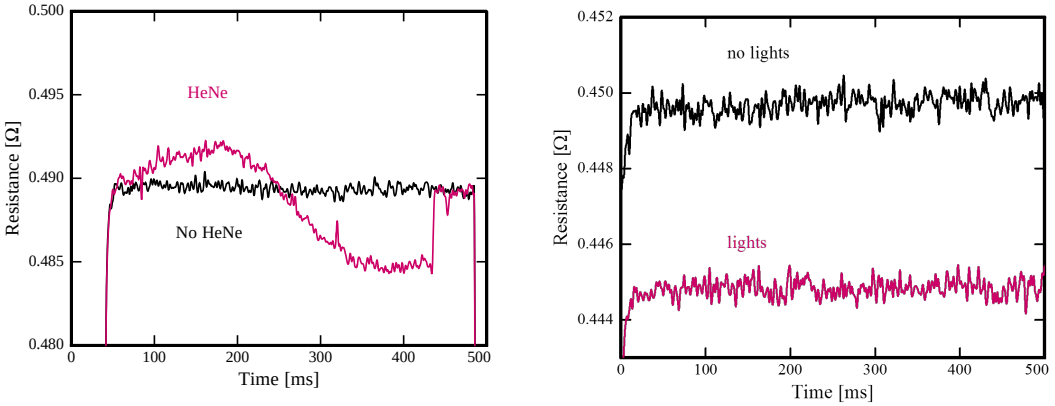

Figure 4.10: The resistor response (a) when scanned with a low power HeNe laser (a pilot diode used for aligning the samples for annealing) and (b) when the room lights were turned on and off. The resistor was not expected to behave in the manner that it did with either sample. If sample heating by light absorption was the source of the change, the resistance is expected to increase. It is currently unknown why the resistance decreases when exposed to the room lights and the resistance initially increases then decreases as the HeNe laser is scanned over the sample.

dwell was measured by first increasing the power, then decreasing the power, and finally increasing again to check for repeatability. It was expected that, if the sample did not have enough time to cool between scans, the increase in temperature on the sample would lead to a higher resistance. The samples that were ramped down in power would have a higher temperature, and thus higher resistance if this was the case. Unexpectedly, for all cases, the resistors show a strong, non-linearity in resistance versus laser current until a threshold power is reached and then the expected linearity returns. Additionally, the samples that were ramped down in power had the lowest resistance each time in the non-linear region. Additionally, the non-linear region seemed to have the most variance in measured resistance at each laser current whereas the linear region

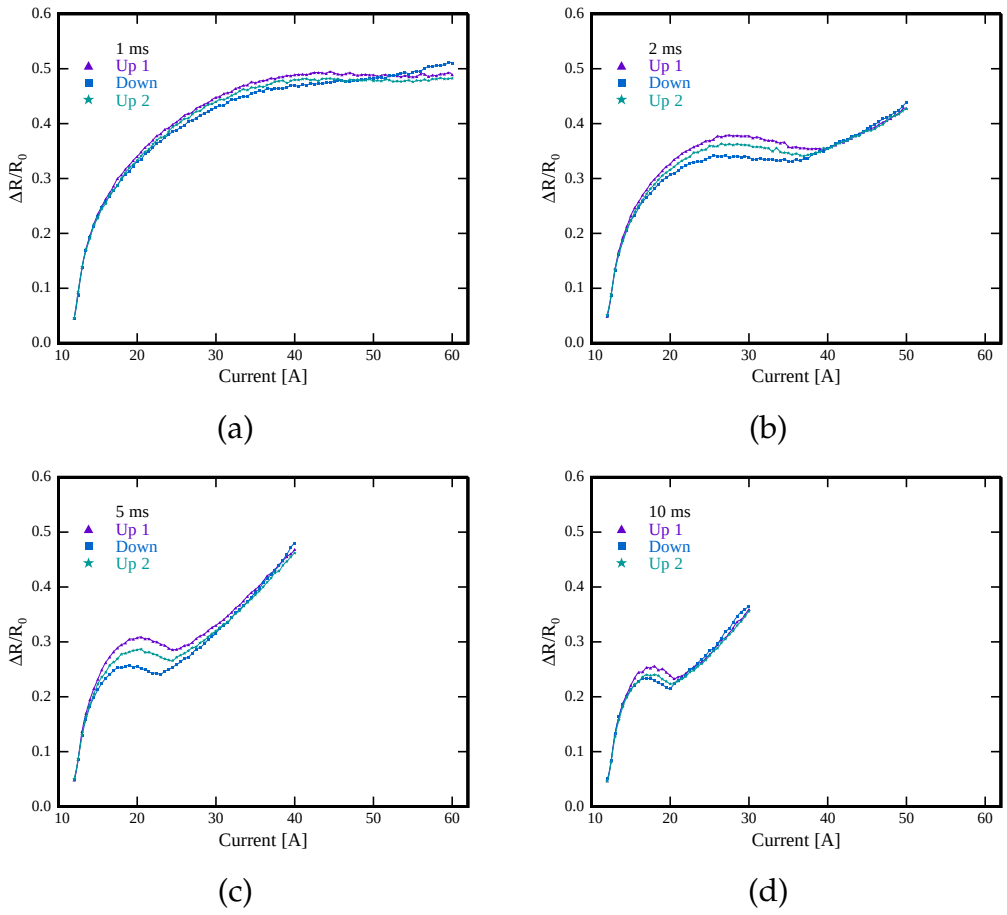

Figure 4.11: The relative temperature calibration using resistors as a function of the diode laser current. The peak resistance was found on the semi-insulating, diode laser-annealed samples at dwells of: (a) 1 ms; (b) 2 ms; (c) 5 ms; and (d) 10 ms.

is consistent. The linear region for each dwell can be extrapolated to roughly to the current which the diode laser turns on, 12 A. Using the "down" data linear region starts about at 55 A for the 1 ms dwell, 37 A for 2 ms, 23 A for 5 ms, and 20 A for the 10 ms dwell.

Directly comparing results for each dwell also leads to very unexpected results, an average for each dwell is summarized in Figure 4.12. At a given power, the shortest dwell should anneal at the lowest temperature. However, this trend

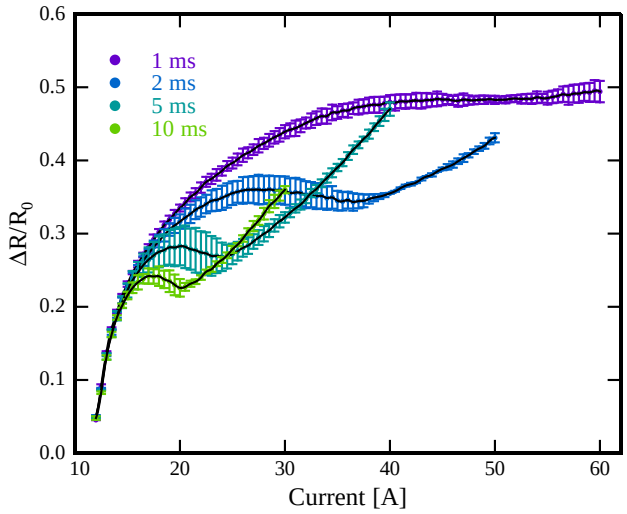

Figure 4.12: Peak resistance profile on for InGaAs using the diode laser for dwells of 1 ms, 2 ms, 5 ms, and 10 ms as a function of laser current. A linear relationship between the laser current and resistance is expected, as well as an increase in resistance at a given laser current as the dwell is increased. The reason for the observed behavior is currently unknown.

does hold for the non-linear regime for the resistors– the shortest dwell has the highest resistance, and if the resistance was solely a response to temperature change, the highest temperature. Extrapolating from the linear regime of the resistors gives the expected trend- the longer dwells reach a higher resistance than the shorter dwells at the laser current. This, combined with the resistor's response to the room lights and the HeNe laser, is good evidence that the non-linear behavior may not be a temperature driven effect. Because of this, the data collected from the resistor was not converted to temperature as it was for the CO_2 laser.

The majority of anneals in subsequent annealing studies of InGaAs on InP with the diode laser were conducted using 75 A with a 5 ms dwell. Conver-

sions from temperature to position were made based on the diode spatial profile Figure 4.9. Based on polymer decomposition, gold melt studies, and the sample damage behavior- the peak temperature of the anneals when cracking damage occurs is assumed to be around the temperature of InP melt at 1062 °C (Table 3.4).

4.4.3 Optical Characterization: Raman Spectroscopy

Micro-Raman characterization with high spatial resolution was used to probe the changes in the sample after annealing with the CO_2 laser. Raman spectra were collected in 5 µm increments perpendicular to the laser annealing stripe.

Using the temperature calibrations developed in the previous section, the positions on the sample were then converted to a corresponding temperature. To limit the amount of error introduced from uncertainty in these temperature conversions, the temperature is defined relative to the thermal damage threshold, T_D. This damage threshold corresponds to position where the visible damage identified in the microscope images occurs, and is accompanied by a sudden change in the Raman signal, which will be discussed next.

Figure 4.13 shows Raman spectra, highlighting changes in the primary phonon peaks as a function of annealing temperature, with the gray lines marking the primary phonon peak positions (InAs-like: 225 cm^{-1} (TO), 233 cm^{-1} (LO); GaAs-like: 255 cm^{-1} (TO), 269 cm^{-1} (LO)). The spectra were taken from a sample annealed with the CO_2 laser with a 1 ms dwell at 24 W. It is evident from this plot that the Raman spectra changes drastically once damaged. At the onset of visible damage, we observe a sharp decline in the GaAs-like LO mode intensity,

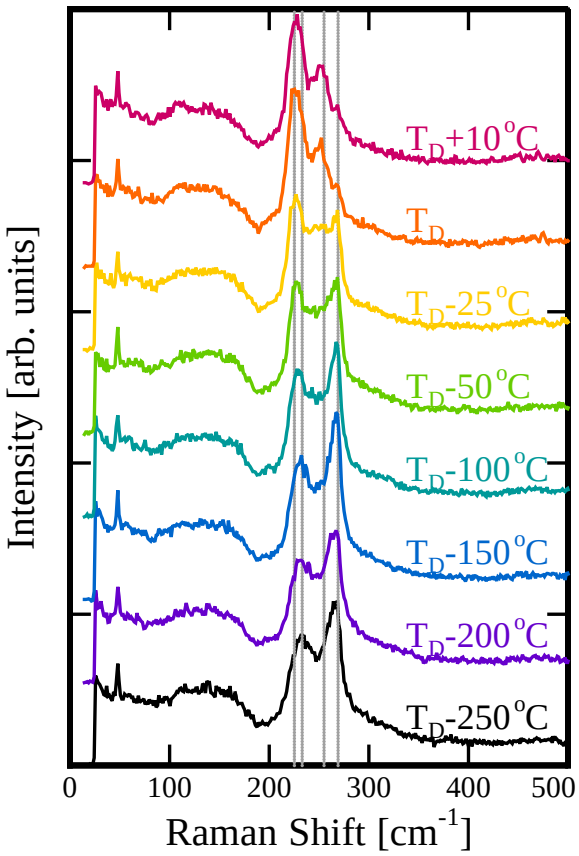

Figure 4.13: Waterfall plot of Raman spectra of the primary phonon peaks in intrinsic InGaAs as a function of annealing temperature for a sample laser-annealed at 24 W with a 1 ms dwell. The gray lines marking the primary phonon peak positions (InAs-like: 225 cm^{-1} (TO), 233 cm^{-1} (LO); GaAs-like: 255 cm^{-1} (TO), 269 cm^{-1} (LO)). Above the thermal damage temperature, T_D, the Raman spectra exhibit a sharp change, most dramatically apparent in the decrease in the intensity of the GaAs-like LO phonon (the peak marked at the highest wavenumber).

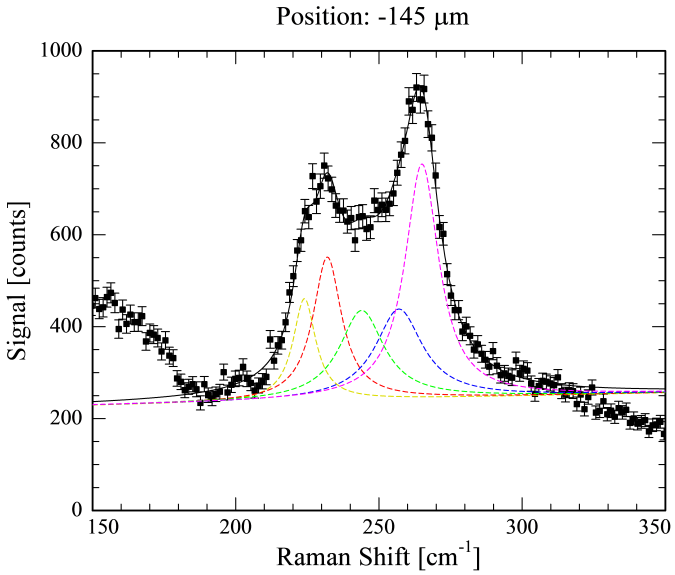

Figure 4.14: Example of the Genplot fitting of the primary peaks in the Raman spectra. The fitting is important to deconvolute the overlapping peaks. The Raman spectra were fit using the primary phonon peak positions (InAs-like: 225 cm^{-1} (TO), 233 cm^{-1} (LO); GaAs-like: 255 cm^{-1} (TO), 269 cm^{-1} (LO)) and a disorder-induced mode at 244 cm^{-1}. The fitting script was used for each collected Raman spectrum to analyze changes in material with annealing. The peak positions, widths, and intensity were allowed to vary during fitting.

with a corresponding appearance of Raman InAs-like and GaAs-like transverse optical (TO) modes.

The temperature at which the intensity of the GaAs-like LO phonon peak drops abruptly is defined as the thermal damage temperature (T_D). For all dwells, our best estimate of this temperature is ≈1070±50 °C, near the expected $In_{0.53s}Ga_{0.47}As$ and InP melting points.

This signal change correlated well with the visible damage on the sample and with As loss. To quantitatively assess the change in behavior of the spectra, the phonon peaks were fitted between 180 cm^{-1} and 310 cm^{-1} using a set

of five Lorentzian peaks: GaAs-like and InAs-like peaks as well as an disorder-induced mode at 244 cm^{-1} [107]. An example of the fitting is shown in Figure 4.14. The results of the fitting is shown for the GaAs-like LO phonon mode in Figure 4.15. The GaAs-like phonon mode shifts in position 125 °C before damaging. Once the sample approaches the damage threshold, the area of the GaAs-like LO phonon peak drops. Changes in primary peaks can indicate changes in alloy composition, orientation, crystalline quality, and stress [122]. A decrease in intensity corresponds to a decrease in crystalline quality, and a shift of the peak position corresponds to a change in composition or stress. The behavior in Figure 4.15 shows that little change is apparent in the GaAs-like LO phonon in Raman until ≈125 °C before damaging. After this point, the GaAs-like LO phonon shifts in position and decreases in intensity. This shows that even before the visible damage, the crystalline quality of the sample changes during annealing. The change is gradual, and is most likely from arsenic evaporation at high temperature.

4.5 Summary

InGaAs films were annealed using IR lasers on both the heavily *p*-type doped and semi-insulating InP substrates. The difference in absorption mechanism (film versus substrate) combined with the different laser annealing profiles, and dwell times led, ultimately, to different types of sample damage. Samples that were diode laser-annealed ultimately reached lower temperatures during the anneals and were less consistent in their failure behavior. Arsenic evaporation from the films was apparent even for the shortest dwell times explored here. Raman spectroscopy was used to probe changes in the sample as a result of

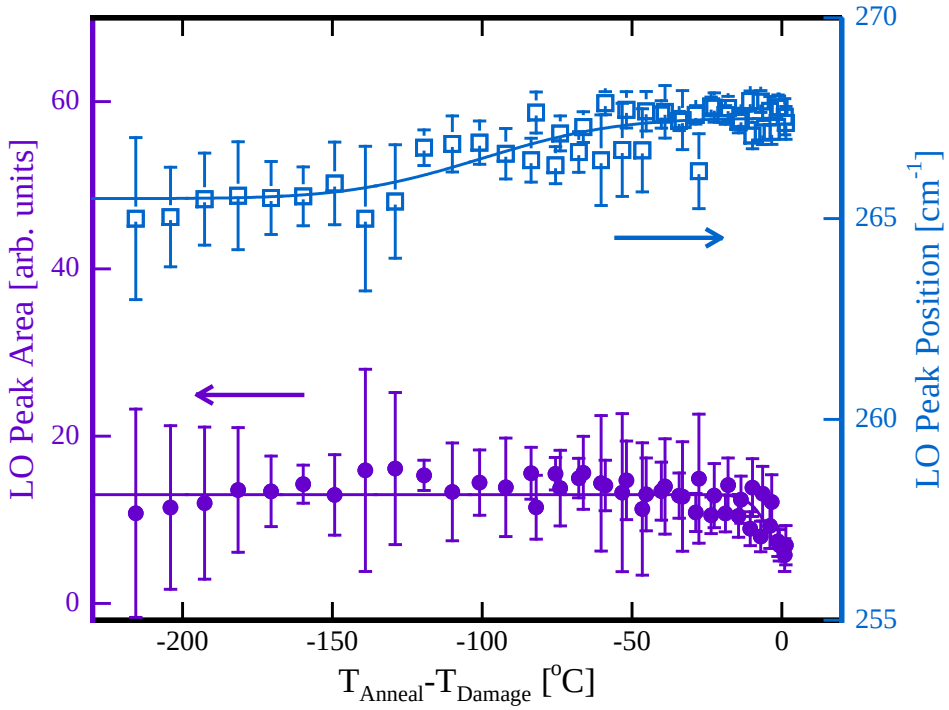

Figure 4.15: Plot of the Raman GaAs-like LO phonon peak position and area as a function of annealing temperature (up to sample damage). Raman spectra were collected after annealing with the CO_2 laser for 1 ms at 24 W. As annealing temperature increases, the GaA-like LO phonon peak area decreases and the peak position increases, indicating a change in crystalline lattice.

laser annealing, with the GaAs-like phonon mode disappearing when the sample surpassed the damage threshold.

CHAPTER 5

ION-IMPLANTED InGaAs

5.1 Motivation

Ion-implantation is a traditional and cost-effective way of incorporating dopants into semiconductors with good spatial resolution. As a result of implantation, the dopants need to be annealed to repair the damage made to the initially crystalline material and move the dopants into active lattice sites. In this study, ion-implanted InGaAs samples were laser-annealed with either the CO_2 or the diode laser to evaluate the feasibility of activating dopants using short-timescale, high temperature laser anneals and to establish limits in both dopant activation and damage created in the samples.

5.2 Sample Details

5.2.1 InGaAs Low Dose Implant Samples

Samples with 300 nm thin films of $In_{0.53}Ga_{0.47}As$ were epitaxially grown on a InAlAs buffer layer, on either semi-insulating or heavily doped, lattice-matched, InP substrates (samples provided by IBM, substrates from AXT, Inc.). Samples were doped with Si by ion-implantation at room temperature at 20 keV to a dose of 10^{14} cm^{-2}, and were cleaved into small 6 mm by 6 mm pieces for annealing. Cross-sectional sketches of the samples are shown in Figure 5.1. SRIM (Stopping and Range of Ions in Matter) [123] calculations were used to give an estimated

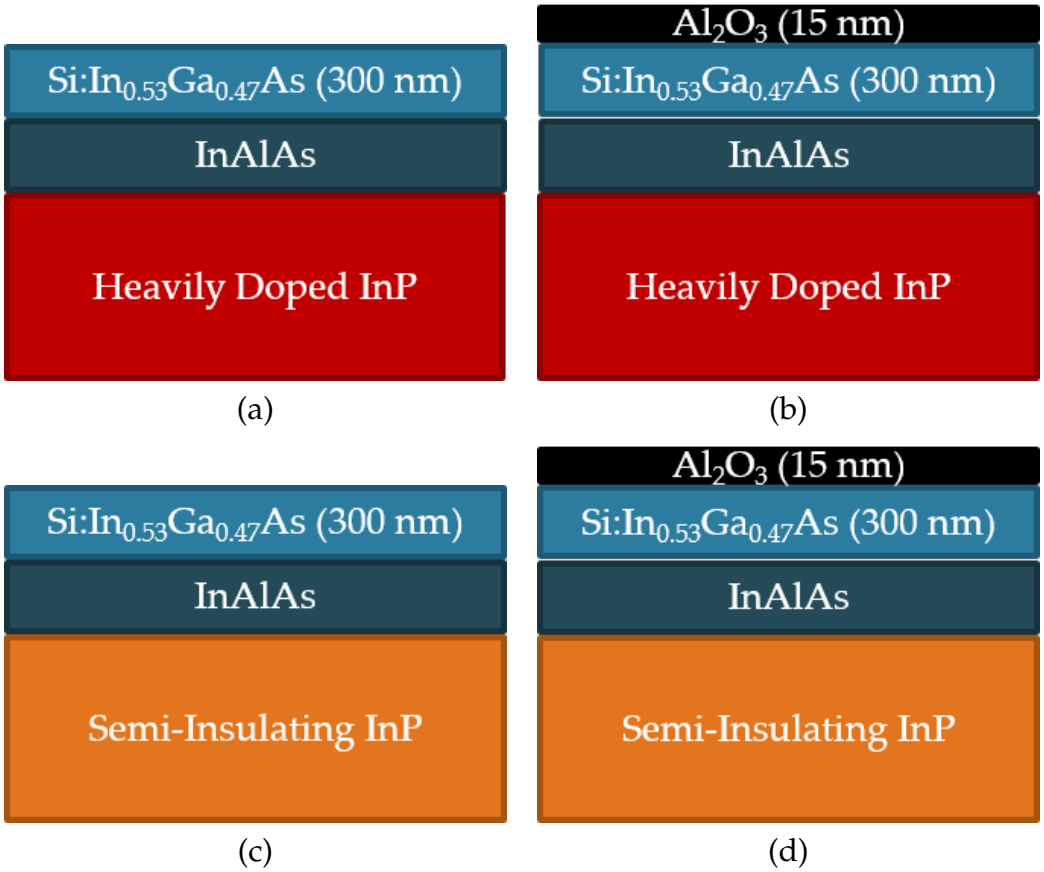

Figure 5.1: Schematic cross-sectional diagrams of the InGaAs samples from IBM that were ion-implanted with silicon. Samples annealed with the CO_2 laser feature heavily doped InP substrates whether (a) uncapped or (b) capped configurations. Samples on semi-insulated InP substrates were annealed with the diode laser, (c) uncapped and (d) capped with an Al_2O_3 layer.

range of 25 nm for the Si with a peak concentration of 2.5×10^{19} cm^{-3}. To prevent arsenic evaporation at high annealing temperatures, some of the implant-doped samples were capped with 15 nm of Al_2O_3 deposited by atomic layer deposition at the University of Florida (courtesy of Kevin Jones), as shown in Figure 5.1b.

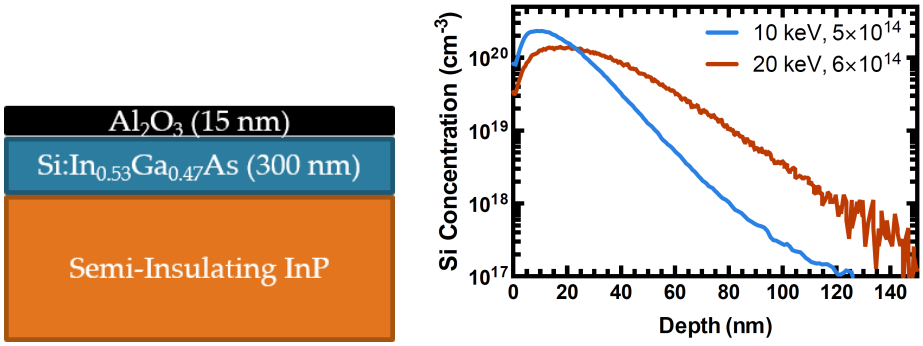

Figure 5.2: Representations of the InGaAs samples from the University of Florida that were ion-implanted with silicon: (a) schematic cross-section of the sample, (b) SIMS implant profile (10 keV) of silicon concentration as a function of depth, provided by our University of Florida collaborator [23]. Samples were annealed with the diode laser.

5.2.2 InGaAs High Dose Implant Samples

Samples with 300 nm epitaxially grown $In_{0.53}Ga_{0.47}As$ on lattice-matched InP substrates. Samples were obtained in collaboration with Kevin Jones's group at the University of Florida (UF). Samples were implanted with a dose of 5×10^{14} cm^{-2} at 10 keV at 80 °C to avoid amorphization. A sketch of a typical sample's cross-section is shown in Figure 5.2a.

Some of the samples were subjected to an additional rapid thermal annealing (RTA) step and their electrical properties were then measured by our collaborators at University of Florida. A summary of the samples is shown in Table 5.1.

Table 5.1: Summary of the ion-implanted InGaAs samples provided by University of Florida.

Sample ID	RTA Step	Mobility	Sheet Number	Sheet Resistivity
UF-A	none	N/A	N/A	N/A
UF-B	750 °C spike	4044	2.49×10^{12}	619
UF-C	750 °C 5 s fast ramp	1788	1.86×10^{13}	187

5.3 Annealing Methods

5.3.1 Furnace Annealing

For furnace anneals, samples were added into a load-locked, pre-heated furnace at room temperature, outside the heated zone. The furnace was purged with nitrogen gas for 10 minutes. The samples were then moved into the heated zone in ≈15 seconds. Once the samples were moved into the heated zone, they were annealed for 15 minutes. After annealing, the samples were moved rapidly back to load-lock and allowed to cool for 5 minutes before opening up the load-lock and exposing the samples to ambient air.

5.3.2 Laser Annealing

The coupling mechanism for laser-induced annealing is assumed to be the same as the intrinsic InGaAs samples. As with the intrinsic InGaAs samples on heavily doped InP, the ion-implanted samples were annealed with the CO_2 laser.

The CO_2 laser heats the sample by coupling with the free carriers in the heavily-doped InP substrate. Samples on semi-insulating substrates were annealed with the diode laser which heats the sample by coupling with the direct band gap on InGaAs.

5.4 Characterization of Low Dose Implant Samples

5.4.1 Laser Annealing Temperature and Material Damage

Since the coupling mechanism in doped InGaAs is the same as that for the intrinsic InGaAs samples, the annealing temperature that was found using the intrinsic samples was applied to these samples. This assumes that the doping did not significantly alter the coupling behavior between the laser and the samples.

The doped InGaAs samples on p-type InP annealed with the CO_2 laser were found to incur damage at $\approx 10\%$ lower power densities than the undoped samples. This could be a result of the activated carriers in the InGaAs coupling to the CO_2 laser, leading to an increase in absorption. This behavior is evidenced by the wider damage width that occurs after annealing with the CO_2 laser at same power and dwell compared to intrinsic samples. Additionally, sometimes crystalline slip accompanied the visible damage that occurred on the sample.

Figure 5.3 shows a dark field micrograph of an uncapped, Si-doped InGaAs sample annealed just above the damage threshold (in this case, 1 ms, 388 W/cm). The damage is visible as a periodic pattern that is apparent in both

bright and dark field imaging, with oscillations on the order of the wavelength of the CO_2 laser (≈11 μm). Similar patterns have been observed for laser irradiation of Si and GaAs as mentioned in the Methods Chapter and have been identified as laser-induced periodic surface structures (LIPSS) stemming from a laser-induced instability. It is suggested that these patterns are triggered by a surface scattering event that is then imprinted on the material by melt, deformation, and re-solidification [124, 92, 72, 95]. As the damage threshold is an easily established reference condition, temperatures in the subsequent discussion are expressed relative to this damage temperature, T_D.

5.4.2 Electrical Characterization: Micro Four-Point Probes

Sheet conductance (proportional to carrier density assuming a constant mobility) of two laser scans with a 1 ms dwell were measured using CAPRES micro four-point probes (Figure 5.4a). These data are plotted as a function of the spatial position across the Gaussian laser scan, with the highest temperature reached at x=0 and decreasing temperatures on either side (see Figure 4.7). The equivalent sheet resistance is shown on the right axis. For a scan with a peak laser power density of 350 W/cm (≈100 °C below T_D), the InGaAs reaches temperatures that activate the silicon dopants as evidenced by the monotonic increase in sheet conductance towards the center of the laser scan. Increasing the peak laser power density to 380 W/cm (T_D+10 °C), the maximum annealing temperatures exceeds the damage threshold which is manifested as a decrease in sheet conductance for positions within 50 μm of the center. Using the lateral laser temperature profile to convert from position to temperature, these same data are shown in Figure 5.4b as a function of peak annealing temper-

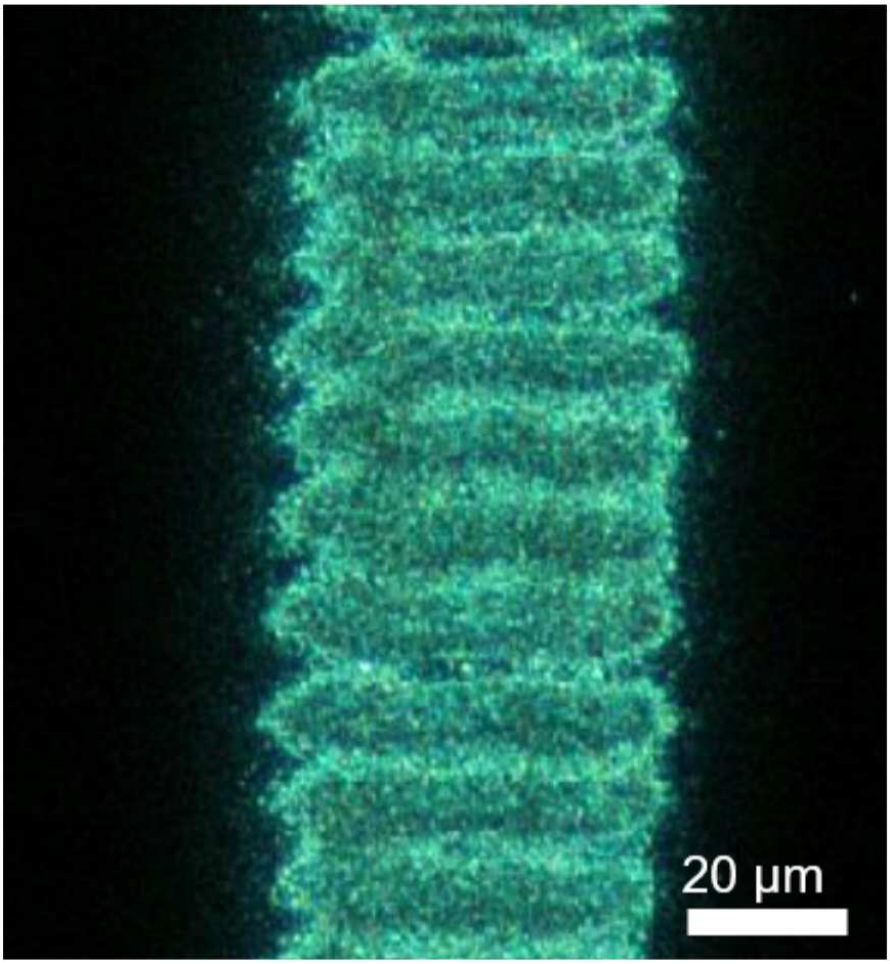

Figure 5.3: Dark field micrograph of Si-doped, InGaAs subjected to CO_2 laser annealing, showing LIPSS damage at high annealing temperatures. The sample was annealed with a 1 ms dwell at an estimated peak temperature of 1080 °C.

ature. For the 350 W/cm anneal, the entire scan remains below the damage threshold whereas, at 380 W/cm, the center exceeds the damage threshold temperature. The overlap of these data confirms the reliability of the temperature calibrations over varying samples and laser powers. The extremely rapid rise in sheet conductivity also demonstrates the power of the spatially resolved characterization which is able to follow the rapid onset of activation over a narrow 10-20 °C temperature band (975-995 °C). Indeed, the entire temperature window

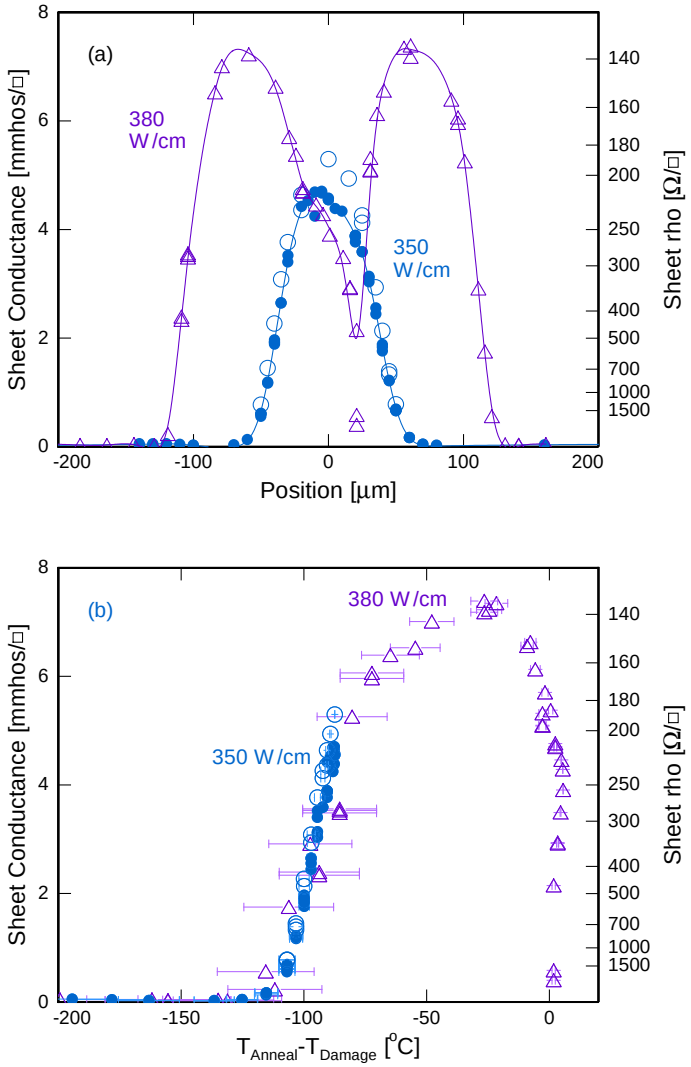

Figure 5.4: (a) Sheet conductance as a function of position for two laser stripes annealed with a 1 ms dwell at different laser powers. (b) Sheet conductance as a function of the peak annealing temperature. Uncertainty in temperature increases with increasing distance from the center of the beam.

for the activation of InGaAs is surprisingly narrow using LSA. Essentially no activation is observed 110 °C below T_D with the peak activation achieved at 30 °C below T_D.

5.4.3 Raman Characterization of Low Dose Implant Samples

Initially, the low dose, ion-implanted samples were furnace-annealed and characterized using Raman spectroscopy. This gave us a long-timescale annealing behavior from furnace annealing to compare to the short-timescale behavior from laser annealing. In Figure 5.5, a waterfall plot of the collected Raman spectra is plotted for each annealing temperature.

The primary phonon peaks in the Raman spectra are generally not visible, due to a filter cut-off in the spectrometer, with the exception of the tail-end of the GaAs-like LO phonon (the lowest wavenumber peak). The peaks between 300 and 550 cm^{-1} are secondary phonon peaks. The implant destroys the crystalline quality of the sample. Beginning at 450 °C, the implantation damage starts to repair, reflected in an observed increase in intensity and a sharpening of the secondary phonon peaks. Beginning at 500 °C, a broad peak appears around 720 cm^{-1} and increases in position as the temperature increases. This is identified as the L_+ coupled mode, discussed in the Methods section. The increase in peak position indicates that the implanted silicon dopants in the sample are becoming activated. Between 600 °C and 650 °C, the L_+ does not significantly change in position, but the primary phonons show an increase in crystalline quality. The maximum L_+ peak position occurred for the 700 °C anneal. At 750 °C, the sample showed signs of visible damage and the Raman spectra varied across the sample. Since these samples were uncapped, the damage is likely to stem from arsenic loss. The 550 °C anneal did not have a visible L_+; the reason for this is currently unknown. We can compare our results with other work; for instance, Hernandez *et al.* found that, with 10-second RTA, a temperature of 600 °C was sufficient to repair crystalline damage, but higher

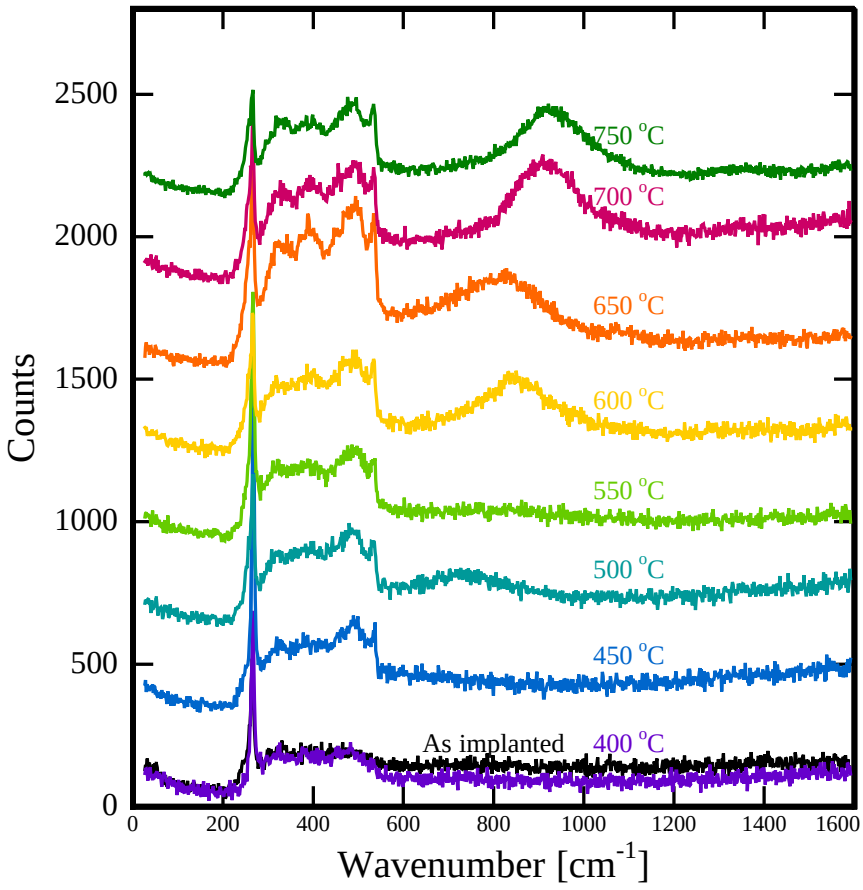

Figure 5.5: Waterfall plot of Raman spectra taken for furnace-annealed, ion-implanted InGaAs from annealing temperatures ranging from 450 to 750 °C in steps of 50 °C. Each offset scan corresponds to a different annealing temperature. The lowest wavenumber peak at ≈269 cm^{-1} is the GaAs-like phonon mode. The broad peak between 600 cm^{-1} and 1000 cm^{-1} that increases in wavenumber with an increase in temperature signifies an increase in *n*-type carrier concentration. The sample showed visible signs of surface damage at 750 °C and inhomogeneities in the Raman signal based on the position on the sample, so it was defined as the damage temperature.

temperatures, 700 °C, were needed to activate the implant [16]. It is expected that long timescales of furnace annealing relative to RTA would allow for those changes to take place at lower temperatures.

The behavior of undoped InGaAs under LSA and the furnace annealing of doped InGaAs established a framework with which we could study ion-implanted samples. For these moderate dose implants, concentration-dependent diffusion effects are not expected to occur for short timescale anneals, allowing a baseline behavior to be established under LSA. This discussion will focus on 1 ms dwells; but all other dwells exhibited similar behavior. As a function of the peak annealing temperature, the GaAs-like LO phonon peak area was used to follow recovery of implantation-induced crystal damage, while the LOPCM peak was used to estimate active carrier concentrations. Figure 5.6a shows the evolution of the LO peak area and the LOPCM peak position with annealing temperature to just above the damage threshold. At temperatures above 100 °C below T_D, there was insufficient energy to activate any significant carrier concentration. In this regime, the GaAs-like LO peak exhibited a continued rise in intensity, which we attribute to structural annealing of the implantation-induced lattice damage.

With increasing temperature, Si dopants began to activate and a statistically significant LOPCM peak was observed with an abruptly increasing intensity. Since the Raman modes are coupled, the area of the GaAs-like LO phonon peak decreased as this LOPCM peak developed. The peak position, which directly measures the carrier concentration, is also shown in Figure 5.6a (when statistically significant). Because Raman spectroscopy probes across an inhomogeneous doping profile, the LOPCM peak was found to be broad in comparison

to samples that were homogeneously doped, such as those in the next chapter. This result has been noted before for InGaAs implanted with silicon [16].

At the onset of measurable activation, the LOPCM peak occurred at ≈860 cm^{-1} corresponding to an active carrier concentration of 5×10^{18} cm^{-3}. The activation level increased with increasing temperature to a maximum that occurred ≈30 °C below T_D, with an LOPCM peak at almost 1000 cm^{-1}. This corresponds to a carrier density of 7.6×10^{18} cm^{-3}. With further increases in temperature, the LOPCM peak shifted to lower wavenumbers until reaching the damage threshold at which both the GaAs-like LO and LOPCM peaks collapse. Table 5.2 summarizes results for a variety of different dwells, in addition to a 15-minute furnace anneal in N_2. In all cases, laser-annealed samples were able to reach higher activation levels, which occurred at temperatures 300-350 °C above temperature limits for the furnace anneals. Because of the uncertainty in the measured temperatures for the LSA samples, differences in activation and damage temperatures between the different laser dwells are very likely to be negligible.

The effect of a 15 nm ALD Al_2O_3 capping layer is shown in Figure 5.6b with similar LO peak intensity and LOPCM peak position data. The LO phonon peak intensity again increased with temperature, reaching a maximum approximately 150 °C below T_D, followed by the onset of the LOPCM peak. However, in contrast to the uncapped sample, the capped sample reached its maximum LOPCM peak position just before damage occurred. Although the absolute maximum LOPCM peak positions differ, we do not believe this is significant as it falls within the standard deviation of the uncertainty in LOPCM position. The drop in the LOPCM peak for uncapped samples within 30 °C of T_D is likely to be due to the incipient loss of arsenic from the sample just below the melt,

Table 5.2: Summary of CO_2-annealed, low-dose ion-implanted samples. LSA was able to activate more *n*-type carriers and reach higher temperatures before damaging in comparison to furnace annealing.

Annealing Time	15 minutes Furnace	250 µs LSA	500 µs LSA	1 ms LSA	2 ms LSA
Onset of Activation [°C]	500	945	980	970	945
Peak Activation [°C]	700	1015	1040	1040	1020
Damage [°C]	750	1050	1075	1070	1060
Peak LOPCM [cm^{-1}]	910	965	980	1000	970
Peak Carrier Density [cm^{-3}]	5.6×10^{18}	6.0×10^{18}	7.1×10^{18}	7.6×10^{18}	6.9×10^{18}
Estimated Activation	34%	36%	41%	44%	40%

with arsenic vacancies compensated by the amphoteric silicon dopants. The deactivation behavior on the uncapped sample occurs ≈50 °C below T_D. Comparing with the Raman behavior of the uncapped intrinsic InGaAs samples in Figure 4.15, the area and position of the primary GaAs-like LO phonon also changed within ≈50 °C of damage, supporting the claim that this deactivation behavior is a related to the changes in the InGaAs film. The capping layer appears to be effective at preventing this evaporation up to the onset of the melt

and preventing deactivation from occurring.

5.4.4 Comparison of Micro Four-Point Probes and Raman Data

Electrical and Raman estimates of carrier densities should be consistent. To test this, Figure 5.7 compares the electrical sheet conductivity ($ne\mu$) with the LOPCM determined carrier density for uncapped samples. Both data sets show essentially identical trends, with the carrier concentration increasing dramatically at 100 °C below T_D before reaching a peak near 30 °C below T_D. Above this peak activation, the carrier concentration and sheet conductivity decrease slowly, presumably due to arsenic loss, until damage. The strong correlation of the carrier concentration with the sheet conductance indicates that the carrier mobility remains relatively constant over this temperature range. Based on the SRIM[123] implant profile, and assuming a flat truncated carrier concentration, we estimate the room temperature mobility of the carriers to be $\approx$1060 cm^2/Vs. This is consistent with other Hall effect measurements of Si^+ mobility in ion-implanted InGaAs [125, 126].

5.5 Characterization of High Dose Implant Samples

5.5.1 Laser Annealing Temperature and Material Damage

The diode laser was used to anneal the InGaAs samples on semi-insulating InP substrates. Since the coupling mechanism is direct band gap absorption with the InGaAs, the doping through ion-implantation was not expected to signifi-

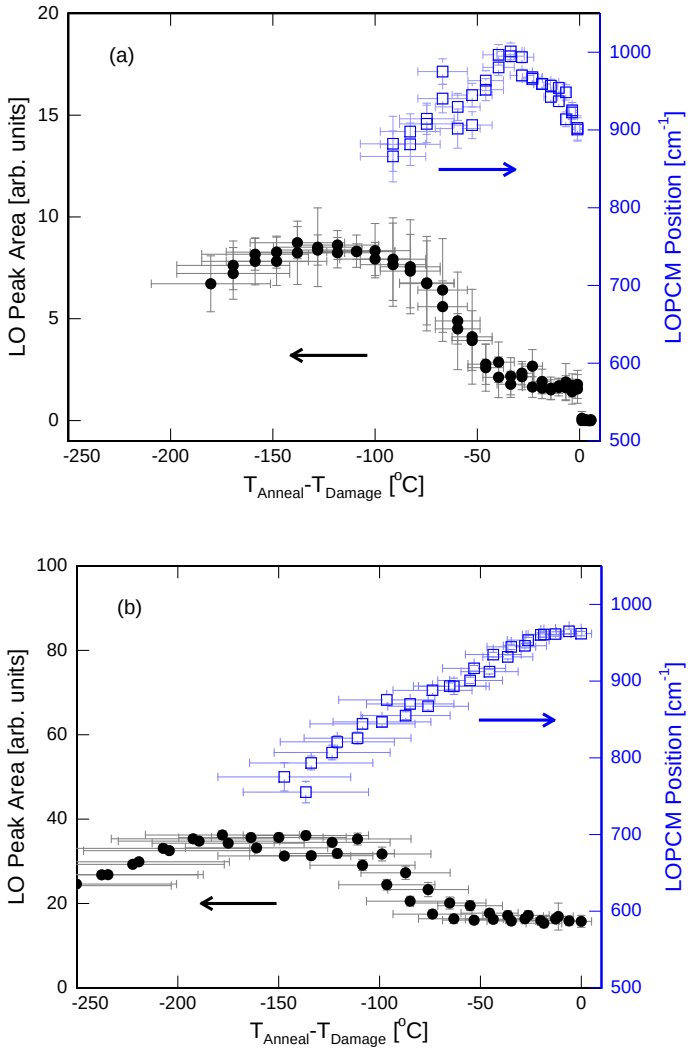

Figure 5.6: The GaAs-like LO phonon peak area and LOPCM peak position as a function of peak annealing temperature across a single laser scan for an ion-implanted sample that is (a) uncapped and (b) capped with 15 nm of Al_2O_3. LOPCM data are shown only for spectra with a statistically significant peak. At high temperatures before damaging, the uncapped sample shows a decrease the carrier concentration, whereas the capped sample does not show this same decrease. It is hypothesized that this deactivation behavior is a result of the group V vacancies that are created when the arsenic evaporates. The amophoteric silicon dopants can move into these group V sites, forming compensating defects that deactivate the *n*-type carriers in the sample.

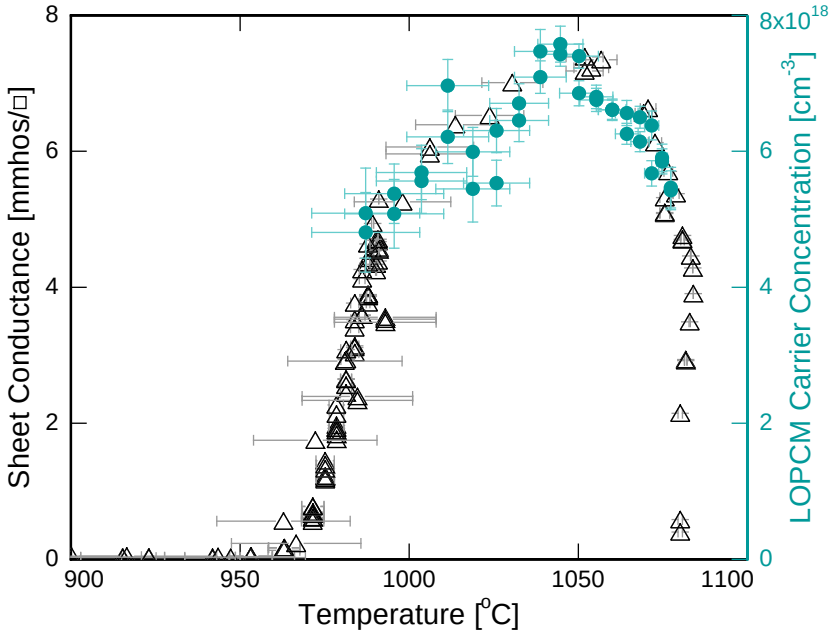

Figure 5.7: Comparison of the LOPCM peak position (carrier density) with the measured sheet conductance as a function of temperature. The trend from the traditional electrical sheet conductance measurement matches well with the trend for the carrier concentration found using Raman Spectroscopy.

cantly alter the interaction of the laser with the sample. It was assumed that the temperatures reached during laser annealing on the intrinsic samples and the ion-implanted samples are the same.

The ion-implanted samples annealed with the diode laser damaged the same way as the intrinsic samples, with crystalline slip, color change, and often cracking. Additionally, there were no apparent differences between intrinsic versus doped samples the laser settings that caused the samples to reach the damage threshold. Figure 5.8 compares the laser annealing damage behavior of the intrinsic and ion-implanted InGaAs samples from IBM without protective capping layers. Longer, 10 ms dwells, were initially explored for annealing, but the

sample cracked more frequently than with the 5 ms dwells. The damage threshold for sample cracking for 10 ms dwells was within the 49 A to 55 A range. All samples characterized in the sections below were laser-annealed with a 5 ms dwell with the laser current set at 75 A. The samples that were capped did not show the visible color change that the damaged uncapped samples did, as apparent in Figure 5.8. Based on this, is is assumed that the color change in the uncapped samples is originating from arsenic loss.

5.5.2 Raman Characterization of High Dose Implant Samples

After annealing, Raman spectra were taken across the samples and analyzed to locate the LOPCM peak position. The peak position was converted to carrier density and the position on the sample was converted to laser annealing temperature. A comparison between the samples is shown in Figure 5.9.

Samples were annealed with RTA and electrically characterized by University of Florida. Raman showed additional activation after LSA, with LSA most effective on samples with high mobility but with low carrier concentrations (RTA 750 °C, spike). The carrier density from the LOPCM peak after LSA is approximately 30% greater than the 1.4×10^{19} cm^{-3} solubility limit found previously [24]. The results are summarized in Table 5.3.

5.6 Summary

Ion-implanted samples were successfully annealed using either a CO_2 or diode laser. The carrier concentration as a function of position of the sample was mea-

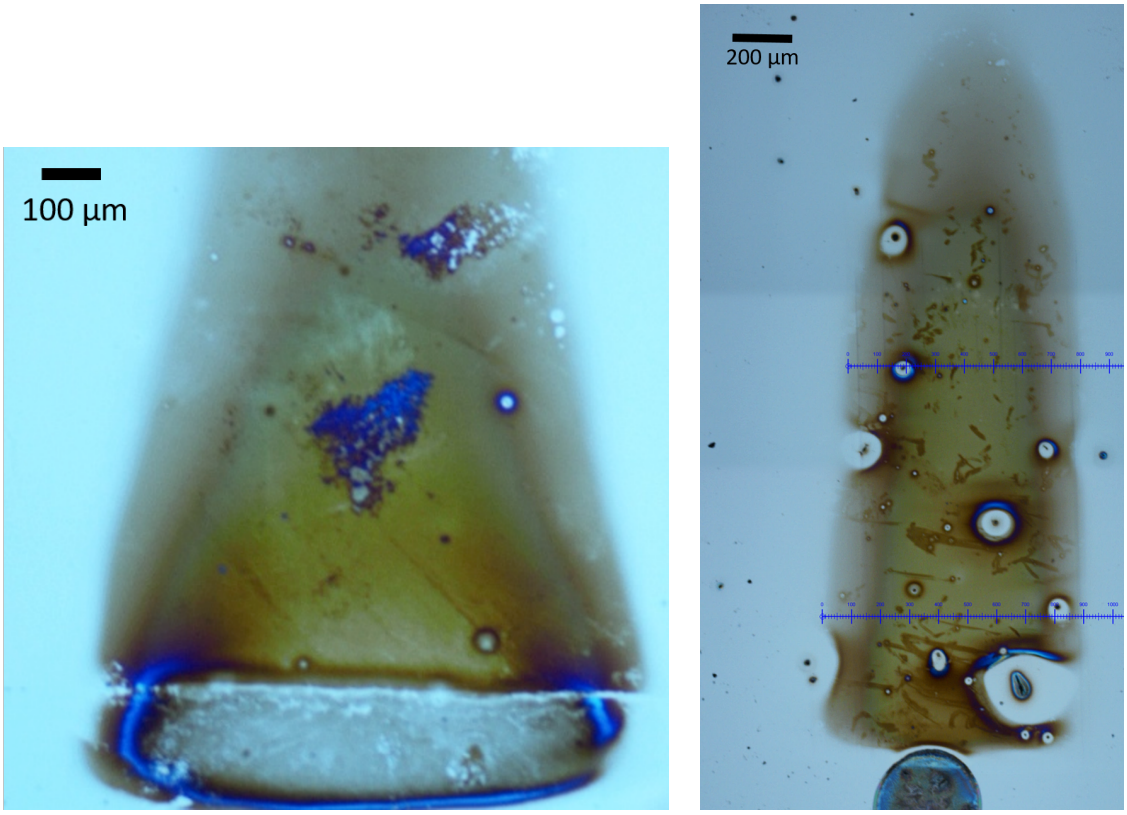

(a) Intrinsic InGaAs (b) Ion-Implanted InGaAs

Figure 5.8: Bright field micrograph comparing the damage behavior of the (a) intrinsic and (b) ion-implanted InGaAs samples from IBM. Both samples were scanned with the diode laser with a 10 ms dwell. The diode laser currents was set at (a) 54 A and (b) 53 A. The image for (b), the doped sample, was composed from combining 3 separate images, the blue lines are guides to measure the width of damage. Both samples show clear signs of visible damage, with the damaged region appearing dark.

sured using Raman spectroscopy. The trend in carrier concentration matches well with traditional electrical measurements for sheet resistivity. It was found that a capping layer on the samples helps prevent deactivation that most likely stems from arsenic evaporation. The capping layer did not prevent the samples from becoming damaged, which probably arises due to melting of the InP substrate. The spatially resolved data was converted from position on the sample

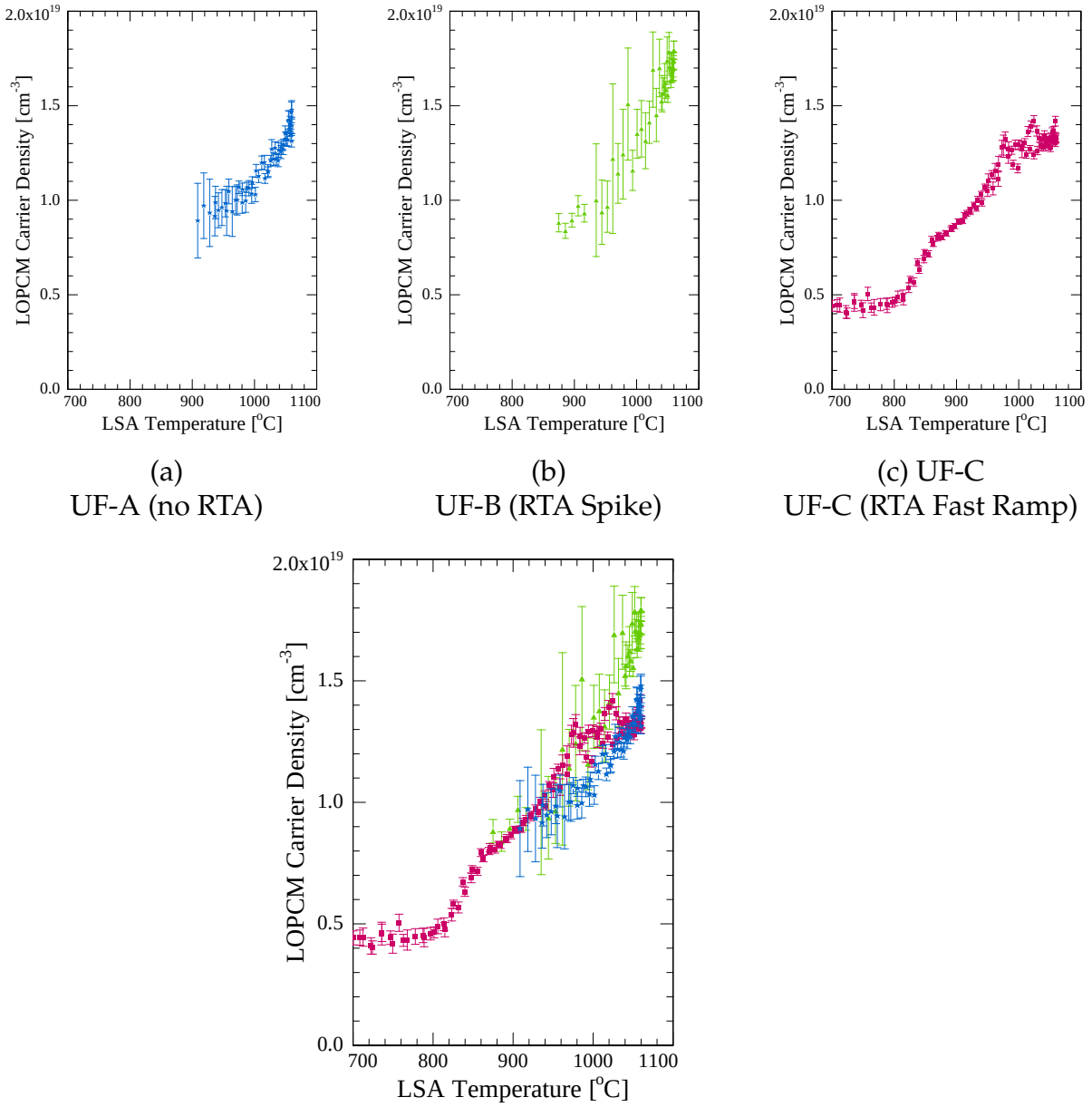

(a) UF-A (no RTA)

(b) UF-B (RTA Spike)

(c) UF-C UF-C (RTA Fast Ramp)

(d) Combined

Figure 5.9: Summary of LOPCM carrier concentration as a function of laser annealing temperature for the high dose, ion-implanted samples from University of Florida. Samples are (a) UF-A, (b) UF-B, and (c) UF-C. Laser annealing increased the carrier concentrations in all samples, with laser annealing being most effective on sample (b), where the carrier concentration exceeds the limit found by Lind *et al.* [24].

Table 5.3: Summary of the peak carrier density found using Raman Spectroscopy after laser annealing the ion-implanted InGaAs samples provided by University of Florida.

Sample ID	**LOPCM Position**	**Peak Carrier Density**
UF-A	1225	1.5×10^{19}
UF-B	1300	1.8×10^{19}
UF-C	1200	1.4×10^{19}

to temperature using the calibration developed for intrinsic samples. For high dose samples, the carrier concentrations reached and, in one case, exceeded the carrier density limit reached for longer time, lower temperature thermal processing. Overall, LSA was effective at activating ion-implanted samples.

CHAPTER 6

METASTABLE InGaAs

6.1 Motivation

Techniques capable of producing high, metastable, doping concentrations by growing-in dopants into lattice positions where they are electronically active, are a distinct viable approach to reach high carrier concentrations beyond what may possible with doping by ion-implantation. This chapter explores the stability of these high carrier concentrations when treated with short timescale, high temperature laser anneals. The intent of this study is to determine whether further thermal processing on samples with high grown-in carrier concentrations will cause deactivation to lower carrier concentrations, as is found for other annealing processes such as furnace annealing. For longer timescale anneals, both dopant diffusion and a decrease in carrier concentration was seen in silicon-doped InGaAs grown by MBE [24]. As-grown samples do not have the issue surrounding implantation damage, and samples can be grown with more precise control over the the defect populations, which ultimately control carrier concentrations. Samples were grown with dopants in active positions using either molecular beam epitaxy (MBE) or metal organic chemical vapor deposition (MOCVD).

6.2 Sample Details

The samples used in this study were grown by MBE and MOCVD and obtained through our collaborators at the University of Florida, as described below. All samples had a 15 nm of Al_2O_3 capping layer added after growth, deposited at 250 °C by atomic layer deposition (ALD) by our collaborators.

6.2.1 Metastable Si-doped InGaAs on InP

Silicon-doped $In_{0.53}Ga_{0.47}As$ was grown by MBE on semi-insulating InP at University of Delaware. The InGaAs was grown at 490 °C, with 320 nm of InGaAs topped with 60 nm InGaAs doped with silicon to a concentration of 7×10^{19} cm^{-3} (Figure 6.1a). This sample was the same as was used in the studies done by our collaborators at the University of Florida [83]. Our collaborators measured the carrier concentration in the MBE grown sample to be 2.86×10^{19} cm^{-3}.

6.2.2 Metastable Te-doped InGaAs on InP

Tellurium-doped InGaAs was grown by MOCVD on a semi-insulating InP substrate. The samples were provided to us by University of Florida, A previous study on the same samples was conducted by SEMATECH [10]. Undoped InP (100 nm) was initially deposited on InP, followed by Te-doped InGaAs (100 nm) grown at 660 °C (Figure 6.1b). According to their paper [10], carrier concentrations for these samples are 3.4×10^{19} cm^{-3}, with a sheet resistivity of 13.8 Ω/□, and a mobility of 1320 cm^2/V s.

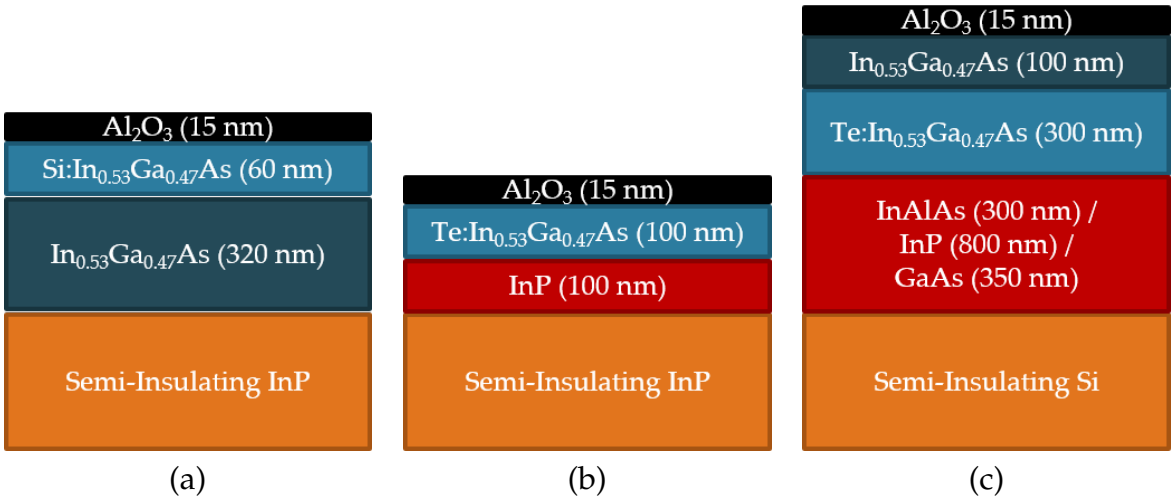

Figure 6.1: Schematic diagrams showing a cross-sectional view of the metastable samples with grown-in dopants: (a) Si-doped InGaAs on InP, (b) Te-doped InGaAs on InP, and (c) Te-doped InGaAs on Si.

6.2.3 Metastable Te-doped InGaAs on Si

Tellurium-doped InGaAs was grown by MOCVD on a Si substrate, the same samples as from the study published by SEMATECH [10]. On silicon substrates, a buffer layer structure was used to relieve the lattice mismatch between Si and $In_{0.53}Ga_{0.47}As$. The buffer layers consisted of GaAs (350 nm)/InP (800 nm)/InAlAs (300 nm) followed by ≈300 nm of Te-doped InGaAs with a ≈100 nm undoped InGaAs capping layer (Figure 6.1c). The InGaAs was grown at 500 °C. The GaAs and InP layers relieve lattice strain, whereas the large band gap InAlAs acts as an electronically insulating layer. For these samples, the reported carrier concentrations are 8.0×10^{19} cm^{-3}, with a sheet resistivity of 12.1 Ω/□, and a mobility of 841 $cm^2/V\,s$.

6.3 Laser Annealing Methods

All the samples were annealed using the diode laser, which heats the samples by direct band gap absorption.

6.3.1 Diode Annealing of Si-doped InGaAs on InP

The silicon-doped InGaAs was annealed with the diode laser at 75 A with a 5 ms dwell. The sample cracked into two pieces during laser annealing, showing evidence of crystalline slip visible in a microscope.

6.3.2 Diode Annealing of Te-doped InGaAs on InP

The anneal for the tellurium-doped InGaAs on the InP was performed at 75 A with a 5 ms dwell, which led to crystalline slip on the sample.

6.3.3 Diode Annealing of Te-doped InGaAs on Si

The samples on the Si substrates were annealed with a 5 ms dwell at 75 A, 85 A, 95 A, and 110 A (the maximum current of the diode laser). Even at the maximum current, the samples showed no visible signs of damage or annealing. To confirm this, we conducted absolute temperature calibrations using the highest annealing current. Gold dots deposited on the sample did not melt, indicating that the annealing temperature did not surpass 1064 °C. In addition, polymer

spun on the sample which was then annealed showed no signs of decomposition, indicating that the sample did not surpass 600 °C.

6.4 Raman Characterization of Metastable InGaAs Samples

Before and after annealing, the samples were characterized using Raman spectroscopy. The samples were probed perpendicular to the laser annealing scan to look for changes in activation as a function of annealing temperature. Based on the results on the intrinsic samples, the peak annealing temperature of the samples on the InP substrate was assumed to be 1062 °C.

6.4.1 Si-doped InGaAs on InP

After annealing, the two halves of the samples were characterized using Raman spectroscopy. Figure 6.2 shows the corresponding Raman LOPCM peak position.

The position on the sample was converted to temperature using the resistor spatial temperature profile and absolute temperature calibration from the intrinsic samples. It was assumed, based on the intrinsic sample data, that the peak temperature this sample reached before cracking was ≈1062 °C. The data clearly shows that the LOPCM peak position did not change after laser annealing, except for the section of the sample that was physically damaged, showing clear crystalline slip and cracking. Where there was visible damage, the LOPCM peak decreased, showing evidence of deactivation.

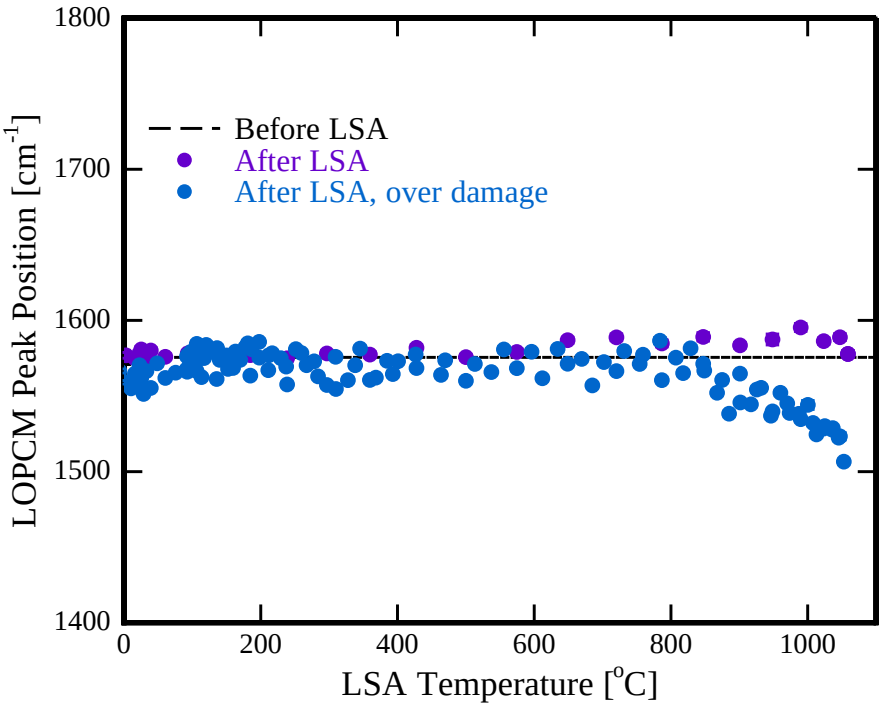

Figure 6.2: LOPCM peak position for Si-doped InGaAs on InP as a function of annealing temperature as determined from Raman spectra. The black dotted line indicates the measured peak position before laser annealing. The data points are from two measurements across the laser annealing profile. The purple points are from an area on the sample without slip whereas the blue points are over an area with visible slip.

6.4.2 Te-doped InGaAs on InP

The Raman spectra of a Te-doped InGaAs sample on InP before and after laser annealing, shown in Figure 6.3a, shows that there are few changes in the Raman signal after annealing. Taking a closer look at the LOPCM peak, Figure 6.3b shows that, before annealing, the LOPCM peak is located at 1748 cm^{-1}, whereas, after annealing, the peak position changes, with the appearance of visible slip on the sample. The peak does not change in the area of the sample located in

the center of the stripe that is undamaged. In the area on the sample where there is visible slip, the LOPCM peak splits into two peaks and red shifts to 1693 cm^{-1} and 1503 cm^{-1}. This red shift in the LOPCM peak after annealing indicates deactivation. The splitting behavior of the peak is most likely to be a result of the damage that occurred on the sample.

Haynes *et al.* [68] showed that As loss through pinholes and cracks is caused by stresses due to mismatches in the thermal expansion coefficient of the dielectric cap and the III-V material, and not from diffusion though the cap materials itself. For these Te-doped InGaAs samples, Orzali *et al.* [10] noted that, during growth, the tellurium has a high vapor pressure and surfactant properties that cause it to evaporate from surfaces and tends to segregate at step edges. In longer timescale anneals, Antonell *et al.* [127] found that Te-doped InP grown by MOCVD with a proximity cap deactivated during 1 minute RTA, lowering the electron concentration, but showed no evidence of Te diffusion. They hypothesized that the Te deactivated by forming small clusters. The dual peak may be a result of the Te deactivating (higher wavenumber peak) and forming small, inactive clusters in the cracked area exposed to ambient (lower wavenumber peak).

6.4.3 Te-doped InGaAs on Si

Raman spectra were taken both before and after annealing, as shown in Figure 6.4. After annealing, Raman spectra were taken across the annealed regions for each of the annealed currents, (85 A, 95 A, and 110 A). The Raman spectra showed no significant changes in the areas where the laser passed over the

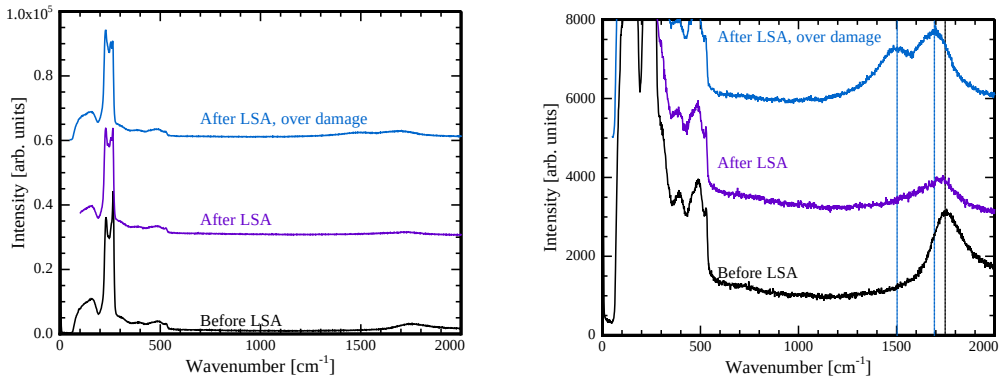

(a) (b)

Figure 6.3: Raman spectra of Te:InGaAs sample on InP before and after LSA. The spectrum after LSA is taken from the middle of the annealed region. The full spectrum is shown in (a); (b) shows a magnified view of the LOPCM peak position.

sample compared to areas that were unannealed. Based on this, and combined with the results from the temperature calibration, it is likely that the laser did not couple with this sample or, if it did, was only weakly coupled.

6.5 Discussion

In general, the metastable dopant concentrations stayed relatively stable during the 5 ms timescales of laser annealing. In areas that were visibly damaged with slip, the sample showed signs of deactivation. This deactivation behavior is expected at longer timescales. Our collaborators at University of Florida found that the carrier density in their samples decreased with 10-minute furnace anneals, as shown in Figure 6.5 [23]. The electrical results taken by our collaborators and the Raman results for each sample are summarized below in Table 6.1.

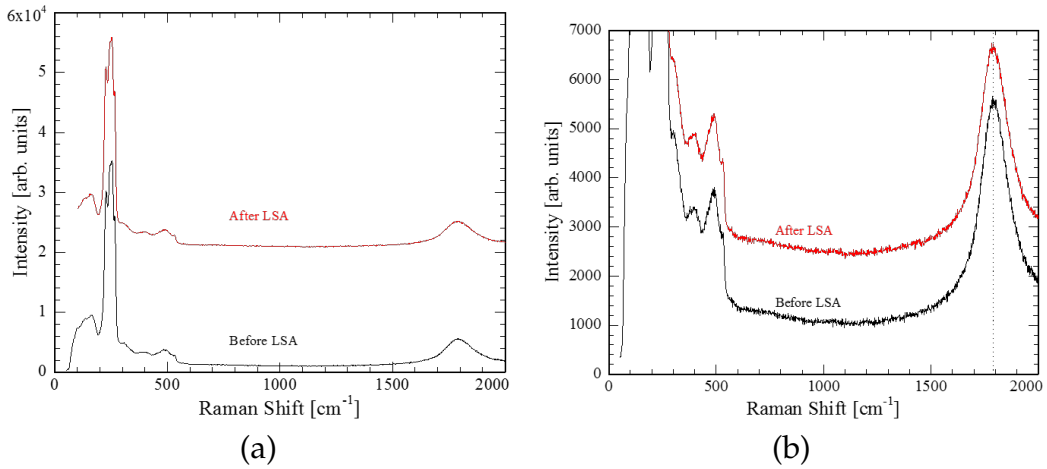

Figure 6.4: Raman spectra of Te:InGaAs on silicon before and after LSA. The after LSA spectra is taken from the middle of the annealed region. The full spectra is shown in (a), (b) shows a zoomed in view of the LOPCM peak position.

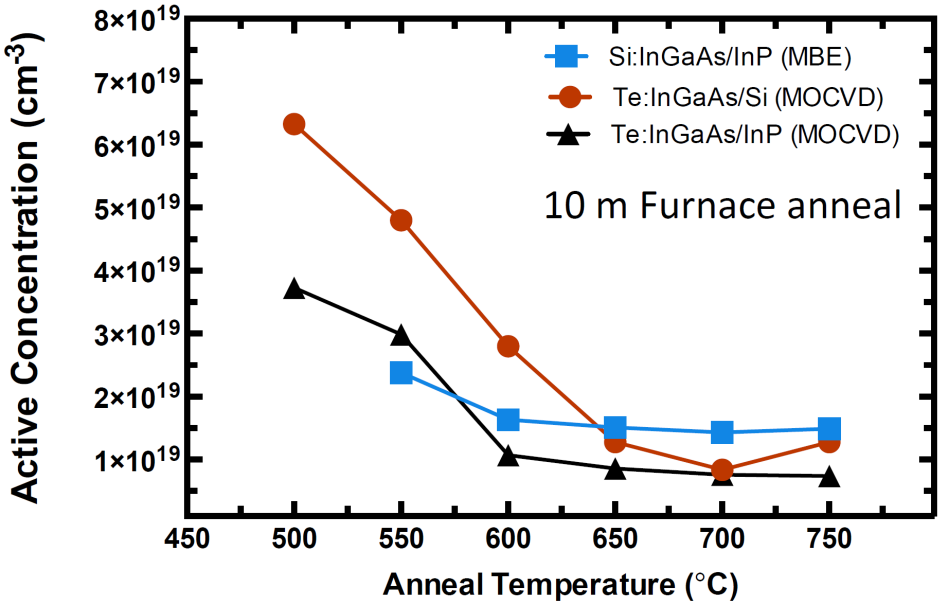

Figure 6.5: Furnace annealing results for the same type of samples annealed by LSA provided by University of Florida [23]. Samples with high, metastable carrier concentrations deactivated with 10 minute furnace anneals.

Table 6.1: Summary of electrical properties of the metastable samples. Overall, the metastable dopants did not deactivate after LSA in undamaged regions. In areas of the sample that damaged with visible crystalline slip, the carrier concentration decreased. Both the intact sample carrier concentration and the carrier concentration collected from the damaged areas are reported, with the damages results in parenthesis. The Te:InGaAs on Si did not show signs of annealing, even after scanning the laser with the maximum power, so the post-LSA results are not reported. Raman characterization of the sample showed no changes before and after the laser scan.

Sample	**Pre-LSA**			**Post-LSA**	
	n_e **Hall** $[cm^{-3}]$	**LOPCM** $[cm^{-1}]$	n_e **Raman** $[cm^{-3}]$	**LOPCM** $[cm^{-1}]$	n_e **Raman** $[cm^{-3}]$
Si:InGaAs on InP	2.86×10^{19}	1575	3.4×10^{19}	no change	no change
(Damage)				(1507)	(2.9×10^{19})
Te:InGaAs on InP	3.4×10^{19}	1748	4.7×10^{19}	no change	no change
(Damage)				(1503)	(2.9×10^{19})
				(1693)	(4.2×10^{19})
Te:InGaAs on Si	8.0×10^{19}	1790	5.1×10^{19}	N/A	N/A

There is a discrepancy between the measured Hall electrical carrier concentrations and the Raman measurements for the carrier concentrations. This is most likely to be the result of using a Raman calibration curve to find carrier concentrations at points which have to be extrapolated beyond concentrations where we have data. This problem is exacerbated by the log scale of the carrier concentration, making a small change in peak position result in a large change in carrier concentration. The Raman spectra seems to over-predict the carrier concentrations for both samples on InP. In addition, the probe depth on the Raman

system could be sampling a different part of the sample from that measured by the Hall measurements. Raman spectroscopy analyzes the sample based on the absorption length in the sample, whereas Hall measurements probe the most conductive layer, which may be buried deeper in the sample than Raman can measure. For the sample on Si, there is a 100 nm undoped InGaAs layer on top of the sample which may be the cause of the under-prediction. Assuming that the carrier concentration did not change since the initial measurements, it could be that the growth was not homogeneous across the entire wafer during growth, and the samples that were tested with Hall do not have the same electrical characteristics as the samples probed with Raman. That being said, probing with Raman across the sample adds a built-in control, so that a change in LOPCM peak position corresponds to a relative change in carrier concentration, even if the absolute carrier concentrations predicted are unreliable.

One of the remaining mysteries for the Te-doped InGaAs samples was the apparent difference in annealing between the samples on InP and the samples on silicon. Since the laser should be heating that sample by direct band gap absorption in the InGaAs film and the InGaAs has a reasonable absorption length, the substrate should not have a direct effect on the laser's ability to heat the sample. To elucidate possible differences between the samples grown on InP versus Si, we measured the Raman spectra before annealing for the different tellurium-doped samples, as shown in Figure 6.6.

The sample on the InP substrate exhibits Raman peaks that are typical for the samples tested previously, namely, with strong LO phonon peaks and weaker TO peaks, the gray lines marking the primary phonon peak positions (InAs-like: 225 cm^{-1} (TO), 233 cm^{-1} (LO); GaAs-like: 255 cm^{-1} (TO), 269 cm^{-1} (LO).

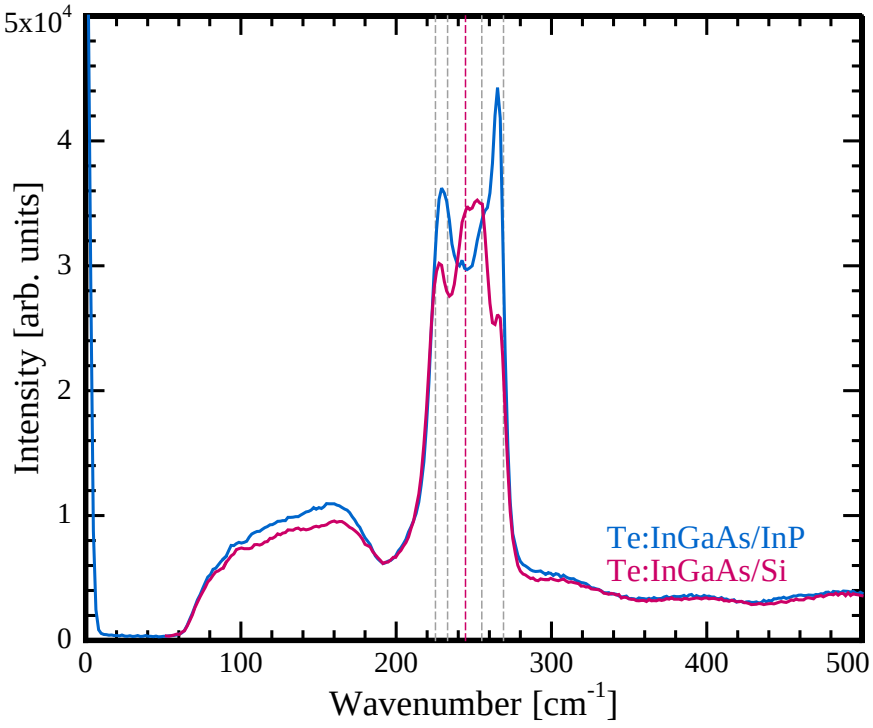

Figure 6.6: Raman spectra with a focus on the primary phonon peaks (with their positions marked as gray dotted lines) for Te:InGaAs on an InP substrate or on a Si substrate. The Te-doped sample on InP looks typical for the samples studied in this thesis. The Te:InGaAs on Si, however, has a large peak in the position of the R* disorder induced mode, with the position of this mode marked with a red dotted line. This is atypical compared to the other samples studied.

The sample on the Si substrate, however, is markedly different. It seems to show weaker LO phonon peaks and is dominated instead by a disorder-induced mode at 244 cm^{-1} (marked with a red line). This disorder-induced mode, R*, has been identified in other InGaAs Raman samples [128, 107]. Both samples show evidence of strain, as shown by the shifted positions of the primary phonon peaks from their relaxed positions [129]. Compressive strain in the doped layer was also noted after analyzing the XRD data for these samples, the large size of

the Te dopants leads to an increase in lattice constant [10].

A review of some results due to Bhattacharya *et al.* is instructive here [40]. They observed two types of order, namely, atomic order and phase-separated order. InGaAs, especially in case where there are roughly equal compositions of In and Ga, has been found to be ordered on the cation lattice, and its atomic ordering is growth-dependent. The most common form of ordering is the Cu-Pt structure, which has been observed when grown with vapor phase epitaxy on (001)-oriented substrates. On samples grown with molecular beam epitaxy on (110)-oriented substrates, a Cu-Au-I structure is observed. The Cu-Pt-I ordering is more favorable thermodynamically, but ordering occurs at the surface during growth, so it is not necessarily more kinetically favorable depending on the growth surface and growth method. Additionally, on related GaInP systems, it was found that an increase in growth rate decreases atomic ordering and atomic ordering reduces the band gap [40]. For InGaAs samples, Nojima *et al.* found that the optical properties vary with growth method, and the growth temperature was particularly important [130].

Taking all this into account, the Raman results can be re-evaluated. The sample grown on the silicon substrate has a large Te concentration, approximately 10x that of the sample on InP substrate, 5.5×10^{20} cm^{-3} compared to 5.7×10^{19} cm^{-3}, providing strain into the lattice [10]. The InGaAs capping layer grown on top is then under tensile stress, and lattice mismatch combined with the higher growth temperature could induce mismatch dislocations and frustrate ordering, leading to the large disorder induced Raman peak. This would impact the optical properties of the sample. Assuming the mechanism for coupling with the diode laser is direct band gap absorption in the InGaAs layer,

the disorder and doping should lead to tail states (known as the Urbach Tail) within the band edges, decreasing the band gap and leading to increased absorption [105]. Thus, disorder induced from the large dopants atoms is not a satisfactory explanation for the poor coupling behavior between the film and the laser.

Another possibility is that the high carrier density could be the reason the sample is not annealing as expected. Degenerate doping of InGaAs pushes the Fermi level into the conduction band, and, because of the small electron mass of InGaAs, this can drastically increase the absorption edge. This has been observed and reported by a few groups [131, 132, 11] and is know as the "Burstein-Moss shift." With the diode laser energy of 1.26 eV, and the band gap of InGaAs at 0.75 eV, an approximate shift of 0.5 eV would be needed to change the InGaAs from absorbent to transparent to the diode laser light. Muñoz *et al.* found that, for InGaAs with a carrier concentration of 3.9×10^{19} cm^{-3}, the absorption edge increased to 1.15 eV [132]. Considering that the Te:InGaAs sample has a doping density well beyond that, it is a reasonable explanation for the strange behavior. If the InGaAs is transparent to the diode laser, the light should be absorbed in the silicon substrate. The substrate is lightly doped so the absorption length is long, as well at the thermal transport length. This could make it so that surface temperature on the sample, where the temperature calibrations read, is low.

6.6 Summary

The dopant concentrations in the metastable samples are stable under laser annealing up to sample damage, which occurs through crystalline slip or crack-

ing. Any area of the sample that damages also exhibits deactivation. Figure 6.7 directly compares the carrier concentrations results for the high dose ion-implanted samples from the previous chapter to samples with the grown-in dopants without damage investigated in this chapter. It is evident from this graph that the samples grown with metastable dopants have much larger carrier densities compared to the ion-implanted samples activated by laser annealing. Depending on the carrier concentration requirements, the ion-implantation may not provide a high enough carrier concentration. For samples with metastable carrier concentrations, subsequent thermal processing should be kept short to prevent deactivation if using high temperatures.

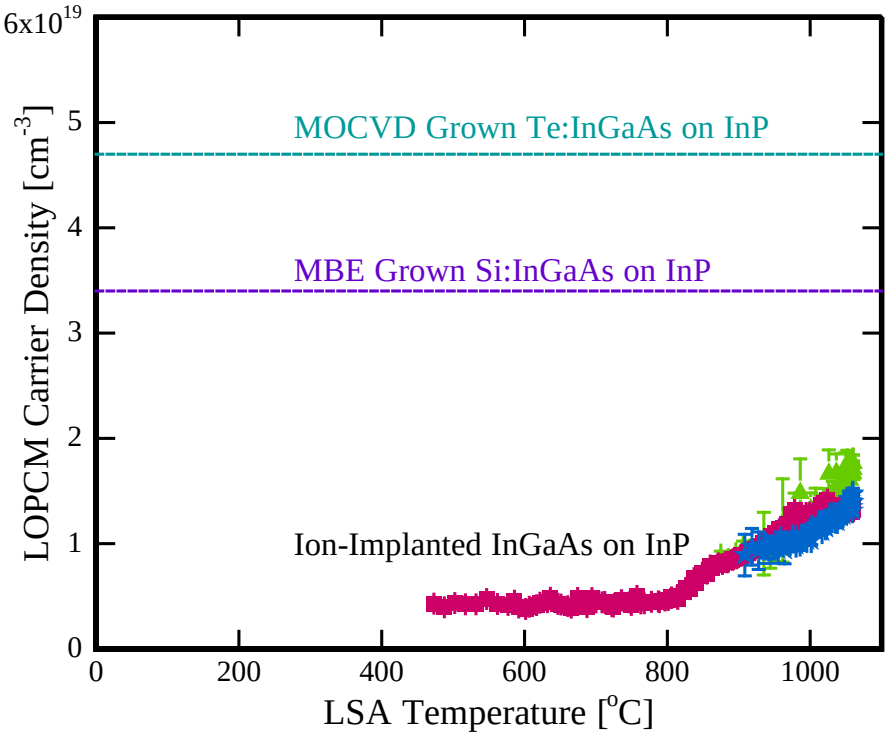

Figure 6.7: Comparison of the laser annealing results for the ion-implanted samples versus metastable samples with grown-in dopants (represented as a line). Although improvements were made to the activation limits for ion-implanted dopants, they well below the carrier concentrations achievable with growing in metastable dopants. The metastable dopant concentrations unchanged with laser annealing, with the exception of deactivation occurring where there was crystalline slip or where the sample cracked.

CHAPTER 7

GaN

7.1 Motivation

Gallium Nitride (GaN), as with other related III-N materials, combine fast carrier transport and high breakdown voltage, which are essential for power and high voltage applications. Device characteristics and performance are critically reliant on controlled *p*- and *n*-type doping. While *in-situ* doping can achieve reasonable activation levels, spatially selective doping by ion-implantation remains challenging. In particular, *p*-type dopants are notoriously difficult to activate in GaN by thermal annealing and must be grown in using metastable methods. In this work, we will explore the efficacy of laser spike annealing to activate and deactivate *n* and *p*-type dopants in GaN. We investigated the behavior of both *in-situ* and ion-implantation-doped samples.

7.2 Sample Details

Wurtzite-structured GaN samples were used in this study, provided by our collaborators in the Xing research group at Cornell. The samples were up to 1 cm x 1 cm in size. Initial tests for laser annealing were conducted to verify the feasibility of annealing using either the CO_2 or diode laser. Three general sample types were used for all the studies, as shown in Figure 7.1. GaN is notoriously difficult to grow with controlled defects, so carefully grown epilayers of GaN with well-controlled defects are fabricated on substrates of sapphire or GaN. In

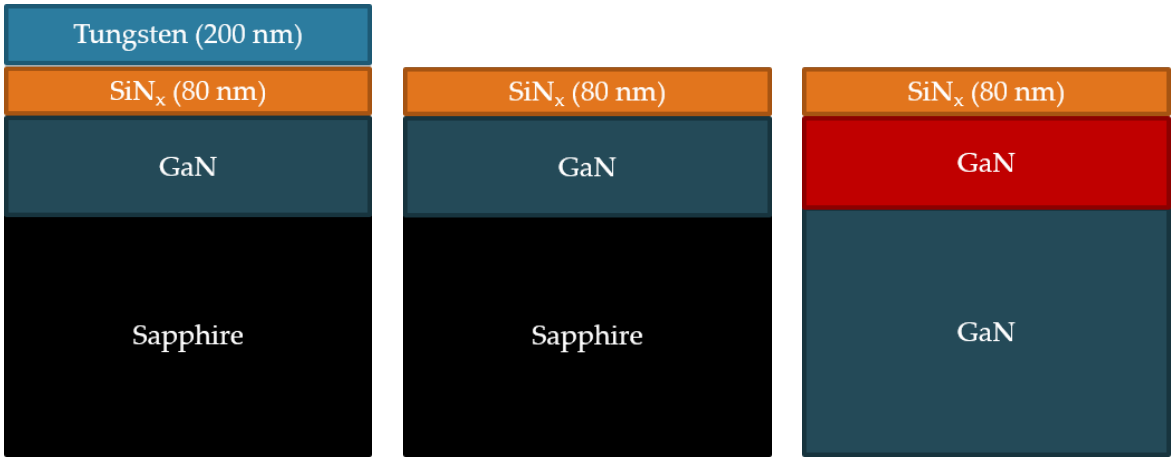

Figure 7.1: Cross-sectional view of the GaN samples: (a) diode laser-annealed sample featuring a tungsten absorber layer, (b) CO_2 laser-annealed GaN on sapphire, and (c) CO_2 laser-annealed GaN on GaN.

the case of the GaN on GaN sample, the substrate has higher levels of defects, and the lower defect GaN epilayer is needed to make well-controlled devices. On all the samples, an ≈80 nm PECVD silicon nitride capping layer was added to prevent nitrogen evaporation during high temperature annealing.

GaN is transparent to the 980 nm light of the diode laser. To aid with light absorption during laser annealing, an additional 200 nm layer of tungsten was deposited to ensure optical coupling between the sample and the laser (see Figure 7.1a). The CO_2 laser annealing study was conducted on GaN films epitaxially grown on either GaN or sapphire substrates (Figure 7.1b and Figure 7.1c).

After the feasibility of laser annealing was established on intrinsic GaN films, as will be discussed in the following section, *p*-type GaN samples were grown with a typical *p*-type dopant for GaN (Mg) on either GaN or sapphire substrates. Some of these samples were subsequently ion-implanted with the *n*-

type dopant, Si, with a box implant to a target concentration of 1×10^{19} Si/cm^3 and to a depth of 400 nm, with the ultimate goal of forming *p*-*n* junctions. The non-implanted samples were used as a control to compare to the samples implanted with Si.

7.3 Laser Annealing Methods

Our initial studies focused on the feasibility of conducting millisecond laser annealing of GaN samples in an atmosphere of air. Laser annealing critically relies on the optical properties of the sample at the laser wavelength. While laser annealing has been previously explored for dopant activation in ion-implanted GaN, the majority are based on pulsed lasers [87, 58]. One group used a CW CO_2 laser to anneal GaN with light absorption occurring in the sapphire substrate, for annealing times on the order of minutes [133]. For this study, both the CO_2 and diode continuous wave lasers were explored for annealing.

For the diode laser, GaN is transparent to the 980 nm light, so a 200 nm tungsten film was deposited to ensure optical coupling. The absorption of the sample was tested at low laser power (the diode laser was set just past the laser turn on current threshold), at which the sample reflected roughly 50% of the light. This implies that the other 50% of the light was transmitted to the sample. At the CO_2 laser wavelength (λ=10.6 μm), the absorption coefficient (216 cm^{-1}) and low reflectivity (8%) ensure effective coupling directly to the GaN for laser annealing [90].

7.4 Laser Annealing Temperature Characterization of GaN Samples

As with the samples from previous chapters, the approximate maximum annealing temperature reached during laser annealing was established using the dwell-dependent, thermal decomposition behavior of a block copolymer film (poly(styrene-block-methyl methacrylate), 70 wt.% polystyrene), previously characterized to well-calibrated anneals on silicon substrates. Polymer films, ≈60 nm thick, were spun on the sample. Polymer decomposition following laser annealing is clearly visible in the optical images and was quantitatively analyzed using the Plot Profile function in ImageJ. The GaN samples have not been characterized using resistor measurements; consequently, the spatial thermal profile has not been established. This means that the farther away on the sample from the polymer decomposition, the less certain the predicted temperature.

7.4.1 Diode Temperature Characterization

A tungsten-coated, ion-implanted, GaN $p-n$ junction sample was annealed with the 980 nm diode laser using a 5 ms dwell. Gold dots were deposited on the sample and then polymer was spun onto the sample. The sample was annealed with single scans across the sample, ramping the power in 5 A increments until the sample showed visible signs of annealing. The sample broke into two pieces at 65 A without showing signs of the gold melting. Copper tape was then added to the edges of the remaining half of the sample to reflect the diode light, thus

protecting the sample from thermal shock from the laser entering and leaving the sample. The copper tape covered the gold dots so they were no longer used as a temperature calibration. The sample was then laser-annealed, starting at 65 A, up 95 A, where the sample shattered. Based on the width of the single polymer decomposition line in the dark field image and no clear transition to full decomposition in the bright field micrograph (as shown in Figure 7.2), the peak annealing temperature reached by the sample was ≈750 °C. This predicted peak temperature constitutes a large extrapolation of temperature from polymer decomposition reference point based on the spatial profiles of silicon used in our lab. Since the polymer did not fully decompose, the temperature must be below ≈810 °C. A large crack that occurred during annealing is also apparent in Figure 7.2. Because this type of damage was not apparent in the CO_2 laser-annealed samples on sapphire, we attribute this damage to thermal stress associated with the longer dwell time, the broad focus of the diode laser, and the light absorption in the thick tungsten layer. This temperature, at this short timescale, will be insufficient to activate ion-implanted dopants. Based on this low damage threshold, the remainder of the studies focused on using the CO_2 laser to anneal samples.

7.4.2 CO_2 Temperature Characterization

For all other GaN samples, annealing behavior under CO_2 illumination was explored with a 1 ms dwell. Effective coupling was established for GaN on both GaN and sapphire substrates. Between the two sample types, large variations in annealing behavior was evident. In general, samples on sapphire damaged at a lower power density, which could be a result of low thermal conductivity of

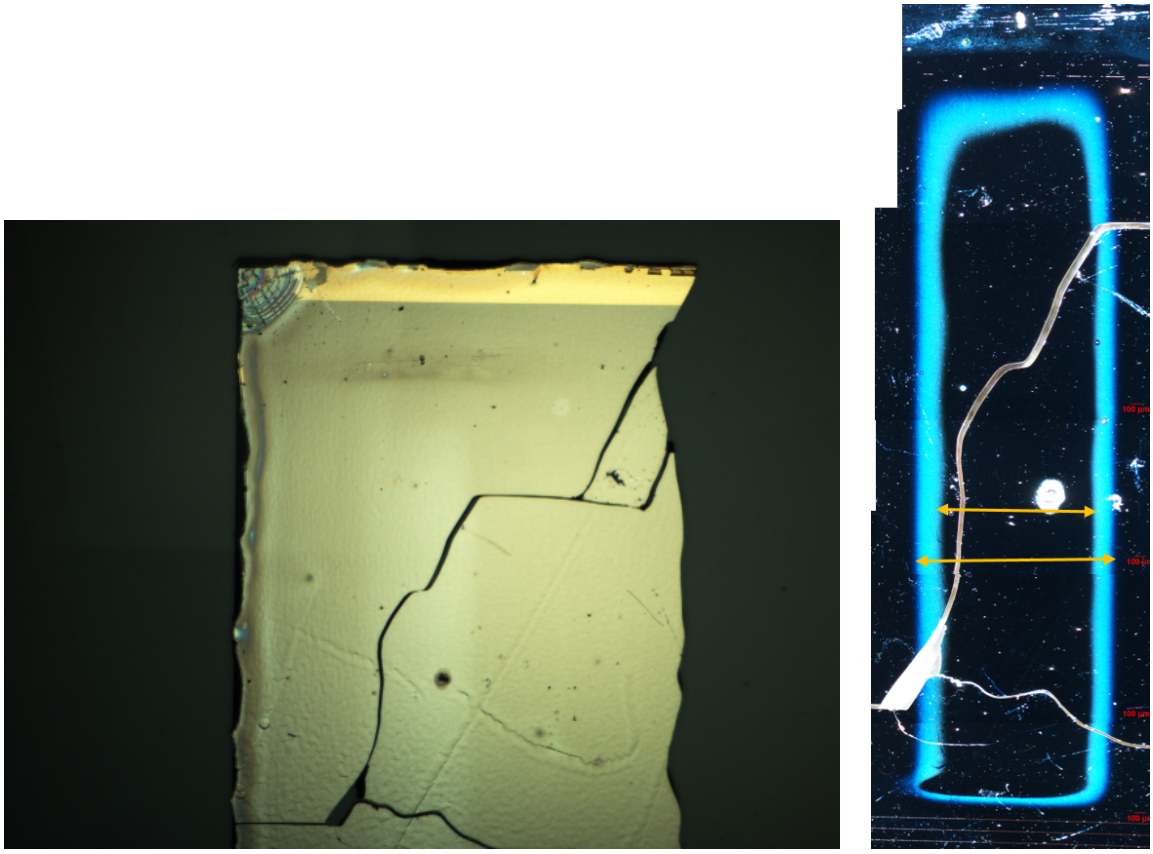

(a) (b)

Figure 7.2: Micrographs of the polymer- coated GaN sample after annealing at 95 A for 5 ms, (a) bright field and (b) dark field. The sample cracked during laser annealing, as evident in the images. A faint color difference where the sample has lightened in the bright field image, shows the beginning of polymer decomposition. In the dark field image (b), the bright blue outline more clearly identifies the start of polymer decomposition. The absences of a second set of bright blue outlines confirms that the sample did not reach a high enough temperature to completely decompose the polymer. Thus, the sample reached a temperature between the initial and complete decomposition temperature of the polymer.

sapphire and possible strong light absorption in the sapphire due to the long absorption length of GaN. The GaN on GaN substrates damaged at higher power densities. In both cases, the annealing and damage threshold changed significantly based heterostructure and doping, making it very difficult to compare results across samples. This also made it so the damage threshold and prediction of annealing temperature predictions had to be re-established for each sample type, a time-consuming process. This leads to large inconsistencies and uncertainty when comparing results across different sample types and makes it extremely difficult to not only understand the cause of the differences seen between samples but also if those differences are repeatable.

Initial temperature calibrations were based on the onset of damage on GaN substrates at moderate CO_2 powers (46 W or 850 W/cm), Figure 7.3. For the 1 ms dwell, the polymer completely decomposes at 900 °C, allowing a calibration curve to be developed. Figure 7.3a and Figure 7.3b show the result of this temperature calibration The polymer is dark and the GaN substrate is light colored. Part of the polymer on the top of the sample was removed with solvent as shown in Figure 7.3b before annealing to show clearly where the polymer decomposed. Figure 7.3a shows scans of increasing power density. From left to right: 28 W shows partial polymer decomposition, 30 W show partial decomposition, and 32 W shows complete decomposition. Figure 7.3b displays a scan at 46 W, with full decomposition and sample damage.

Based on the width of the polymer decomposition, we estimated the peak annealing temperature using Figure 7.3c and Figure 7.3d. As expected, this relationship is roughly linear. At the power density where the sample damages (850 W/cm), the peak temperature becomes dependent on the damage extent. If

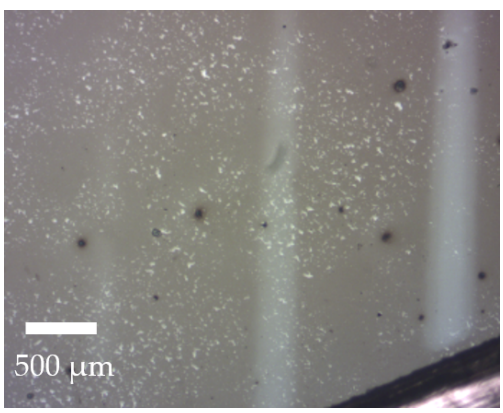

(a) 1 ms: 28 W, 30 W, and 32 W

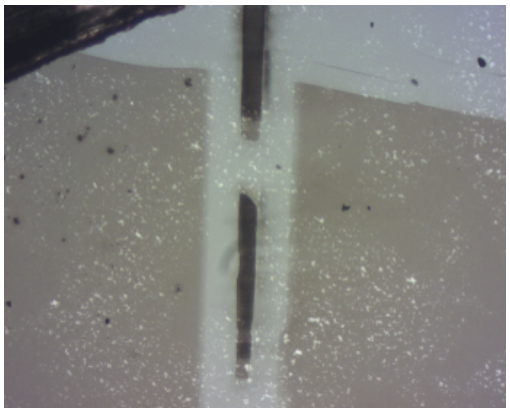

(b) 1 ms: 46 W

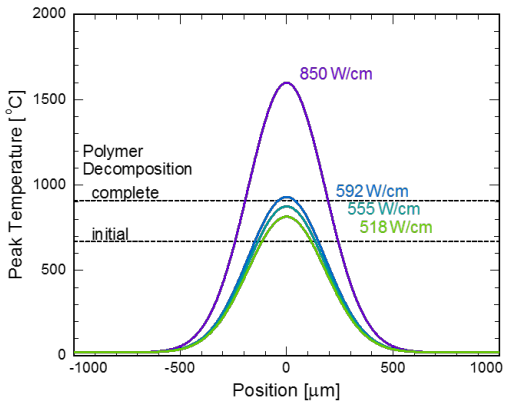

(c) Spatial temperature

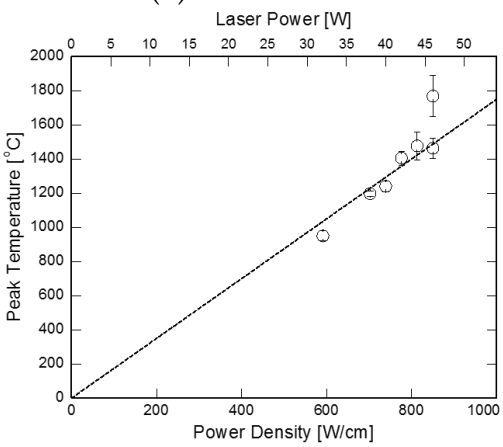

(d) Peak Temperature

Figure 7.3: The result of the temperature calibrations using 1 ms scans with the CO_2 laser to anneal GaN substrates. The bright field micrographs (a,b) show the polymer coated areas as dark, and the areas that the polymer has thermally decomposed as light. (a) From left to right, anneals were performed at 28 W, 30 W, and 32 W. The polymer partially decomposed in the 28 W and 30 W scan and completely decomposed in the 32 W scan. (b) Annealing was performed at 46 W, which reached a high enough temperature to fully decompose the polymer as well as thermally damage the sample. The sample damage appears black in the middle of the scan. On the top right portion of the sample that appears light, the polymer was removed with solvent prior to annealing to make the polymer decomposition easier to identify. (c) The expected spatial profile is based on the spatial profile from the thin film resistors on silicon combined with the measured polymer widths from (a) and (b). (d) The resulting peak temperature estimations (including additional samples) shows that the predicted peak temperature follows a roughly linear trend with laser power, as expected. Peak temperatures reach an estimated 1400-1600 °C before damage is occurred.

the sample cracks, it reaches a lower temperature compared to sample that has visible thermal damage but no cracking. The peak temperature that the samples can reach is estimated to be between 1400-1600 °C based on this study, although there is a large uncertainty in predicting temperatures far from the 900 °C calibration point. The use of the silicon spatial profiles for initial estimates for predicting the spatial profiles appears to be justified, based on GaN and silicon having very similar thermal conductivities.

This analysis was repeated for doped heterostructure samples grown on GaN substrates, as summarized in Figure 7.4. The annealing conditions shown in Figure 7.4a (44 W, 46 W, and 48 W), all show complete polymer decomposition (the polymer is orange in the image and complete decomposition occurs when the sample turns lighter in color). Additionally, all samples show a color change to blue in the areas with temperatures above the polymer decomposition temperature. The 46 W and 48 W annealing scans show visible annealing damage on the sample.

Comparing the two peak temperature graphs, as shown in Figure 7.5, the device structures do not couple as strongly with the laser, as evidenced by the higher powers needed to reach the same peak temperatures. By comparing the power density and predicted temperature that damage occurred at between the two samples, it appears that the device sample damage at lower temperature by ≈300 °C.

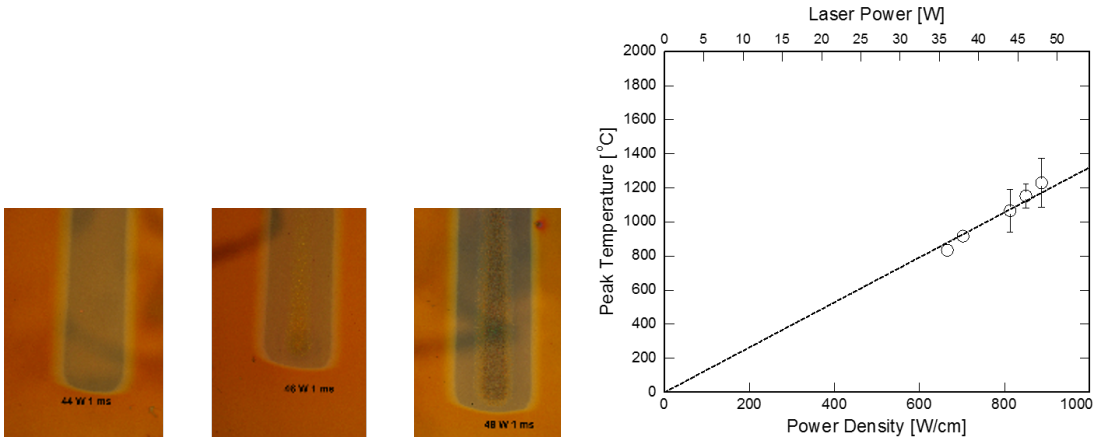

(a) (b)

Figure 7.4: The result of the polymer decomposition temperature calibrations using 1 ms scans with the CO_2 laser to anneal GaN device structures on GaN substrates: (a) (from left to right) anneals at 44 W, 46 W, and 48 W showing full polymer decomposition and (b) the resulting peak temperature estimations.

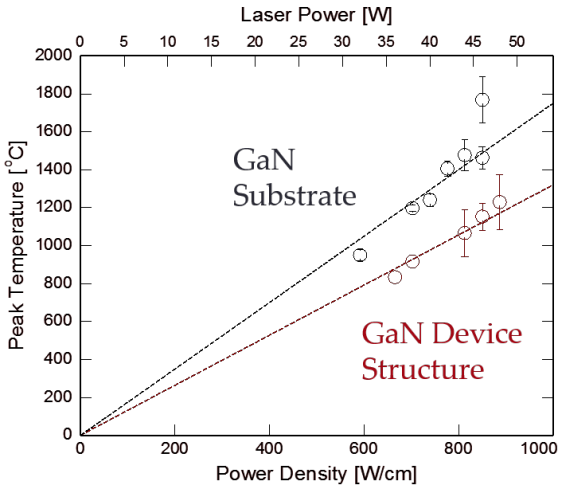

Figure 7.5: Comparison of the temperature calibrations for two of the CO_2 laser-annealed samples on GaN substrates. The samples on GaN substrates couple with the laser more effectively and are able to reach a higher estimated temperature before damaging.

7.5 Raman Characterization of GaN Samples

Previous groups have used Raman spectroscopy as a powerful probe of crystalline quality, implantation damage, carrier concentrations, and relative hole concentrations in GaN [18]. This work uses micro Raman spectroscopy, using the Renishaw InVia Confocal Raman microscope in backscattering mode with 488 nm excitation and a spot size of 1 μm, to rapidly characterize the GaN properties as a function of position on the sample and, ultimately, annealing temperatures once the spatial temperature and peak temperature are well-characterized.

We collected Raman spectra perpendicular to the annealing stripe for the ion-implanted samples annealed at 850 W/cm with a 1 ms dwell. Since the GaN samples are optically transparent, it was found to be critical to use the confocal mode on the microscope in order to eliminate undesired signals from deeper layers within the sample or even the tape securing the sample to the slide.

Raman spectra were mapped in 5 μm steps over the ion-implanted GaN sample on sapphire. A portion of the collected spectra from both the right and the left of the laser scan are displayed as offset waterfall plots in Figure 7.6.

The Raman spectra show the expected characteristic GaN peaks [18] (E_2^H at 568 cm^{-1} and A_1(LO) at 734 cm^{-1} and smaller, implantation damage-related peaks at 300, 420, 670 cm^{-1}, with initially little change in intensity with laser annealing. As the annealing temperature is increased (moving close to the center of the annealing stripe), a peak appears at 480 cm^{-1} and shifts to 515 cm^{-1} as annealing temperature is increased. This is initial evidence of the frequency shifting TO phonon-plasmon coupled mode that would indicate *n*-type carriers

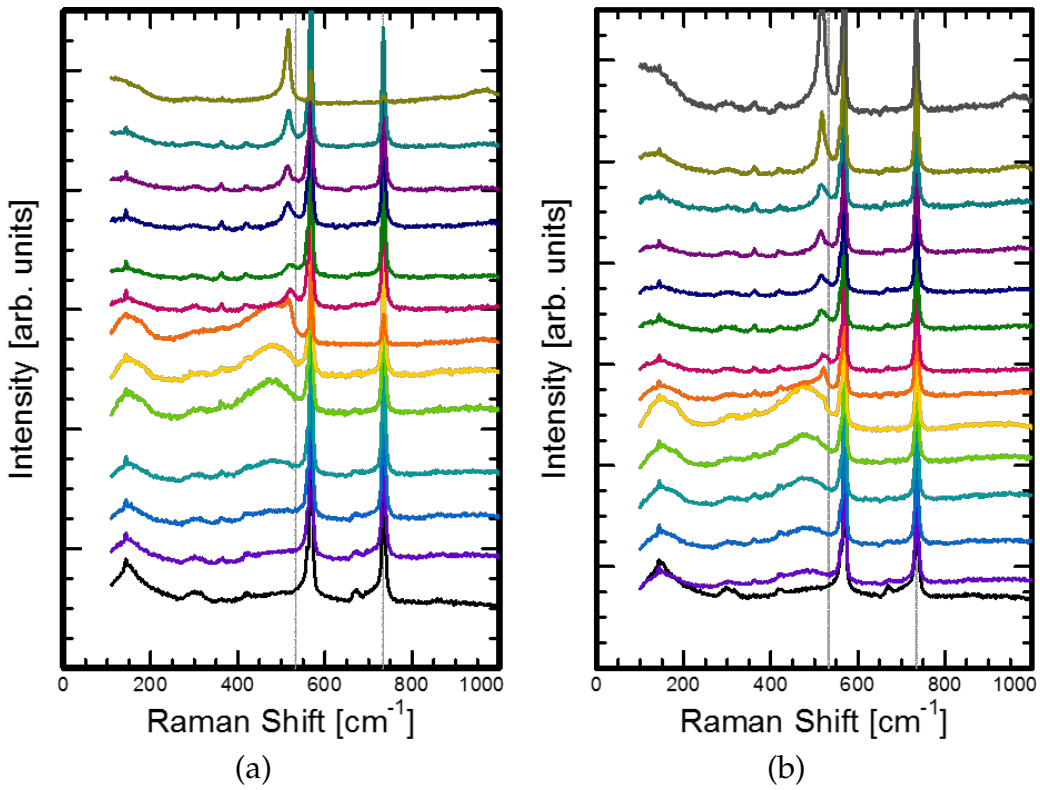

Figure 7.6: The Raman spectra taken in 5 µm steps from the left side of the annealing stripe (a) and the right side (b). Moving up the plots, the spectra are taken closer to the laser stripe, the bottom black line being unannealed. The gray lines are to guide the eye regarding the position of the TO and LO phonon modes. As the laser annealing temperature on the sample is increased, coupled mode peaks appear on the sample around 480 cm^{-1} and shifts to 515 cm^{-1} at higher annealing temperatures. The shift in this peak shows that the implant becomes active and the carrier concentration on the sample increases as the annealing temperature is increased.

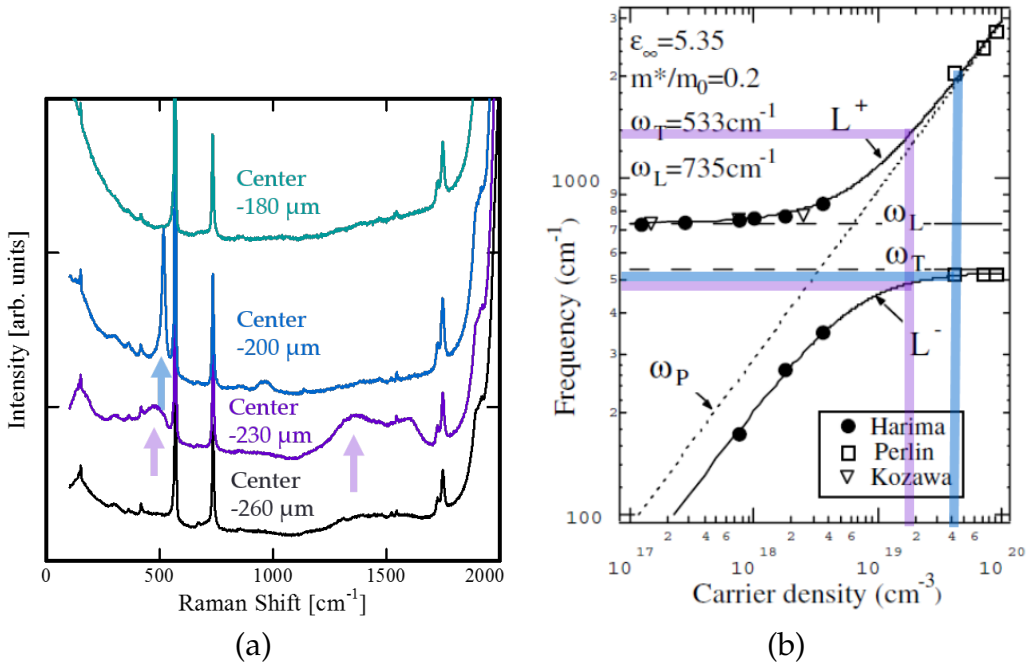

Figure 7.7: The Raman spectra taken from the left side of the annealing stripe (a) and the calibration for converting peak position to carrier concentration (b). Moving up the plots, the spectra are taken closer to the laser stripe, the bottom black line being unannealed. The colored arrows in (a) identify the coupled peak positions and their corresponding carrier density is highlighted in (b). The coupled peaks show that the sample exhibits dopant activation, with carrier concentrations in the 1×10^{19} to 5×10^{19} cm^{-3} range.

[18].

Looking at higher resolution spectra collected for larger 20 μm steps across the sample, both the L^- peak and the L^+ can be resolved in Figure 7.7a. The arrows point out the coupled mode peaks. Figure 7.7b provides a graphical representation of predicted carrier concentrations based on the peak position.

7.6 Discussion

One of the most interesting results of this analysis is that the predicted carrier concentration surpasses the 1×10^{19} Si/cm^3 implant concentration. If the predicted carrier concentration from Raman is correct and the implant was correctly measured, the increase in carriers would have arise from other charged defects, perhaps thermodynamically favored charge vacancies [48] or the high laser annealing temperatures are allowing the capping layer to act as a source of dopants [67, 76, 77] or maybe another unidentified source. More work is needed in order to identify if the Raman predicted carrier concentration in correct. If the carrier concentration is indeed greater than the implant concentration, the next step is to identify the type of defect that is leading to this behavior. In order to gain a greater understanding of this system, other characterization methods beyond Raman should be used.

7.7 Summary

This work shows the feasibility of using short timescale, high temperature, laser spike annealing of GaN materials with a high power CW CO_2 laser. The wavelength of the CO_2 laser couples efficiently to GaN films and substrates as well as GaN on sapphire substrates. Samples reached peak annealing temperatures that are estimated to be between 1200-1600 °C before damaging, based on an absolute temperature calibration using a thermally decomposing polymer. On ion-implanted samples, we studied the activation behavior using Raman spectroscopy. We found evidence of an increase in carrier density in the laser annealed sample, though the carrier density surpasses the concentration of the

implant. More work is needed to confirm this result.

CHAPTER 8

CONCLUSIONS AND FUTURE WORK

8.1 Conclusions

This work focused on exploring the efficacy of short timescale laser annealing of III-V materials, specifically InGaAs and GaN, to improve dopant activation and finding ideal characterization techniques to probe the structural and electrical changes in the samples that resulted from this laser annealing. These III-V materials have ideal electronic properties that position them as good candidates to make improvements in high-efficiency and high-performance electronic device applications. However, controlling the doping process in these compound materials has proven to be unexpectedly complicated, especially with respect to the response of the material to thermal processing. Traditional annealing techniques, such as furnace annealing and rapid thermal annealing, are characterized by longer annealing times and lower annealing temperatures than are explored in this thesis. The long annealing times are beneficial in terms of their ability to repair crystalline damage made to the material by doping through ion-implantation, but the long times leads to properties that are limited by thermodynamics. The lower annealing temperatures have the disadvantage that they limit the activation of dopants. Unfortunately, the vapor pressure of the group V atom (arsenic or nitrogen, in the cases studied here) causes the material to thermally decompose as the annealing temperature is increased, which is compounded by the longer annealing times. This behavior provided the motivation to significantly limit the annealing time through the use of sub-millisecond laser annealing (to limit As or N evaporation) at a suitably high enough power to al-

low the samples to reach higher temperatures than is afforded by furnace and RTA. Hence, increasing the proportion of activated dopants while simultaneously limiting the damage that occurs in the material due to thermal decomposition.

Using lateral gradient laser spike annealing (LSA) combined with spatially resolved characterization techniques, we were able to conduct a large-scale design of experiments to explore short timescale anneals with a built-in, unannealed control on the sample. This set up allowed us to analyze the effect of annealing time (in the time range of 250 µs to 10 ms) and the entirety of temperature space from unannealed locations at room temperature up to temperatures that lead to thermal damage, *all within a single LSA scan*. We combined these fast laser annealing scans with the rapid, non-destructive characterization technique of Raman spectroscopy, used to monitor the progress of crystalline repair and dopant activation simultaneously. We found that the high temperatures that could be reached during LSA were effective at activating dopant concentrations that were kinetically limited, although the short timescales did not completely repair crystalline damage. Even at the short timescales of LSA explored, thermal decomposition through evaporation was evident on uncapped samples. By combining protective capping layers with LSA, the evaporation of group V atoms can be effectively limited, even at the high temperatures unattainable by longer-timescale annealing processes. For high-dose, ion-implanted samples, we were able to improve the number of activated dopants from the thermodynamic limit of 1.4×10^{19} cm^{-3} to 1.8×10^{19} cm^{-3}, a 29% increase. To put this result in context, an improvement smaller than this would be considered as grounds for immediate adoption in the semiconductor industry. Importantly, this work also shows that, unlike longer time-scale annealing methods, LSA allows us to

retain the metastably high levels of activated dopants in III-V samples made possible by processes such as MBE and MOCVD, right up to the point at which the sample becomes damaged by the action of the laser-induced high temperatures. In contrast, furnace annealing and RTA of such metastably high dopant concentrations results in a significantly reduced level of activated dopants to the thermodynamic limit of 1.4×10^{19} cm^{-3} given sufficient annealing time and temperatures. The limitation on activation behavior for ion-implanted silicon dopants in InGaAs seems to result from the amphoteric nature of the dopants and implantation damage, similarly to what is observed as a result of longer timescale annealing methods.

For samples with very high active carrier concentrations, doping modifies the interaction between the laser light and the material. The Fermi level is pushed into the conduction band and, for samples with low electron effective masses, the absorption characteristics of the material are modified. This change in absorption increases the energy of light at which the sample absorbs. This means that, for samples with very high metastable doping concentrations and a carefully chosen laser type, the material will be optically transparent with high carrier concentrations and will absorb in areas with low carrier concentrations. Practically, this could be used to selectively anneal areas of samples, as long as the thermal diffusion distances are less than the feature sizes of interest for samples with heterogeneous carrier concentrations.

8.2 Future Work

This work can be extended in two different directions: through improving our mechanistic understanding of the effects of laser annealing on III-V materials and through the development of complementary *in-situ* and *ex-situ* characterization techniques suitable for laser-annealed samples.

8.2.1 Understanding and Optimizing Laser Annealing for III-V Materials

Suggested Sample Improvements for Improved Electrical Activation

Part of the emphasis of this work centered on determining whether laser annealing could activate ion-implanted dopants. We found that the high temperatures accessible through laser annealing (LSA) are effective at activating dopants, but lower temperature anneals with longer annealing times are needed to repair implantation damage. Crystalline damage degrades device performance and was frequently encountered in our studies; hence, it is worth further investigation to minimize the appearance of damage. Future work should look into the effect of using samples that already exhibit improved crystalline quality before annealing, either by limiting damage during implantation through heated implants or by incorporating a lower temperature, long annealing step to repair implantation damage before undertaking LSA.

Bridging Research-Scale Results with Industrial Requirements for Large-Scale Adoption

For all the III-V materials which were laser-annealed during this study, we found that the temperature "window" for maximal dopant activation is located very close to the temperature limit at which the sample becomes damaged. From a practical standpoint, this makes laser annealing difficult to recommend for widespread industrial adoption. For this thesis, the samples were annealed until the point at which they damaged to explore the entire temperature space up until damage. A high activation is not useful if it cannot be obtained without the samples cracking or melting. It would be useful to determine if reasonably high dopant activation is possible with laser annealing while simultaneously avoiding damaging the samples. Along this same idea, it would be useful to explore area annealing the samples with overlapping laser scans (unlike the single scan approach adopted here), as well as exploring spatially selective annealing through masking with a reflective film or pattering of absorber layer on top or buried within a sample. The stability of the metastable carrier concentrations would also be useful to study. By introducing a longer timescale furnace anneal after LSA, we can determine the stability of these metastable carrier concentrations with further thermal processing, which is important to determine for industrial adoption.

An important option to pursue would be to monolithically integrate InGaAs films onto silicon substrates. Ultimately, this most likely will be required for high-performance transistor applications. The source of damage for the laser-annealed InGaAs samples seems to stem primarily from damage to the InP substrate, which is extremely brittle and melts at the temperatures explored during

this laser annealing study. Using mechanically superior silicon substrates may allow the samples to reach slightly higher annealing temperatures, although the melting temperature of InGaAs will limit how high those temperatures can be and the thermal expansion mismatch between the materials may lead to other complicating issues.

Additionally, exploration into the possibility of activating ultra-shallow implants in InGaAs through LSA would also be very interesting, considering that this may be the direction that industry could take in order to form highly conductive source/drain contacts.

Understanding and Improving Laser Annealing Processes

In this thesis, annealing of GaN samples has only be been explored using a single dwell with the CO_2 laser because of the large variety of sample types used. Because heating during laser annealing critically rely on interaction between the light and the samples, any changes in the heterostructure, composition, and doping can drastically affect annealing behavior. This makes it extremely challenging to compare between samples and gain any real understanding of how laser annealing modifies a sample without knowing how the annealing behavior differs. By only using a single dwell, we can control for annealing time but, without more detailed temperature calibrations for each sample type, we cannot compare annealing temperature between samples. Additionally, when characterizing samples, there are no control samples to which we can compare, so any differences that result could be a result of differences in annealing behavior or differences in the sample heterostructure, doping, and composition. It would be interesting to explore a larger range of dwell times in order to determine how

different annealing times affect the kinetics and material damage incurred by GaN samples.

8.2.2 Recommended Characterization Techniques

This work can be extended to include complementary characterization techniques with good spatial resolution that are optimized for analyzing laser-annealed samples.

Temperature Characterization

For the samples that were used in this study, additional work is needed to understand the laser annealing heating profiles. The spatial temperature and peak temperature profiles for GaN should be characterized using the thin film resistor method used for the InGaAs system, as well as with absolute temperature calibrations that are ideal for determining much higher annealing temperatures, well beyond 1100 °C, and closer to the expected peak temperatures reached. This would allow us to have much more certainty in the temperature measurements. In addition, we need an understanding of the unexpected resistor results for diode laser-annealed InGaAs. Finally, the differences in laser absorption and heating profiles could be modeled with temperature- and dopant-dependent properties using CLASP (Cornell Laser Annealing Simulation Package) for a greater understanding of the 3D laser absorption and heat conduction through the entirety of the sample [134, 89, 135].

Another, extremely powerful option to characterize laser annealing temper-

atures *in-situ* would be to use thermoreflectance [136]. This method is currently being developed for our laser system as an optical, contact-free method to determine temperature profiles during laser annealing by shining an LED on the sample during annealing and recording the reflected signal with a CCD camera. Thermoreflectance would provide information that is complementary to the thin film resistor method but without requiring any clean room processing, only image analysis. Additionally, the thermoreflectance could be taken during each annealing laser scan and at high temperature, rather than having to extrapolate the low temperature behavior of the thin film resistor results to other samples.

Electrical, Optical, and Compositional Characterization

This work would be enhanced greatly by the implementation of collection of complementary characterization techniques. For example, micro-Hall measurements using patterned van der Pauw devices, or capacitance-voltage profiling could be used to compare to the carrier concentrations found with Raman spectroscopy. This would be extremely valuable as a comparison to the Hall measurements made by other groups for longer timescale annealing methods. Additionally, photoluminescence and IR spectroscopy could be used as a complementary, non-destructive optical technique to Raman in order to give a fuller picture of the characteristics of the sample. This includes information about band structure, free carriers, lattice properties, impurities and defects states, and microstructure (see Perkowitz for a combination of theory and examples for probing semiconductors using these optical techniques [122]). Of special interest is the calculations involved in local vibrational mode analysis, which probes

defect bonding information. Currently, we are collaborating with our computational team to model the local phonon Density of States (DOS) for silicon-doped InGaAs so that we can identify the local vibrational mode frequencies for silicon in different bonding sites using Raman spectroscopy. Using this technique coupled with lateral gradient laser spike annealing, we could identify the preferred bonding environment of silicon as a function of annealing temperature and time. Additionally, to probe changes for different depths into the sample, other wavelengths of light can also be used with Raman spectroscopy, which could be useful for resolving depth-dependent carrier concentrations or heterostructure composition. Spatially resolved SIMS measurements would also be extremely useful as a means to quantify and confirm the dopant concentration as a function of depth and to determine if concentration-dependent dopant diffusion takes place on the short timescales of LSA.

For the GaN samples, there is evidence of *n*-type carrier concentrations with annealing, but the source of this increase in carrier concentration is unclear. It would be very useful to determine if the carrier concentrations predicted from Raman are accurate and, if so, which defects are responsible for the increase in carrier concentration. These questions can be addressed using the techniques outlined above.

8.2.3 Summary of Future Work

In general, future extensions of the work in this thesis should focus on establishing a greater understanding of the complex defect behavior of the material. This work has shown macro-scale evidence for improved electrical properties, but an

atomic-level understanding is also crucial. This can be done through complementary optical characterization techniques such as photoluminescence and IR spectroscopy. Additionally, a large emphasis should be put on developing optical characterization techniques like thermoreflectance that could pair with laser annealing to rapidly and non-destructively probe the characteristics of interest for the LSA system and annealed samples. Continued collaboration with computational modeling can also help elucidate the role of thermodynamics and kinetics in III-V systems, through a greater understanding of the interplay of doping, defects, and temperature on behavior on an atomic scale.

APPENDIX A

STANDARD OPERATING PROCEDURES (SOPS)

A.1 Gold Dots

This SOP gives the fabrication instructions for gold dots that are used as an absolute temperature calibration for laser annealing.

A.1.1 SOP (Short Version)

- Oxford PECVD: Run "High Rate SiO_2" at 350°C to deposit 50 nm SiO_2
- Spin LOR 5A (dispense at 500 rpm, 100 rpm/s, 5s; spin at 3000 rpm, 500 rpm/s, 30 sec)
- Bake at 180°C for 5 min
- Spin nLOF 2020 (4000 rpm, 4000 rpm/s, 30 s)
- Bake at 110°C 1 min
- Expose nLOF series with dose of 66 mJ/cm^2 using Gold Dots Mask and Ruby lift to duplicate pattern
- Post-exposure bake at 110°C for 1 min
- Overdevelop in AZ 300MIF for 2 min
- Rinse with DI water and dry w/ nitrogen gun
- Evaporator: Deposit 1.5 nm Cr and 25 nm Au
- Lift-off in 1165
- DI water rinse and dry using N_2

A.1.2 SOP (Long Version)

Oxide Layer

Gold is a fast diffuser in InGaAs. The oxide layer should help with fabrication and will allow gold melt to be observed without having to worry diffusion/eutectic/alloying. Additionally, the surface energy of the oxide makes it so we can directly compare our results with the temperature calibrations on silicon samples.

- Deposit 50 nm of SiO_2 using the Oxford Plasma Enhanced Physical Vapor Deposition (PECVD)
- Run "High Rate SiO_2", at 350 °C
  - Deposits 250 nm/min, but check that calibration did not change in tool handbook
  - For 50 nm, deposit for 12 seconds
- Run "High Rate Clean", at 350 °C for 10 min + deposition time

Note: You can check film thickness using Rudolph FTM (in Class I resist room). Assume refractive index of film is less than the wafer ($r_f < r_w$) and use refractive index for thermal oxide.

A.1.3 Patterning

Gold Dots use a lift-off process and negative tone resist. The gold dot mask and Ruby Lift are in bins just ahead and to the left of the entrance in either Byungki or Willeman box.

Lift-off Resist

- Spin LOR 5A (in Class II resist room)
  - Deposit 1-2 drops at 500 RPM (rate), 100 RPM/s (ramping speed), for 5 seconds
  - Spin at 3000 RPM, 500 RPM/s, 30 sec
  - Tap edges with swab or on wipe to remove edge bead
  - Bake for 5 minutes at 180 °C on the LOR hot plate
  - The LOR should be ≈ 550 nm thick

Photoresist

- Spin AZ nLOF 2020 (in Class I resist room)
  - Deposit at 4000 RPM, 4000 RPM/s, 30 seconds (1-2 drops)
  - Tap edges with swab or on wipe to remove edge bead
  - Bake for 1 minute at 110 °C
  - The nLOF should be ≈ 2 µm thick

Expose

- Expose using ABM or Suss MA6 contact aligner
  - Use Gold Dot mask (CV alignment Au mask from 4/17/2014- Cr side towards sample, label towards back of tool)
  - On ABM
    - Use 365 lens with no filter

* $Exposure\ Time\ (s) = \frac{Dose\ (\mathrm{mJ/cm^2})}{Intensity\ (\mathrm{mW/cm^2})}$
* Dose for n-LOF 2020 is 66 $\mathrm{mJ/cm^2}$
* Intensity will vary over time and between tools, it will be listed on the tool ($\mathrm{mW/cm^2}$)
* Example: Assuming the intensity on ABM for the 365 nm lens with no filter is 11.8 $\mathrm{mJ/cm^2}$, $Exposure\ Time\ (s) = \frac{66\ \mathrm{mJ/cm^2}}{11.8\ \mathrm{mW/cm^2}} =$ 5.6 s
* Use screws to block vacuum for small pieces (on MA6, use the small piece chuck)
* Be careful not to break the piece during the exposure! Be gentle when raising the stage, and makes sure to hold down the depress chuck level button.
* Use Ruby Lift between the mask and the lamp to block light and selectively expose regions of sample. Use this to duplicate gold dots on top and bottom of InGaAs, See Figure A.1 for ideal layout.

– Post exposure bake for 1 minute at 110 °C

Develop

- Develop in AZ 300MIF
  – Find AZ 300MIF in base cabinet
  – Place sample face up in developer and swirl for 2 minutes
  – Rinse with DI water gun while removing, and place in DI water
  – Dry front and back with N_2 gun

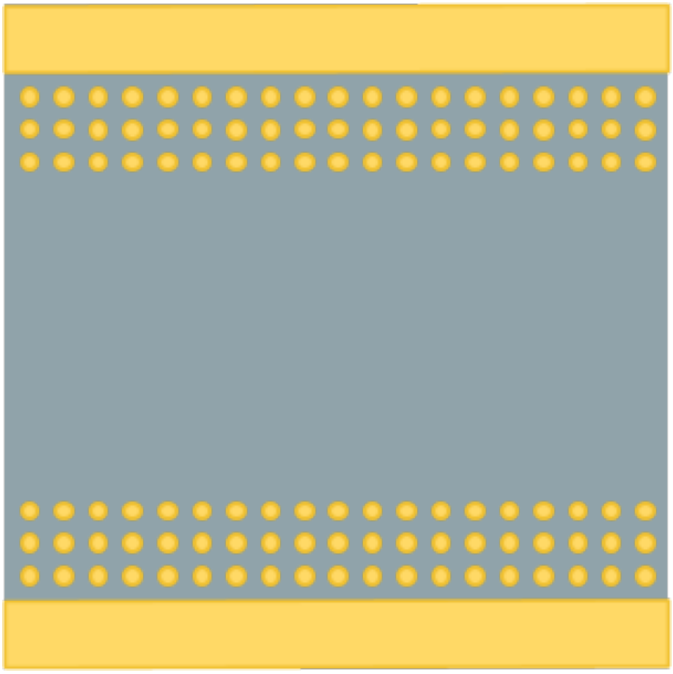

Figure A.1: Pattern of the gold dots on the sample. Use Ruby Lift to selectively pattern one half of the sample at a time. Not to scale.

Note: This recipe may need more development time, look under yellow light microscope for well defined gold dots. Try developing for more time if photoresist remains on unexposed regions. It is also very important to have good contact during the exposure step since the features are small. If you need to start over, soak in 1165 for a few hours to remove the photoresist. If satisfied with patterning, you can take the sample into white light.

A.1.4 Metal Deposition

Metal depositions are done using SC4500 Odd Hour Evaporator or the CHA evaporator. Use thermal evaporation for the chrome (wire) and either thermal or e-beam evaporation for the gold.

- Attach small samples using yellow evaporator tape just on the edges of the sample
- Deposit 1.5 nm Cr adhesion layer at $\approx 0.02 - 0.03$ nm/s
  - Let Cr degas before depositing, pressure will go up and then back to normal
- Deposit 25 nm gold at $\approx 0.05 - 0.1$ nm/s

A.1.5 Lift-Off

- Lift-off in 1165
  - Find 1165 in solvent cabinet
  - Place samples in 1165 for a few hours/overnight
  - Remove sample from 1165 and place in DI water while spraying with water.
  - Dry with N_2 gun (front and back)

Note: If the metal does not seem to be coming off, put it in the sonicator for a while. If metal still does not come off, gently swab it while still in 1165 (only if absolutely necessary). If the metal lifts off, but makes contact with the sample/dries it can stick and will not come off. Make sure to spray the sample while you remove the sample from 1165.

A.2 Platinum Resistors

This SOP gives the fabrication instructions for platinum resistors that are used as a relative temperature calibration for laser annealing. It fabricates a thin film resistor on top of a samples for a relative surface temperature measurement using four-point resistance measurements during laser annealing.

A.2.1 SOP (Short Version)

- Oxford PECVD: Run "High Rate SiO_2" at 350°C to deposit 50 nm SiO_2
- Spin LOR 5A (dispense at 500 rpm, 100 rpm/s, 5s; spin at 3000 rpm, 500 rpm/s, 30 sec)
- Bake at 180°C for 5 min
- Spin S1805 (4000 rpm, 4000 rpm/s, 30 s)
- Bake at 90°C 1 min
- Overexpose S1805 series by 30% with dose of 1.3×18 mJ/cm^2 using Thermistor Layer 1 Mask
- Post-exposure bake at 90°C for 1 min
- Overdevelop in 726 MIF for 2 min
- Rinse with DI water and dry w/ nitrogen gun
- Odd hour evaporator: Deposit 2 nm Cr (wire, thermal) and 40 nm Pt (no crucible, e-gun)
- Lift-off in 1165
- DI water rinse and dry using N_2

- Spin LOR 5A (dispense at 500 rpm, 100 rpm/s, 5s; spin at 3000 rpm, 500 rpm/s, 30 sec)
- Bake at 180°C for 5 min
- Spin S1805 (4000 rpm, 4000 rpm/s, 30 s)
- Bake at 90°C 1 min
- Overexpose S1805 series by 30% with dose of 1.3×18 mJ/cm^2 using Thermistor Layer 2 Mask
- Post-exposure bake at 90°C for 1 min
- Overdevelop in 726 MIF for 2 min
- Rinse with DI water and dry w/ nitrogen gun
- Odd hour evaporator: Deposit 250 nm Ni (crucible,e-gun)
- Lift-off in 1165
- DI water rinse and dry using N_2

A.2.2 SOP (Long Version)

Oxide Layer

When high temperatures are reached on InGaAs the increased conductivity can cause resistors to short. Oxide layer insulates the devices, preventing shorting.

- Deposit 50 nm of SiO_2 using the Oxford Plasma Enhanced Physical Vapor Deposition (PECVD)
- Run "High Rate SiO_2", at 350 °C
  - Deposits 250 nm/min, but check that calibration did not change in tool handbook
  - For 50 nm, deposit for 12 seconds
- Run "High Rate Clean", at 350 °C for 10 min + deposition time

Note: You can check film thickness using Rudolph FTM (in Class I resist room). Assume refractive index of film is less than the wafer ($r_f < r_w$) and use refractive index for thermal oxide.

A.2.3 Platinum Layer Patterning

Thin film resistors use standard Lift-off process and positive tone resist. These steps create the thin platinum wire that the laser passes over during temperature calibrations.

Lift-off Resist

- Spin LOR 5A (in Class II resist room)
  - Deposit 1-2 drops at 500 RPM (rate), 100 RPM/s (ramping speed), for 5 seconds
  - Spin at 3000 RPM, 500 RPM/s, 30 sec
  - Tap edges with swab or on wipe to remove edge bead
  - Bake for 5 minutes at 180 °C on the LOR hot plate
  - The LOR should be ≈ 550 nm thick

Photoresist

- Spin S1805 (in Class I resist room)
  - Deposit at 4000 RPM, 4000 RPM/s, 30 seconds (1-2 drops)
  - Tap edges with swab or on wipe to remove edge bead
  - Bake for 1 minute at 90 °C
  - The S1805 should be ≈ 500 nm thick

Expose

- Overexpose by 30% using ABM or Suss MA6 contact aligner
  - Use ”Thermistor Layer 1” mask (Cr side towards sample, label towards back of tool)
  - On ABM
    - Use 365 lens with no filter

    - $Exposure\ Time\ (s) = 130\% \times \frac{Dose\ (\mathrm{mJ/cm^2})}{Intensity\ (\mathrm{mW/cm^2})}$
    - Dose for S1805 is 18 $\mathrm{mJ/cm^2}$
    - Intensity will vary over time and between tools, it will be listed on the tool ($\mathrm{mW/cm^2}$)
    - Example: Assuming the intensity on ABM for the 365 nm lens with no filter is 11.8 $\mathrm{mJ/cm^2}$, $Exposure\ Time\ (s) = 130\% \times \frac{18\ \mathrm{mJ/cm^2}}{11.8\ \mathrm{mW/cm^2}} = 2.0\ \mathrm{s}$
    - Use screws to block vacuum for small pieces (on MA6, use the small piece chuck)
    - Be careful not to break the piece during the exposure! Be gentle when raising the stage, and makes sure to hold down the depress chuck level button.
  - Post exposure bake for 1 minute at 90 °C

Develop

- Overdevelop in MIF 726
  - Find MIF 726 in base cabinet
  - Place sample face up in developer and swirl for 2 minutes
  - Rinse with DI water gun while removing, and place in DI water
  - Dry front and back with N_2 gun

Note: Look under yellow light microscope for well-defined patterned resistors. If you need to start over, soak in 1165 for a few hours to remove the photoresist. If satisfied with patterning, you can take the sample into white light.

A.2.4 Platinum Metal Deposition

Metal depositions are done using SC4500 Odd Hour Evaporator. Use thermal evaporation for the chrome (wire) and e-beam evaporation for the platinum.

- Attach small samples using yellow evaporator tape just on the edges of the sample
- Deposit 2 nm Cr adhesion layer at $\approx 0.02 - 0.03$ nm/s using thermal evaporation off the Cr wire
  - Let Cr degas before depositing, pressure will go from 2×10^{-6} torr to about 1×10^{-5} torr and then back to normal, this happens when you heat the Cr wire
- Deposit 40 nm Pt at $\approx 0.05 - 0.1$ nm/s using e-beam evaporation

A.2.5 Lift-Off

- Lift-off in 1165
  - Find 1165 in solvent cabinet
  - Place samples in 1165 for a few hours/overnight
  - Remove sample from 1165 and place in DI water while spraying with water.
  - Dry with N_2 gun (front and back)

Note: If the metal does not seem to be coming off, put it in the sonicator for a while. If metal still does not come off, gently swab it while still in 1165 (only if absolutely

necessary). If the metal lifts off, but makes contact with the sample/dries it can stick and will not come off. Make sure to spray the sample while you remove the sample from 1165.

A.2.6 Nickel Layer Patterning

This basically a repetition of the steps for patterning and deposition of the platinum layer with a different mask and metal film. This is to make the metal contact pads to wirebond the packaging to.

Lift-off Resist

- Spin LOR 5A (in Class II resist room)
  - Deposit 1-2 drops at 500 RPM (rate), 100 RPM/s (ramping speed), for 5 seconds
  - Spin at 3000 RPM, 500 RPM/s, 30 sec
  - Tap edges with swab or on wipe to remove edge bead
  - Bake for 5 minutes at 180 °C on the LOR hot plate
  - The LOR should be ≈ 550 nm thick

Photoresist

- Spin S1805 (in Class I resist room)
  - Deposit at 4000 RPM, 4000 RPM/s, 30 seconds (1-2 drops)
  - Tap edges with swab or on wipe to remove edge bead

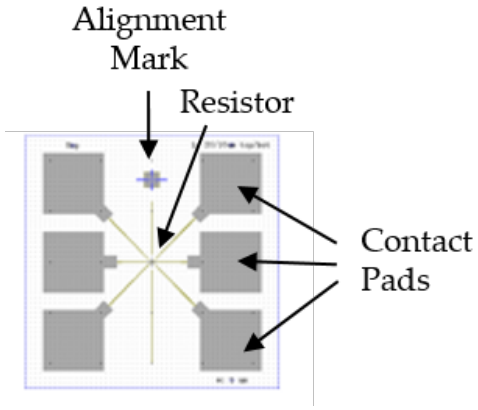

Figure A.2: Resistor mask layout mask showing the placement of the alignment mark. The large gray squares are the nickel contact pads and the thin yellow lines are the platinum wires.

- Bake for 1 minute at 90 °C
- The S1805 should be ≈ 500 nm thick

Expose

- Overexpose by 30% using ABM or Suss MA6 contact aligner
  - Use ”Thermistor Layer 2” mask (Cr side towards sample, label towards back of tool)
  - When exposing, place mask in frame so that the alignment marks (See Figure A.2) faces the top. Load the sample so the alignment mark is facing the same direction. Align this mark on the sample to the alignment mark on the frame.
  - Overexpose S1805 series by 30% with dose of 1.3×18 mJ/cm^2
  - Post exposure bake for 1 minute at 90 °C

Develop

- Overdevelop in MIF 726
  - Find MIF 726 in base cabinet
  - Place sample face up in developer and swirl for 2 minutes
  - Rinse with DI water gun while removing, and place in DI water
  - Dry front and back with N_2 gun

Note: Look under yellow light microscope for well defined patterned resistors. If you need to start over, soak in 1165 for a few hours to remove the photoresist. If satisfied with patterning, you can take the sample into white light. It is important that the Pt resistor wires are connected, without any breaks. If you do not have four contacts to the resistor, you will not be able to take measurements.

A.2.7 Nickel Metal Deposition

The metal deposition are done using SC4500 Odd Hour Evaporator. Use e-beam evaporation for the nickel.

- Attach small samples using yellow evaporator tape just on the edges of the sample
- Deposit 250 nm nickel (in a crucible) at $\approx$ 0.1 – 0.2 nm/s using e-beam evaporation with the recommended procedure for nickel in the evaporator manual
  - Ni can be difficult to evaporate because it can spit. If you cannot reach 250 nm, as long as you get to 200 nm, its okay.

- If possible, start the evaporation early. Evaporating 250 nm at 1 /s takes 40 minutes. If you dont want to rush (ramping up too slowly can cause spitting), start early and have your samples ready to load before you log on.

A.2.8 Lift-Off

- Lift-off in 1165
  - Find 1165 in solvent cabinet
  - Place samples in 1165 for a few hours/overnight
  - Remove sample from 1165 and place in DI water while spraying with water.
  - Dry with N_2 gun (front and back)

Note: If the metal does not seem to be coming off, put it in the sonicator for a while. If metal still does not come off, gently swab it while still in 1165 (only if absolutely necessary). If the metal lifts off, but makes contact with the sample/dries it can stick and will not come off. Make sure to spray the sample while you remove the sample from 1165. If you realize something went terribly wrong at this point, samples may be used again, by soaking in HF to remove the oxide layer (which should remove the metal layers as well) though you are probably better off getting new samples at this point.

A.2.9 Wire Bond Thin Film Resistors

Wire bond resistors using standard lead packages using West Bond 7400A Ultrasonic Wirebonder (Duffield 228).

- Epoxy the resistor to the packaging
  - Try to center the resistor, make sure the put the resistor in the correct direction. The shorter wire should be on top, and the lead packaging has a circle in the top left corner. See Figure A.3(a). Let dry overnight
- Connect each resistor contact pad to the packaging with two wire bonds, see Figure A.3(b)
  - Make some practice bonds. If the bonds are not sticking, you will need to alter the tool settings
  - a good starting point is
    - Tool Heat: 4
    - Channel 1 Time: 4, Power: 80 (3)
    - Channel 2 Time: 4, Power: 80 (3)
- After packaging, Use Ohm meter to test lead resistances. Place them between two opposing wires contacts. (Standard is around 1 kΩ)

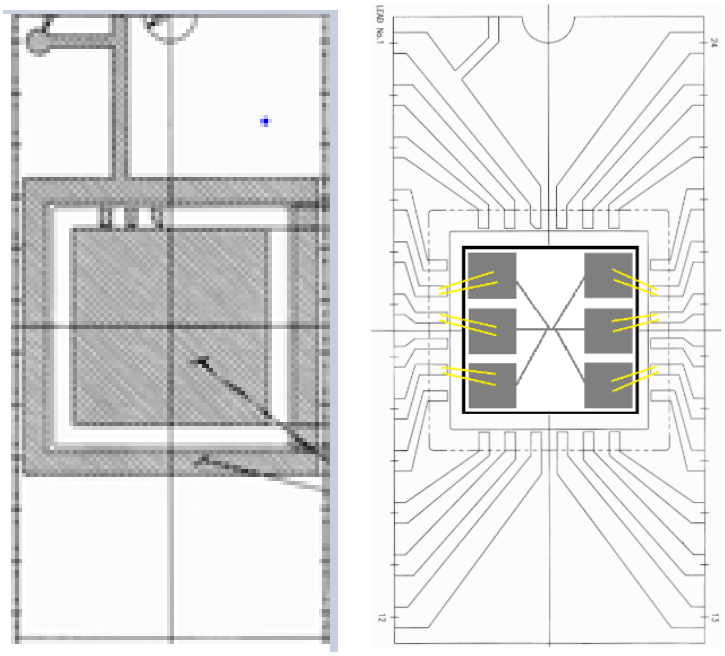

(a) (b)

Figure A.3: Top views of the resistor packaging (a) showing the correct orientation of the packaging and (b) with the resistor with the yellow lines marking the wirebonds to make with the wirebonder.

A.3 Frequently Asked Questions

What chuck do I use for 6X6 mm pieces?

Class I resist room: There is a small piece chuck on the top of the spinner hood. Class II resist room: Use the small screws in the chuck drawer, screw them in tightly into the spinner. You can also borrow the small chuck from the Class I Room, just make sure it is completely free of photoresist before you use it. Make sure to clean it well and return it after you are done. If you do this, it is best to do it when the clean room is not very busy so someone does not get frustrated looking for the small piece chuck.

What do I do to if the spinner does not recognize my piece?

This could be for multiple reasons. The back of your substrate or chuck may be dirty or there could be solvent in the vacuum line. First take off the sample, put it back on, and try to center again. If this does not work, clean the back of your sample and try again. If this does not work, clean your chuck, and try again. Finally, if it still will not work, try a new spinner (the solvent will evaporate after a while).

How do I remove an edge bead of resist? On small samples, there is an edge bead of resist that builds up after spinning. The easiest way to remove an edge bead of resist is to immediately get a clean room swab and lightly touch the edges of the sample in order to soak up extra resist. It is important to remove this bead because if you do not, it will solidify during the bake and create an uneven surface which could lead to sample cracking during exposure. A swab with 1165 also works if the photo resist has dried.

What do I do if the PR does not develop properly?
If you are pre/post baking, and using the right exposure time/developing time, and it is still not working, it is possible that the PR or developer has gone bad. Try again with a fuller bottle of developer or replace your PR.

What is the difference between a positive and negative photoresist?
Good question! It has to do with how the photoactive compound in the photoresist respond to light. A positive photoresist will dissolve where it has been exposed to light when it is developed. Whereas for negative photoresist, the unexposed regions will dissolve when developed. Always check your mask to make sure you are using the correct mask/photoresist combination.

What is LOR and what solvents can I use with it?

LOR stands for ”Lift Off Resist” and is used for metal liftoff processes. It is used in conjunction with a photoresist for patterning. Lift off processes for evaporated metals are nice because it avoids having to use a metal etch step. LOR is not photo sensitive so it is okay to take it into white light. To remove LOR edge beads after they have dried, use a swab with ”Remover PG” in hood of Class II resist room before baking. To strip off samples with LOR use ”1165” from the flammable cabinet of resist development room. Do not try to use acetone to remove LOR, it cross links.

Where can I learn more about the photoresist I am using?

In the Class I resist room there is a giant binder with all sorts of information on the photoresists used in CNF. It is a great place to look if you are troubleshooting the photolithography part of your recipe or making a new recipe. It has information like recommended spin speeds, exposure dose, and developer.

How do I replace/refill my resist?

Dispose of old/bad resist in Flammable Solvents waste bottle. Rinse bottle with acetone then isopropanol (these also go into the flammable solvent waste). Then fill again with resist from Flammable Cabinet in resist room. P20 can also be replaced. It is in a large bottle at the bottom of the other flammable cabinet where acetone is stored.

What if I finish off a bottle developer or solvent?

Do not put it back in the cabinet, instead take it to area with acid hoods. There is a bottle rinsing station in between the hoods. Open one of the containers and remove the previously rinsed bottle and cap. Place these in the cleaned container bin (with cap off). Place your empty bottle over the rinsing faucet and place the cap outwards. Close the lid and press the rinsing foot peddle at the

bottom.

How do I clean wafers/pieces?

If you want to clean Class I resist off your wafer (or just clean it in general), you can do this with acetone and isopropanol. Spin the wafers at 4000 RPM, 4000 RPM/s, and 60 seconds. Spray heavily with acetone for 10 seconds, then spray with acetone and IPA for 10 seconds, then spray with IPA for another 10 seconds. Make sure it spin dries all the way. Use the magnet (with a hook on it) to block the top left corner of the spinner so that you dont have to close the lid. If you have a lot of wafers that need resist removal, run them though the hot resist strip bath. (10 min in bath 1, 10 min in bath 2, and rinse in bath 3) Dry in spinners to the left.

How do I clean a mask?

If your mask gets dirty during exposure, you can clean it with acetone/IPA. Wipe the dirty part with acetone on a swab. Then spray the whole thing with acetone followed by IPA. Then dry with N_2 gun. There is also a mask cleaner in the Class I resist room.

Can I wait to expose or develop after spinning my pieces?

You can wait a few days after spinning/baking resist to expose them or after exposing to develop them. Just make sure you store them inside the yellow light area (there are some boxes label ”Byunki Jung” or ”Michael Willemann” near the exit that you can put the samples in). You can likely wait a few weeks after developing to move forward with your process, just keep them in the clean room.

Where can I learn more about the science and theory of micro and nano fabrication?

See: S.A. Campbell, *Fabrication Engineering at the Micro- and Nanoscale*, Fourth Ed. (Oxford University Press, New York, 2013) [52].

BIBLIOGRAPHY

[1] S. Adachi. *Properties of Semiconductor Alloys*. John Wiley & Sons, Ltd, Chichester, UK, 2009.

[2] I. Vurgaftman, J. R. Meyer, and L. R. Ram-Mohan. Band parameters for III-V compound semiconductors and their alloys. *J. Appl. Phys.*, 89(11):5815–5875, jun 2001.

[3] J. A. del Alamo. Nanometre-scale electronics with III-V compound semiconductors. *Nature*, 479(7373):317–323, nov 2011.

[4] J. Wang, B. Lukose, M. O. Thompson, and P. Clancy. Ab initio modeling of vacancies, antisites, and Si dopants in ordered InGaAs. *J. Appl. Phys.*, 121(4):045106, jan 2017.

[5] J. J. M. Law, A. D. Carter, S. Lee, C. Y. Huang, H. Lu, M. J. W. Rodwell, and A. C. Gossard. Co-doping of InxGa1-xAs with silicon and tellurium for improved ultra-low contact resistance. *J. Cryst. Growth*, 378:92–95, 2013.

[6] D. P. Byrnes, C. Ebert, Z. Pulwin, A. Krahnert, and F. Ramos. Optimization of tellurium doped InGaAs grown by MOCVD for solar cell tunnel junctions application. *2014 IEEE 40th Photovolt. Spec. Conf. PVSC 2014*, pages 1135–1138, 2014.

[7] M. B. Panish, R. A. Hamm, and L. C. Hopkins. Sn incorporation into InP grown by molecular beam epitaxy: A secondary-ion mass spectrometry study. *Appl. Phys. Lett.*, 56(23):2301–2303, 1990.

[8] L. Jiang, T. Lin, X. Wei, G. H. Wang, G. Z. Zhang, H. B. Zhang, and X. Y. Ma. Effects of V/III ratio on InGaAs and InP grown at low temperature by LP-MOCVD. *J. Cryst. Growth*, 260(1-2):23–27, 2004.

[9] C. J. Pinzone, N. D. Gerrard, R. D. Dupuis, N. T. Ha, and H. S. Luftman. Heavily-doped n-type InP and InGaAs grown by metalorganic chemical vapor deposition using tetraethyltin. *J. Appl. Phys.*, 67(11):6823–6829, 1990.

[10] T. Orzali, A. Vert, R. T. P. Lee, A. Norvilas, G. Huang, J. L. Herman, R. J. W. Hill, and S. S. P. Rao. Heavily tellurium doped n-type InGaAs grown by MOCVD on 300mm Si wafers. *J. Cryst. Growth*, 426:243–247, sep 2015.

[11] Y. Fedoryshyn, M. Beck, P. Kaspar, and H. Jaeckel. Characterization of Si volume- and delta-doped InGaAs grown by molecular beam epitaxy. *J. Appl. Phys.*, 107(9):093710, may 2010.

[12] A. G. Lind, H. L. Aldridge, C. Hatem, M. E. Law, and K. S. Jones. Review-Dopant Selection Considerations and Equilibrium Thermal Processing Limits for n+-In 0.53 Ga 0.47 As. *ECS J. Solid State Sci. Technol.*, 5(5):Q125–Q131, mar 2016.

[13] R. T. Bell, A. G. Jacobs, V. C. Sorg, B. Jung, M. O. Hill, B. E. Treml, and M. O. Thompson. Lateral Temperature-Gradient Method for High-Throughput Characterization of Material Processing by Millisecond Laser Annealing. *ACS Comb. Sci.*, 18(9):548–558, jul 2016.

[14] R. Cuscó, L. Artús, S. Hernández, J. Ibáñez, and M. Hopkinson. Raman scattering by LO phonon-plasmon coupled modes in n-type In0.53Ga0.47As. *Phys. Rev. B*, 65(3):035210, dec 2001.

[15] J. E. Maslar, J. F. Dorsten, P. W. Bohn, S. Agarwala, I. Adesida, C. Caneau, and R. Bhat. Phonon-electron interactions in the two-dimensional electron gas in InGaAs-InAlAs modulation-doped field-effect transistor structures studied by Raman scattering. *Appl. Phys. Lett.*, 63(14):1909–1911, oct 1993.

[16] S. Hernández, R. Cuscó, N. Blanco, G. González-Daz, and L. Artús. Study of the electrical activation of Si+-implanted InGaAs by means of Raman scattering. *J. Appl. Phys.*, 93(5):2659–2662, mar 2003.

[17] J. Ibáñez, E. Tarhan, A. K. Ramdas, S. Hernández, R. Cuscó, L. Artús, M. R. Melloch, and M. Hopkinson. Direct observation of LO phonon-plasmon coupled modes in the infrared transmission spectra of n-GaAs and n-In x Ga 1-x As epilayers. *Phys. Rev. B*, 69(7):075314, feb 2004.

[18] H. Harima. Properties of GaN and related compounds studied by means of Raman scattering. *J. Phys. Condens. Matter*, 14(38):R967–R993, sep 2002.

[19] H. Harima, H. Sakashita, and S. Nakashima. Raman Microprobe Measurement of Under-Damped LO-Phonon-Plasmon Coupled Mode in n-Type GaN. *Mater. Sci. Forum*, 264-268:1363–1366, 1998.

[20] P. Perlin, J. Camassel, W. Knap, T. Taliercio, J. C. Chervin, T. Suski, I. Grzegory, and S. Porowski. Investigation of longitudinal-optical phonon-plasmon coupled modes in highly conducting bulk GaN. *Appl. Phys. Lett.*, 67(17):2524–2526, oct 1995.

[21] T. Kozawa, T. Kachi, H. Kano, Y. Taga, M. Hashimoto, N. Koide, and K. Manabe. Raman scattering from LO phonon-plasmon coupled modes in gallium nitride. *J. Appl. Phys.*, 75(2):1098–1101, jan 1994.

[22] X. Ma. *Sub-millisecond Laser Spike Annealing of In0.53Ga0.47As*. PhD thesis, Cornell University, 2014.

[23] A. G. Lind. *Dopant-Defect Interactions in Si Doped InGaAs*. PhD thesis, University of Florida, 2015.

[24] A. G. Lind, H. L. Aldridge, K. S. Jones, and C. Hatem. Co-implantation of Al + , P + , and S + with Si + implants into In 0.53 Ga 0.47 As. *J. Vac. Sci. Technol. B, Nanotechnol. Microelectron. Mater. Process. Meas. Phenom.*, 33(5):051217, sep 2015.

[25] E. Towe, editor. *Heterogeneous Optoelectronics Integration*. SPIE Press, Bellingham, 2000.

[26] A. G. Baca and C. I. H. Ashby. *Fabrication of GaAs Devices*. Institution of Electrical Engineers, London, 2005.

[27] R. Chau, S. Datta, and A. Majumdar. Opportunities and Challenges of III-V Nanoelectronics for Future High-Speed, Low-Power Logic Applications. In *Compd. Semicond. Integr. Circuit Symp. 2005.*, pages 17–20. IEEE, 2005.

[28] R. Chau, S. Datta, and M. Doczy. Benchmarking Nanotechnology for High-Performance and Low-Power Logic Transistor Applications. *IEEE Trans. Nanotechnol.*, 4(2):153–158, 2005.

[29] R. Chau, B. Doyle, S. Datta, J. Kavalieros, and K. Zhang. Integrated nanoelectronics for the future. *Nat. Mater.*, 6(11):810–812, 2007.

[30] H. Riel, L.-E. Wernersson, M. Hong, and J. A. del Alamo. III-V compound semiconductor transistors-from planar to nanowire structures. *MRS Bull.*, 39(08):668–677, aug 2014.

[31] C. W. Liu, M. Östling, and J. B. Hannon. New materials for post-Si computing. *MRS Bull.*, 39(08):658–662, aug 2014.

[32] Editorial. There's more to come from Moore. *Nature*, 520(7548):408–408, apr 2015.

[33] S. Oktyabrsky and P. D. Ye, editors. *Fundamentals of III-V Semiconductor MOSFETs*. Springer US, Boston, MA, 2010.

[34] K. J. Kuhn, U. Avci, A. Cappellani, M. D. Giles, M. Haverty, S. Kim, R. Kotlyar, S. Manipatruni, D. Nikonov, C. Pawashe, M. Radosavljevic, R. Rios, S. Shankar, R. Vedula, R. Chau, and I. Young. The ultimate CMOS device and beyond. In *2012 Int. Electron Devices Meet.*, pages 8.1.1–8.1.4. IEEE, dec 2012.

[35] M. M. Waldrop. The chips are down for Moore's law. *Nature*, 530(7589):144–147, feb 2016.

[36] S. Nakamura, T. Mukai, and M. Senoh. Candela-class high-brightness InGaN/AlGaN double-heterostructure blue-light-emitting diodes. *Appl. Phys. Lett.*, 64(13):1687–1689, mar 1994.

[37] S. Nakamura. Nobel Lecture: Background story of the invention of efficient blue InGaN light emitting diodes. *Rev. Mod. Phys.*, 87(4):1139–1151, oct 2015.

[38] B. Bothwell, D. Drummond, M. Pilla, H. G. Xing, and D. Jena. Vertical GaN: The Pathway To Power Switching Efficiency. *Compd. Semicond.*, October:1–8, 2015.

[39] M. Ohring. *Materials Science of Thin Films*. Academic Press, second edition, 2001.

[40] P. Bhattacharya. *Properties of Lattice-Matched and Strained Indium Gallium Arsenide*. INSPEC, The Institution of Electrical Engineers, 1993.

[41] E. A. Fitzgerald, M. T. Bulsara, Y. Bai, C. Cheng, W. K. Liu, D. Lubyshev, J. Fastenau, Y. Wu, M. Urtega, W. Ha, J. Bergman, B. Briar, C. Drazek, N. Daval, F. Letertre, W. E. Hoke, J. R. LaRoche, K. J. Herrick, and T. E. Kazior. Monolithic III-V/Si Integration. *ECS Trans.*, 19(5):345–350, 2009.

[42] S. Datta, G. Dewey, J. M. Fastenau, M. K. Hudait, D. Loubychev, W. K. Liu, M. Radosavljevic, W. Rachmady, and R. Chau. Ultrahigh-Speed 0.5 V Supply Voltage In0.7Ga0.3As Quantum-Well Transistors on Silicon Substrate. *IEEE Electron Device Lett.*, 28(8):685–687, 2007.

[43] H. Schmid, M. Borg, K. Moselund, L. Gignac, C. M. Breslin, J. Bruley, D. Cutaia, and H. Riel. Template-assisted selective epitaxy of III-V

nanoscale devices for co-planar heterogeneous integration with Si. *Appl. Phys. Lett.*, 106(23):233101, jun 2015.

[44] A. Alkauskas, M. D. McCluskey, and C. G. Van de Walle. Tutorial: Defects in semiconductors-Combining experiment and theory. *J. Appl. Phys.*, 119(18):181101, 2016.

[45] K. S. Jones, A. G. Lind, C. Hatem, S. Moffatt, and M. C. Ridgeway. (Invited) A Brief Review of Doping Issues in III-V Semiconductors. *ECS Trans.*, 53(3):97–105, may 2013.

[46] T. F. Kuech, S. E. Babcock, and L. Mawst. Growth far from equilibrium: Examples from III-V semiconductors. *Appl. Phys. Rev.*, 3(4):040801, dec 2016.

[47] S. Limpijumnong and C. G. Van de Walle. Diffusivity of native defects in GaN. *Phys. Rev. B*, 69(3):035207, jan 2004.

[48] C. G. Van de Walle and J. Neugebauer. First-principles calculations for defects and impurities: Applications to III-nitrides. *J. Appl. Phys.*, 95(8):3851–3879, apr 2004.

[49] M. D. McCluskey and E. E. Haller. *Dopants and defects in semiconductors*. Taylor & Francis, Boca Raton, FL, 2012.

[50] N. Mukherjee, J. Boardman, B. Chu-Kung, G. Dewey, A. Eisenbach, J. Fastenau, J. Kavalieros, W. K. Liu, D. Lubyshev, M. Metz, K. Millard, M. Radosavljevic, T. Stewart, H. W. Then, P. Tolchinsky, and R. Chau. MOVPE III-V material growth on silicon substrates and its comparison to MBE for future high performance and low power logic applications. *Tech. Dig. - Int. Electron Devices Meet. IEDM*, pages 35.1.1–35.1.4, dec 2011.

[51] H. Ryssel and I. Ruge. *Ion Implantation*. Wiley, Chichester, 1986.

[52] S. A. Campbell. *Fabrication engineering at the micro- and nanoscale*. Oxford University Press, New York, fourth edition, 2013.

[53] K. G. Stephens. Doping of III-V compound semiconductors by ion implantation. *Nucl. Instruments Methods Phys. Res.*, 209-210:589–614, 1983.

[54] C. W. Farley and B. G. Streetman. The role of defects in the diffusion

and activation of impurities in ion implanted semiconductors. *J. Electron. Mater.*, 13(2):401–436, mar 1984.

[55] S. B. Ogale. Ion implantation and laser treatment of III-V compound semiconductor: A brief report. *Bull. Mater. Sci.*, 13(1-2):51–56, mar 1990.

[56] W. Wesch. Ion implantation in III-V compounds. *Nucl. Instruments Methods Phys. Res. Sect. B Beam Interact. with Mater. Atoms*, 68(1-4):342–354, may 1992.

[57] M. V. Rao. Ion implantation in III-V compound semiconductors. *Nucl. Instruments Methods Phys. Res. Sect. B Beam Interact. with Mater. Atoms*, 79(1-4):645–647, jun 1993.

[58] B. N. Feigelson, T. J. Anderson, M. Abraham, J. A. Freitas, J. K. Hite, C. R. Eddy, and F.J. Kub. Multicycle rapid thermal annealing technique and its application for the electrical activation of Mg implanted in GaN. *J. Cryst. Growth*, 350(1):21–26, jul 2012.

[59] C. T. Foxon, B. A. Joyce, R. F. C. Farrow, and R. M. Griffiths. The identification of species evolved in the evaporation of III-V compounds. *J. Phys. D. Appl. Phys.*, 7(17):317, nov 1974.

[60] K. G. Stephens. Doping of III-V compound semiconductors by ion implantation. *Nucl. Instruments Methods Phys. Res.*, 209-210:589–614, may 1983.

[61] D. E. Davies. Transient thermal annealing in GaAs. *Nucl. Instruments Methods Phys. Res. Sect. B Beam Interact. with Mater. Atoms*, 7-8:387–394, mar 1985.

[62] R. C. Clarke and G. W. Eldridge. Transient Capless Annealing of Ion-Implanted GaAs. *IEEE Trans. Electron Devices*, 31(8):1077–1082, 1984.

[63] C. A. Armiento and F. C. Prince. Capless rapid thermal annealing of GaAs using an enhanced overpressure proximity technique. *Appl. Phys. Lett.*, 48(23):1623, 1986.

[64] A. Alian, G. Brammertz, N. Waldron, C. Merckling, G. Hellings, H. C. Lin, W. E. Wang, M. Meuris, E. Simoen, K. De Meyer, and M. Heyns. Silicon and selenium implantation and activation in In0.53Ga0.47As under low thermal budget conditions. *Microelectron. Eng.*, 88(2):155–158, feb 2011.

[65] J. H. Yum, H. S. Shin, R. Hill, J. Oh, H. D. Lee, R. M. Mushinski, T. W. Hudnall, C. W. Bielawski, S. K. Banerjee, W. Y. Loh, W.-E. Wang, and P. Kirsch. A study of capping layers for sulfur monolayer doping on III-V junctions. *Appl. Phys. Lett.*, 101(25):253514, dec 2012.

[66] S. S. Kular, B. J. Sealy, M. H. Badawi, K. G. Stephens, D. Sadana, and G. R. Booker. Laser annealing of capped and uncapped GaAs. *Electron. Lett.*, 15(14):413, 1979.

[67] M. H. Badawi, J. A. Akintunde, B. J. Sealy, and K. G. Stephens. Effect of Si3N4 encapsulation on the laser-annealing behaviour of GaAs. *Electron. Lett.*, 15(15):447, 1979.

[68] T. E. Haynes, W. K. Chu, and S. T. Picraux. Direct measurement of evaporation during rapid thermal processing of capped GaAs. *Appl. Phys. Lett.*, 50(16):1071–1073, apr 1987.

[69] M. Kuzuhara and H. Kohzu. SiOxNy capped annealing for Si-implanted GaAs. *Appl. Phys. Lett.*, 44(5):527–529, 1984.

[70] W. Skorupa and H. Schmidt, editors. *Subsecond Annealing of Advanced Materials*, volume 192 of *Springer Series in Materials Science*. Springer International Publishing, Cham, first edition, 2014.

[71] R. Ditchfield. Rapid Thermal Processing: Fixing Problems with the Concept of Thermal Budget. *J. Electrochem. Soc.*, 144(5):1842, 1997.

[72] M. von Allmen and A. Blatter. *Laser-Beam Interactions with Materials*. Springer Series in Materials Science. Springer Berlin Heidelberg, Berlin, Heidelberg, second edition, 1995.

[73] S. O. Kucheyev, J. S. Williams, and S. J. Pearton. Ion implantation into GaN. *Mater. Sci. Eng. R Reports*, 33(2-3):51–108, may 2001.

[74] J. A. Golovchenko and T. N. C. Venkatesan. Annealing of Te-implanted GaAs by ruby laser irradiation. *Appl. Phys. Lett.*, 32(3):147–149, 1978.

[75] B. J. Sealy, S. S. Kular, K. G. Stephens, R. Croft, and A. Palmer. Electrical properties of laser-annealed donor-implanted GaAs. *Electron. Lett.*, 14(22):720, 1978.

[76] J. A. Akintunde. Laser-induced diffusion of silicon atoms from Si3N4 films deposited onto GaAs. *Thin Solid Films*, 113(1):73–78, mar 1984.

[77] A. Rys, A. D. Compaan, A. Bhat, H. W. Yao, and Y. Shieh. Pulsed laser annealing of GaAs implanted with Se and Si. *Opt. Eng.*, 29(4):329, 1990.

[78] P. A. Barnes, H. J. Leamy, J. M. Poate, S. D. Ferris, J. S. Williams, and G. K. Celler. Ohmic contacts produced by laser-annealing Te-implanted GaAs. *Appl. Phys. Lett.*, 33(11):965–967, dec 1978.

[79] R. B. James, W. H. Christie, R. E. Eby, B. E. Mills, and L. S. Darken. Nonlinear optical studies and CO2 laser-induced melting of Zn-doped GaAs. *J. Appl. Phys.*, 59(4):1323, 1986.

[80] E. Y.-J. Kong, P. Guo, X. Gong, B. Liu, and Y.-C. Yeo. Toward Conformal Damage-Free Doping With Abrupt Ultrashallow Junction: Formation of Si Monolayers and Laser Anneal as a Novel Doping Technique for InGaAs nMOSFETs. *IEEE Trans. Electron Devices*, 61(4):1039–1046, apr 2014.

[81] H. L. Aldridge, A. G. Lind, C. C. Bomberger, Y. Puzyrev, J. M. O. Zide, S. T. Pantelides, M. E. Law, and K. S. Jones. N-type doping strategies for InGaAs. *Mater. Sci. Semicond. Process.*, 57(January 2017):39–47, jan 2017.

[82] N. Watanabe, T. Nittono, and K. Watanabe. Annealing effect on the carrier concentration in heavily Si-doped n+ -InGaAs. *Appl. Phys. Lett.*, 61(16):1945–1947, oct 1992.

[83] A. G. Lind, H. L. Aldridge, C. C. Bomberger, C. Hatem, J. M. O. Zide, and K. S. Jones. Comparison of thermal annealing effects on electrical activation of MBE grown and ion implant Si-doped In 0.53 Ga 0.47 As. *J. Vac. Sci. Technol. B, Nanotechnol. Microelectron. Mater. Process. Meas. Phenom.*, 33(2):021206, mar 2015.

[84] E. Wendler, B. Breeger, Ch. Schubert, and W. Wesch. Comparative study of damage production in ion implanted III-V-compounds at temperatures from 20 to 420 K. *Nucl. Instruments Methods Phys. Res. Sect. B Beam Interact. with Mater. Atoms*, 147(1-4):155–165, jan 1999.

[85] G. Vitali, L. Palumbo, M. Rossi, G. Zollo, C. Pizzuto, L. Di Gaspare, and F. Evangelisti. Solid-phase epitaxy induced by low-power pulsed-laser annealing of III-V compound semiconductors. *Phys. Rev. B*, 53(8):4757–4769, feb 1996.

[86] D.-J. Kim, S.-E. Park, H.-J. Kim, J.-K. Ryu, B. O, and S.-S. Pak. Excimer Laser Annealing with a Line Beam for Improvement of Structural and Optical Properties of Polycrystalline GaN. *Japanese J. Appl. Physics, Part 1 Regul. Pap. Short Notes Rev. Pap.*, 42(12):7349–7353, 2003.

[87] H. T. Wang, L. S. Tan, and E. F. Chor. Pulsed laser annealing of Be-implanted GaN. *J. Appl. Phys.*, 98(9):094901, nov 2005.

[88] B. Jung. *Laser-induced millisecond heating of polymers and small molecules for pattern development*. PhD thesis, Cornell University, 2014.

[89] K. Iyengar, B. Jung, M. Willemann, P. Clancy, and M. O. Thompson. Experimental determination of thermal profiles during laser spike annealing with quantitative comparison to 3-dimensional simulations. *Appl. Phys. Lett.*, 100(21):211915, 2012.

[90] S. Adachi. *Optical Constants of Crystalline and Amorphous Semiconductors: Numerical Data and Graphical Information*. Springer Science+ Business Media, New York, 1999.

[91] B. Jung, J. Sha, F. Paredes, M. Chandhok, T. R. Younkin, U. Wiesner, C. K. Ober, and M. O. Thompson. Kinetic Rates of Thermal Transformations and Diffusion in Polymer Systems Measured during Sub-millisecond Laser-Induced Heating. *ACS Nano*, 6(7):5830–5836, jul 2012.

[92] P. M. Fauchet and A. E. Siegman. Surface ripples on silicon and gallium arsenide under picosecond laser illumination. *Appl. Phys. Lett.*, 40(9):824–826, 1982.

[93] A. Borowiec and H. K. Haugen. Subwavelength ripple formation on the surfaces of compound semiconductors irradiated with femtosecond laser pulses. *Appl. Phys. Lett.*, 82(25):4462–4464, 2003.

[94] J. Bonse, M. Munz, and H. Sturm. Structure formation on the surface of indium phosphide irradiated by femtosecond laser pulses. *J. Appl. Phys.*, 97(1):013538, jan 2005.

[95] D. W. Bäuerle. *Laser Processing and Chemistry*. Springer-Verlag Berlin Heidelberg, Berlin, Heidelberg, fourth edition, 2011.

[96] P. Blood and J. W. Orton. The electrical characterisation of semiconductors. *Reports Prog. Phys.*, 41(2):157–257, feb 1978.

[97] D. H. Petersen, R. Lin, T. M. Hansen, E. Rosseel, W. Vandervorst, C. Markvardsen, D. Kjær, and P. F. Nielsen. Comparative study of size dependent four-point probe sheet resistance measurement on laser annealed ultra-shallow junctions. *J. Vac. Sci. Technol. B Microelectron. Nanom. Struct.*, 26(1):362, 2008.

[98] C. V. Raman and K. S. Krishnan. A New Type of Secondary Radiation. *Nature*, 121(3048):501–502, 1928.

[99] L. A. Lyon, C. D. Keating, A. P. Fox, B. E. Baker, L. He, S. R. Nicewarner, S. P. Mulvaney, and M. J. Natan. Raman Spectroscopy. *Anal. Chem.*, 70(12):341–362, jun 1998.

[100] I. R. Lewis and H. Edwards. *Handbook of Raman Spectroscopy: From the Research Laboratory to the Process Line*. Practical Spectroscopy. CRC Press, 2001.

[101] A. Mooradian and G. B. Wright. First order Raman effect in III-V compounds. *Solid State Commun.*, 4(9):431–434, sep 1966.

[102] A. Mooradian and G. B. Wright. Observation of the Interaction of Plasmons with Longitudinal Optical Phonons in GaAs. *Phys. Rev. Lett.*, 16(22):999–1001, may 1966.

[103] A. Mooradian and A. L. McWhorter. Polarization and Intensity of Raman Scattering from Plasmons and Phonons in Gallium Arsenide. *Phys. Rev. Lett.*, 19(15):849–852, oct 1967.

[104] J. Ibáñez and R. Cuscó. Raman Spectroscopy of Compound Semiconductors. In A. Patane and N. Balkan, editors, *Semicond. Res.*, volume 150, chapter 9, pages 259–281. Springer Series, oct 2012.

[105] J. Jimenez and J. W. Tomm. *Spectroscopic Analysis of Optoelectronic Semiconductors*, volume 202. Springer International Publishing, 2016.

[106] W. Hayes and R. Loudon. *Scattering of Light by Crystals*. Dover Books on Physics. Dover Publications, Mineola, New York, 2004.

[107] J. P. Estrera, P. D. Stevens, R. Glosser, W. M. Duncan, Y. C. Kao, H. Y. Liu, and E. A. Beam. Phonon mode study of nearlatticematched In x Ga 1-x As using micro-Raman spectroscopy. *Appl. Phys. Lett.*, 61(16):1927–1929, oct 1992.

[108] J. Groenen, R. Carles, and G. Landa. Optical-phonon behavior in Ga 1-x In x As : The role of microscopic strains and ionic plasmon coupling. *Phys. Rev. B*, 58(16):452–462, 1998.

[109] H. W. Dinges, H. Burkhard, R. Lösch, H. Nickel, and W. Schlapp. Refractive indices of InAlAs and InGaAs/InP from 250 to 1900 nm determined by spectroscopic ellipsometry. *Appl. Surf. Sci.*, 54:477–481, 1992.

[110] T. Yuasa, S. Naritsuka, M. Mannoh, K. Shinozaki, K. Yamanaka, Y. Nomura, M. Mihara, and M. Ishii. Raman scattering from coupled plasmon LO-phonon modes in n-type Al x Ga 1-x As. *Phys. Rev. B*, 33(2):1222–1232, jan 1986.

[111] L. Artús, R. Cuscó, J. Ibáñez, N. Blanco, and G. Gonzalez-Diaz. Raman scattering by LO phonon-plasmon coupled modes in n-type InP. *Phys. Rev. B*, 60(8):5456–5463, 1999.

[112] R. Cuscó, E. Alarcón-Lladó, L. Artús, W. S. Hurst, and J. E. Maslar. Raman scattering by LO-phonon-plasmon coupled modes in Ga1-xInxAsySb1-y: Role of Landau damping. *Phys. Rev. B*, 81(19):195212, may 2010.

[113] L. P. Avakyants and T. P. Kolmakova. Raman spectroscopy determination of carrier concentration in n-In x Ga 1-x As epitaxial films. *Inorg. Mater.*, 47(4):335–339, 2011.

[114] S. Mishra, B. Singh, S. Bhattacharya, J. K. Panda, D. Kabiraj, A. Roy, and S. Ghosh. Probing charge carrier compensation in high energy ion irradiated III-V semiconductor by Raman spectroscopy and Hall measurements. *J. Raman Spectrosc.*, 47(8):963–970, aug 2016.

[115] V. C. Sorg, S. N. Zhang, M. Hill, P. Clancy, and M. O. Thompson. (Invited) Dopant Activation and Deactivation in InGaAs during Sub-Millisecond Thermal Annealing. *ECS Trans.*, 66(4):117–124, may 2015.

[116] K. R. Kort, P. Y. Hung, W.-Y. Loh, G. Bersuker, and S. Banerjee. Determination of Free Electron Density in Sequentially Doped InxGa1-xAs by Raman Spectroscopy. *Appl. Spectrosc.*, 69(2):239–242, feb 2015.

[117] A. G. Lind, T. P. Martin, V. C. Sorg, E. L. Kennon, V. Q. Truong, H. L. Aldridge, C. Hatem, M. O. Thompson, and K. S. Jones. Activation of Si implants into InAs characterized by Raman scattering. *J. Appl. Phys.*, 119(9):095705, mar 2016.

[118] J. E. Maslar, J. F. Dorsten, P. W. Bohn, S. Agarwala, I. Adesida, C. Caneau, and R. Bhat. Electron-phonon interactions in n-type In 0.53 Ga 0.47 As and In 0.52 Al 0.48 As studied by inelastic light scattering. *Phys. Rev. B*, 50(23):17143–17150, dec 1994.

[119] D. T. Hon and W. L. Faust. Dielectric Parameterization of Raman Lineshapes for GaP with a Plasma of Charge Carriers. *Appl. Phys.*, 1(5):241–256, may 1973.

[120] S. Hernández, R. Cuscó, J. Ibáñez, M. Hopkinson, and L. Artús. Anomalous dispersion with excitation wavelength of longitudinal optical phonon-plasmon coupled modes in n-InGaAs. *J. Phys. Condens. Matter*, 16(6):971–978, feb 2004.

[121] S. Adachi. *Physical properties of III-V semiconductor compounds: InP, InAs, GaAs, GaP, InGaAs, and InGaAsP*. Wiley, New York, 1992.

[122] S. Perkowitz. *Optical Characterization of Semiconductors: Infrared, Raman, and Photoluminescence Spectroscopy (Techniques of Physics)*. Elsevier, 2012.

[123] J. F. Ziegler, M. D. Ziegler, and J. P. Biersack. SRIM - The stopping and range of ions in matter (2010). *Nucl. Instruments Methods Phys. Res. Sect. B Beam Interact. with Mater. Atoms*, 268(11-12):1818–1823, jun 2010.

[124] Z. Guosheng, P. M. Fauchet, and A. E. Siegman. Growth of spontaneous periodic surface structures on solids during laser illumination. *Phys. Rev. B*, 26(10):5366, 1982.

[125] T. C. Penna, B. Tell, A. S. H. Liao, T. J. Bridges, and G. Burkhardt. Ion implantation of Si and Se donors in In 0.53 Ga 0.47 As. *J. Appl. Phys.*, 57(2):351–354, jan 1985.

[126] A. G. Lind, N. G. Rudawski, N. J. Vito, C. Hatem, M. C. Ridgway, R. Hengstebeck, B. R. Yates, and K. S. Jones. Maximizing electrical activation of ion-implanted Si in In 0.53 Ga 0.47 As. *Appl. Phys. Lett.*, 103(23):232102, dec 2013.

[127] M. J. Antonell, C. R. Abernathy, V. Krishnamoorthy, R. W. Gedridge, and T. E. Haynes. Thermal stability of heavily tellurium-doped InP grown by metalorganic molecular beam epitaxy. *J. Electron. Mater.*, 26(11):1283–1286, nov 1997.

[128] T. P. Pearsall, R. Carles, and J. C. Portal. Single longitudinal-mode optical phonon scattering in Ga 0.47 In 0.53 As. *Appl. Phys. Lett.*, 42(5):436–438, mar 1983.

[129] J. Groenen, G. Landa, R. Carles, P. S. Pizani, and M. Gendry. Tensile and compressive strain relief in In x Ga 1-x As epilayers grown on InP probed by Raman scattering. *J. Appl. Phys.*, 82(1997):803–809, 1997.

[130] S. Nojima and H. Asahi. Refractive index of InGaAs/InAlAs multi-quantumwell layers grown by molecular-beam epitaxy. *J. Appl. Phys.*, 63(2):479–483, jan 1988.

[131] G. W. Charache, D. M. DePoy, J. E. Raynolds, P. F. Baldasaro, K. E. Miyano, T. Holden, F. H. Pollak, P. R. Sharps, M. L. Timmons, C. B. Geller, W. Mannstadt, R. Asahi, A. J. Freeman, and W Wolf. MossBurstein and plasma reflection characteristics of heavily doped n -type InxGa1xAs and InPyAs1y. *J. Appl. Phys.*, 86(1):452–458, jul 1999.

[132] M. Muñoz, F. H. Pollak, M. Kahn, D. Ritter, L. Kronik, and G. M. Cohen. Burstein-Moss shift of n-doped In 0.53 Ga 0.47 As / InP. *Phys. Rev. B*, 63(23):233302, may 2001.

[133] W.-C. Lai, M. Yokoyama, S.-J. Chang, J.-D. Guo, C. Sheu, T. Chen, W.-C. Tsai, J.-S. Tsang, S.-H. Chan, and S. M. Sze. Optical and Electrical Characteristics of CO2-Laser-Treated Mg-Doped GaN Film. *Jpn. J. Appl. Phys.*, 39(Part 2, No. 11B):L1138–L1140, nov 2000.

[134] K. Iyengar, P. Clancy, and M. O. Thompson. Cornell Laser Annealing Simulation Package (CLASP), 2011.

[135] K. Iyengar. *Modeling Sub-Millisecond Laser Spike Annealing Processes*. PhD thesis, Cornell, 2012.

[136] J. Kölzer, E. Oesterschulze, and G. Deboy. Thermal imaging and measurement techniques for electronic materials and devices. *Microelectron. Eng.*, 31(1-4):251–270, feb 1996.